This is to certify that the
dissertation entitled

STRUCTURAL AND ELECTRONIC PROPERTIES OF RARE EARTH SILICIDES ON SI(001): NANOWIRES AND 3D ISLANDS

presented by

Chigusa Ohbuchi

has been accepted towards fulfillment
of the requirements for the

Ph.D. degree in Physics and Astronomy

Major Professor's Signature

8/18/04

Date

STRUCTURAL AND ELECTRONIC PROPERTIES OF RARE EARTH SILICIDES ON SI(001): NANOWIRES AND 3D ISLANDS

By

Chigusa Ohbuchi

A DISSERTATION

Submitted to
Michigan State University
in partial fulfillment of the requirements
for the degree of

DOCTOR OF PHILOSOPHY

Department of Physics and Astronomy

2004

ABSTRACT

STRUCTURAL AND ELECTRONIC PROPERTIES OF
RARE EARTH SILICIDES ON SI(001): NANOWIRES AND 3D ISLANDS

By

Chigusa Ohbuchi

Deposition of rare earth (RE) metals on the silicon(001) surface at elevated temperature results in the formation of RE silicide islands coexisting with a reconstructed substrate surface. This thesis presents the growth behavior of holmium, samarium, and dysprosium on Si(001) and the electronic properties of the resulting surface structures.

The growth of Ho and Sm on Si(001) at 600°C was studied using scanning tunneling microscopy (STM) and low energy electron diffraction.

Ho grows in a Stranski-Krastanov mode with highly elongated nanowires (NWs) and a 2×4 reconstructed substrate at low metal coverage. As the coverage increases, three-dimensional (3D) compact silicide islands coexist with the NWs. A 2×7 two-dimensional (2D) phase appears in the medium coverage range, and it always coexists with the 2×4 phase. Scanning tunneling spectroscopy (STS) data show that $HoSi_2$ NWs are more metallic than the 3D silicide islands or the reconstructed substrate.

Sm/Si(001) induces two different surface reconstructions: a lower coverage 2×3 phase and higher coverage 3×2/*c*(6×2) phases. In the high coverage regime, large 3D silicide islands are observed instead of elongated NWs.

The topographical evolution of 3D Dy silicide structures and the 2D reconstructed surface in the temperature range of 600 to 750°C was investigated by STM and low energy electron microscopy (LEEM). The initial surfaces were covered in the 2×7 superstructure plus NWs of uniform width defined by the 2×7 unit cell. Post-growth annealing at 700°C increases the number of 3D islands and the average island size. At the same time, the number of NWs decreases and surface reconstruction is swept away. Therefore, 3D silicide islands are a stable phase whereas NWs are a metastable phase at 700°C.

Ex-situ transport properties of the grown RE silicide films were correlated with film morphology as observed by STM. A 1 nm thick film of interconnected $DySi_2$ islands shows surface resistivity at 4.2 K similar to the reported bulk silicide value. A sample with sparse, disconnected islands shows higher surface resistivity than the 1 nm film but lower than that of the clean Si surface.

ACKNOWLEDGMENTS

First of all, I would like to thank my major advisor Professor Jun Nogami for having given me an opportunity to work in his group. I decided to do my research at Michigan State University because Dr. Nogami was there. He generously accepted me as his student even though I did not have enough background of surface physics. Without his offer, I could not even come to the U.S. and my Ph.D. life would never have started. I remember the days when he explained to me how STM works in JAPANESE because my English comprehension level was poor at that time. I was so grateful to him for his patience and generosity. I also thank him for giving me his time, support, and valuable advise, and feedback on my Ph.D. work.

I would like to thank my committee members, Professor Norman Birge, Professor Jack Baldwin, Professor Phillip Duxbury, Professor Thomas Glasmacher, and the previous committee, Professor Carl Bromberg who is currently on the Sabbatical, for their helpful comments and suggestions. Especially, I thank Dr. Birge for providing me technical assistance and knowledgeable advice on transport measurements.

There are several other people whom I would like to thank for helping me with transport measurements. Dr. Reza Loloee, a SQUID (superconducting quantum interference devices) specialist in Physics, made pre-deposited Ta and Ti contacts in the sputtering system. Michael Crosser and Ion Moraru, graduate students in Dr. Birge's lab, helped me with preparations for transport measurements in the clean room. They always gave me a hand whenever I needed them, even though they are busy with their own research.

I would like to express my appreciation to Dr. Wacek Swiech who is a LEEM specialist in the Frederick Seitz Materials Research Laboratory at the University of Illinois for his LEEM operation and image acquisition. I really enjoyed doing new experiments with him although his lab was extremely cold.

I thank former and current coworkers, Dr. Bangzhi Liu, Michael Katkov, Gangfeng Ye, and Jiaming Zhang for their kind support and friendship. Bangzhi and Micheal taught me how to do the STM experiments. Besides research, we used to have a cookout on summer weekend for fun and relaxing. I am really thankful to Gangfeng and Jiaming for encouraging me throughout the writing of this thesis.

I also thank Professor Evangelyn Alocilja in Biosystems and Agricultural Engineering for her continuous encouragement, prayer, and support for my successful research progress and future proposals.

Sean Davis and Beth Czischke are my best American friends and also my best English teachers. I learned a lot about American cultures and traditions from them. I am grateful to them for making my life more fulfilling and happier.

Finally, I would like to thank my fiancé Yuzuru Honda and my family in Japan for their loving and caring about me all the time. My parents sent me my favorite Japanese food for my energy source from time to time. Yuzuru has been waiting for the completion of my Ph.D. since I started the program, which becomes a powerful motivation for me to work hard and finish my Ph.D. within five years. I have been always feeling his overwhelming love and support although we are far apart. My gratitude to him is beyond words.

I thank all the other friends in Japan and the U.S. who cheered me up.

TABLE OF CONTENTS

LIST OF TABLES

LIST OF FIGURES

CHAPTER 4

CHAPTER 5

CHAPTER 6

CHAPTER 7

APPENDICES

ABBREVIATIONS

The following abbreviations are used in this thesis.

1D	one-dimensional
2D	two-dimensional
3D	three-dimensional
AFM	Atomic Force Microscopy
BF	bright field
DF	dark field
LEED	Low Energy Electron Diffraction
LEEM	Low Energy Electron Microscopy
ML	monolayer (see p.23 for the definition)
NW	nanowire
RE	rare earth
RT	room temperature
SEM	Scanning Electron Microscopy
STM	Scanning Tunneling Microscopy
STS	Scanning Tunneling Spectroscopy
TBF	tilted bright field
TEM	Transmission Electron Microscopy
UHV	ultra high vacuum

Chapter 1 Introduction

Our research objective is motivated by the potential for application of self-assembled rare earth (RE) silicide nanowires (NWs) for electronic and photonic devices in the semiconductor industry and to explore the structural and electrical properties of those NWs and their growth kinetic and dynamics.

In this chapter, the background and basic ideas of rare earth (RE) silicides and their growth behavior and electric properties are introduced. The organization of this thesis will be described in the end of this chapter.

1.1 Rare earth (RE) silicides and self-assembled RE disilicide NWs

RE disilicide NWs were firstly discovered by Preinesberger *et al.* in 1998 and they showed that Dy deposited on Si(001) forms NWs under certain conditions [1]. Unfortunately, this fascinating phenomenon was not noticed for more than 1 year. On November 1, 1999, the *New York Times* carried an article reporting that a Hewlett-Packard research group had produced conductive wires about 10 atoms wide [2]. These NWs were actually made of RE silicide [3]. This result was described as part of an impending revolution in molecular electronics and nanotechnology.

Since then, epitaxial RE silicides grown on silicon have attracted particular interest. In the study of RE silicides grown on Si(001), it has been reported that so far eight types of RE silicides can form self-assembled NWs: YSi_2 [4], $ScSi_2$ [5], $SmSi_2$ [6], $GdSi_2$ [5, 7, 8], $DySi_2$ [1, 5, 6, 9-12], $HoSi_2$ [9, 13, 14], $ErSi_2$ [3, 5, 6, 15, 16], and $YbSi_2$ [17]. For the other RE silicide/Si substrate systems, NW formation has been recently found on Dy/Si(111) [18], Gd/Si(111) [19], and Dy/Si(110) [20]. The formation of NWs is

ascribed to small lattice mismatch in one direction and large lattice mismatch in the perpendicular direction on Si(001) substrate. The mechanics of nanowire formation will be explained on page 15.

1.1.1 The rare earths

The rare earths are a group of 15 metallic elements: La (atomic number 57) through Lu (71) which appear in the extended sixth row of the periodic table as shown in Table 1.1. Along with Sc (21) and Y (39), they constitute the "RE elements". RE elements can be classified into two groups: the light RE elements (La to Eu) and the heavy RE elements (Gd to Lu, Sc and Y). The RE metals are typically trivalent, which are distinct by the progressive filling of the 4*f* localized subshell, while the external electrons are shared between 6*s* and 5*s* subshells which determine the conduction band maximum with a total charge of between two and three electrons under normal conditions [21]. The 5*d* and 6*s* subshells mix in the solid state, and RE metals have a conduction band of hybrid *s-d* character; the extent of hybridization varies along the series in a rather irregular way. In contrast to most of the trivalent RE metals, Sm, Eu, and Yb are divalent. The divalence of Eu and Yb metals is well explained in terms of very stable configuration of half filled ($4f^7$) and completely filled 4*f* band ($4f^{14}$), respectively [21]. Sm forms divalent or trivalent compounds depending on the chemical environment, because two valence states have rather similar energies [22, 23].

Table 1.1 Periodic table of the elements

^{1}H																	^{2}He
^{3}Li	^{4}Be											^{5}B	^{6}C	^{7}N	^{8}O	^{9}F	^{10}Ne
^{11}Na	^{12}Mg											^{13}Al	^{14}Si	^{15}P	^{16}S	^{17}Cl	^{18}Ar
^{19}K	^{20}Ca	^{21}**Sc**	^{22}Ti	^{23}V	^{24}Cr	^{25}Mn	^{26}Fe	^{27}Co	^{28}Ni	^{29}Cu	^{30}Zn	^{31}Ga	^{32}Ge	^{33}As	^{34}Se	^{35}Br	^{36}Kr
^{37}Rb	^{38}Sr	^{39}**Y**	^{40}Zr	^{41}Nb	^{42}Mo	^{43}Tc	^{44}Ru	^{45}Rh	^{46}Pd	^{47}Ag	^{48}Cd	^{49}In	^{50}Sn	^{51}Sb	^{52}Te	^{53}I	^{54}Xe
^{55}Cs	^{56}Ba	57~71	^{72}Hf	^{73}Ta	^{74}W	^{75}Re	^{76}Os	^{77}Ir	^{78}Pt	^{79}Au	^{80}Hg	^{81}Tl	^{82}Pb	^{83}Bi	^{84}Po	^{85}At	^{86}Rn
^{87}Fr	^{88}Ra	89~103	^{104}Rf	^{105}Db	^{106}Sg	^{107}Bh	^{108}Hs	^{109}Mt	^{110}Uun	^{111}Uuu	^{112}Uub	113	^{114}Uuq	115	^{116}Uuh	117	^{118}Uuo

Light RE elements							Heavy Rare Earth elements										
^{57}La	^{58}Ce	^{59}Pr	^{60}Nd	^{61}Pm	^{62}**Sm**	^{63}Eu	^{64}**Gd**	^{65}Tb	^{66}**Dy**	^{67}**Ho**	^{68}**Er**	^{69}Tm	^{70}**Yb**	^{71}Lu
^{89}Ac	^{90}Th	^{91}Pa	^{92}U	^{93}Np	^{94}Pu	^{95}Am	^{96}Cm	^{97}Bk	^{98}Cf	^{99}Es	^{100}Fm	^{101}Md	^{102}No	^{103}Lr

RE metals are gray-shaded. RE metals which can form NWs are highlighted with bold letters.

1.1.1.1 RE silicides

The investigation of the intrinsic character of RE silicide systems started to develop in the early 1980s; interface and thin film formation, electronic structure, and transport and magnetic properties [24-29]. Since then, studies of RE compound layers on semiconductors have become increasingly popular. Some of their advantages are the low growth temperatures, the good thermal stability, the low Schottky barrier on *n*-type Si substrates [24], and their compatibility to the Si technology. Moreover, these silicides are characterized by a small lattice mismatch relative to the Si(111) surface, ranging from zero to 2.5 %, thereby allowing epitaxial growth with chemically sharp interfaces and a high degree of crystallinity and structural perfection. Another interest is that of magnetic properties of RE compounds, associated with a large value of the magnetic moment of 4*f* layer of RE elements. These properties are unusual and can be studied by electrical transport methods, because the magnetic ions interact strongly with conduction electrons (see Chapter 7).

The RE silicides occur in three major stoichiometries: in metal rich form as RE_5Si_3 and RE_5Si_4 silicides, as monosilicides RESi, and as disilicides of varying composition, silicon rich $RESi_{2-x}$ with $0 \leq x \leq 0.33$ (from RE_3Si_5 to $RESi_2$) [30-34]. From the present viewpoint, the disilicides are of most interest, since this type of stoichiometry develops upon annealing of RE overlayers on Si.

1.1.2 Crystal structures of $RESi_{2-x}$

The crystallographic properties have been described earlier in several papers [30, 35, 36]. As shown in Figure 1.1, three main crystallographic structures are encountered, depending on the RE metal and on the silicon content: the hexagonal AlB_2 structure (*p6/mmm* space group) [Figure 1.1 (a)], the tetragonal $ThSi_2$ structure (*I4/amd* space group), and its distorted orthorhombic variant $GdSi_2$ (*Imma* space group) [Figure 1.1 (b)]. The structures and lattice constants are listed on Table 1.2. The first three RE metals (La, Ce, and Pr) crystallize in the tetragonal $ThSi_2$ or orthorhombic $GdSi_2$ structure. The next RE metals (Nd to Gd) can crystallize all the three structures depending on the RE elements. The hexagonal AlB_2 structure is found mainly in heavy RE compounds like $YbSi_{2-x}$ and $ScSi_{2-x}$ for a stoichiometry close to R_3Si_5 [37, 38], and corresponds to the structure of epitaxial films grown on Si(111). The type of structure adopted depends on the nature of the RE, on the value of x in $RESi_{2-x}$ and on the temperature.

AlB_2 structure hosts the metal atoms in hexagonal planes along the c-axis ([0001] direction) [Figure 1.1 (a)]. The hexagonal RE planes alternate with Si atoms in a honeycomb arrangement. In this lattice, Si atoms occupy the interstitial sites between the hexagonal layers of RE atoms. However, the growth of epitaxially ordered RE_3Si_5 layers is observed and this bulk-like silicide forms a defected hexagonal AlB_2 structure, consisting of stacked hexagonal RE planes and graphite-like Si planes with an ordered arrangement of vacancies at every sixth Si lattice site [39]. Therefore, the actual compositions of Si atoms vary between 1.67 and 2.00 per RE atom although the stoichiometry for perfect AlB_2-type RE silicides would be $RESi_2$.

Tetragonal $ThSi_2$ structure [Figure 1.1 (b)] is closely related to the AlB_2 structure.

Starting from the AlB_2 structure [Figure 1.1 (c)] and introducing shear planes parallel to $(10\bar{1}0)_{hex}$ with a shear vector $(\mathbf{b}_{hex} + \mathbf{c}_{hex})/2$ and a periodicity of $\sqrt{3}\,a_{hex}$, the $ThSi_2$ structure is derived [Figure 1.1 (d)]. As a consequence, the lattice parameters of the two structures are related:

$$a = b \approx (a_{hex} + c_{hex})/2 \text{ and } c \approx 2\sqrt{3}\,a_{hex}$$

The orthorhombic $GdSi_2$ structure is a deformation of the tetragonal $ThSi_2$ structure with $a \neq b$.

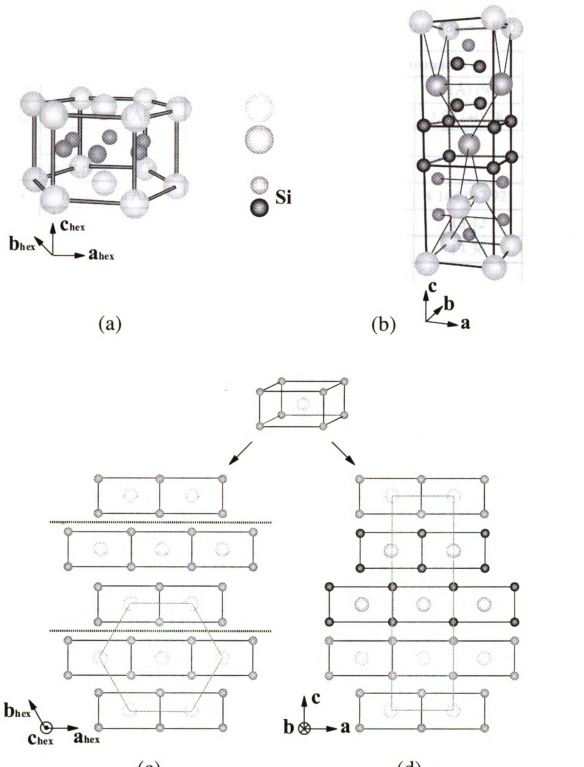

Figure 1.1 Spatial models for (a) the hexagonal AlB_2 structure, and (b) tetragonal $ThSi_2$ structure or orthorhombic $GdSi_2$ structure. (c) Projection of AlB_2 structure along the c_{hex}-axis. (d) Projection of $ThSi_2/GdSi_2$ along the *b*-axis; Introduction of shear planes in AlB_2 generates the $ThSi_2/GdSi_2$ structure.

Table 1.2 $RESi_2$ lattice parameters and mismatches with Si substrate. (a_{Si} = 3.840 Å)

Silicide	Structure	Lattice parameter and mismatch			Ref
		a (Å) (%)	b (Å) (%)	c (Å) (%)	
$ScSi_{1.7}$	hexagonal AlB_2	3.66 (-4.69)		3.87 (+0.78)	[40]
	tetragonal $ThSi_2$				
	orthorhombic $GdSi_2$				
YSi_2	hexagonal AlB_2	3.842 (+0.05)		4.144 (+7.92)	[36]
	tetragonal $ThSi_2$	4.04 (+5.21)		13.42	[40]
	orthorhombic $GdSi_2$	4.05 (+5.52)	3.954 (+2.97)	13.36	[40]
$LaSi_2$	hexagonal AlB_2				
	tetragonal $ThSi_2$	4.31 (+12.2)		13.80	[41]
	orthorhombic $GdSi_2$	4.271 (+11.2)	4.182 (+8.91)	14.035	[42]
$CeSi_2$	hexagonal AlB_2				
	tetragonal $ThSi_2$	4.192 (+9.17)		13.86	[42]
	orthorhombic $GdSi_2$	4.19 (+9.11)	4.13 (+7.55)	13.92	[42]
$PrSi_2$	hexagonal AlB_2				
	tetragonal $ThSi_2$	4.22 (+9.90)		13.71	[42]
	orthorhombic $GdSi_2$	4.20 (+9.38)	4.16 (+8.33)	13.76	[42]
$NdSi_2$	hexagonal AlB_2	4.12 (+7.29)		4.44 (+15.6)	[43]
	tetragonal $ThSi_2$	4.111 (+7.06)		13.56	[42]
	orthorhombic $GdSi_2$	4.155 (+8.20)	4.125 (+7.42)	13.67	[42]
$PmSi_2$	hexagonal AlB_2				
	tetragonal $ThSi_2$				
	orthorhombic $GdSi_2$				
Sm_3Si_5 $SmSi_2$	hexagonal AlB_2	3.90 (+1.64)		4.21 (+9.64)	[44]
	tetragonal $ThSi_2$	4.08 (+6.25)		13.51	[42]
	orthorhombic $GdSi_2$	4.105 (+6.90)	4.035 (+5.08)	13.46	[42]
$EuSi_2$	hexagonal AlB_2				
	tetragonal $ThSi_2$	4.29 (+11.7)		13.66	[42]
	orthorhombic $GdSi_2$				

Table 1.2 (cont'd)

Silicide	Structure	Lattice parameter and mismatch			Ref
		a (Å) (%)	b (Å) (%)	c (Å) (%)	
$GdSi_2$	hexagonal AlB_2	3.877 (+0.96)		4.172 (+8.65)	[36]
	tetragonal $ThSi_2$	4.10 (+6.77)		13.61	[42]
	orthorhombic $GdSi_2$	4.09 (+6.51)	13.44	13.44	[42]
$TbSi_2$	hexagonal AlB_2	3.847 (+0.18)		4.146 (+7.97)	[36]
	tetragonal $ThSi_2$				
	orthorhombic $GdSi_2$	4.057 (+5.65)	3.97 (+3.39)	13.375	[42]
$DySi_2$	hexagonal AlB_2	3.831 (-0.23)		4.121 (+7.32)	[36]
	tetragonal $ThSi_2$	4.03 (+4.95)		13.38	[42]
	orthorhombic $GdSi_2$	4.04 (+5.21)	3.95 (+2.86)	13.34	[42]
$HoSi_2$	hexagonal AlB_2	3.816 (-0.63)		4.107 (+6.95)	[36]
	tetragonal $ThSi_2$	3.964 (+3.23)		13.297	[45]
	orthorhombic $GdSi_2$	4.03 (+4.95)	3.944 (+2.71)	13.30	[42]
$ErSi_{2-x}$ $(0<x<0.5)$	hexagonal AlB_2	3.79 (-1.30)		4.09 (+6.51)	[46]
	tetragonal $ThSi_2$	3.96 (+3.13)		13.26 (+245)	[46]
	orthorhombic $GdSi_2$	5.6 (+45.8)	13.26 (+245)	5.6	[46]
		5.6 (+45.8)	13.26 (+245)	11.2	[46]
$TmSi_2$	hexagonal AlB_2	3.768 (-1.88)		4.070 (+5.99)	[36]
	tetragonal $ThSi_2$				
	orthorhombic $GdSi_2$				
$YbSi_2$	hexagonal AlB_2	3.784 (-1.46)		4.098 (+6.71)	[36]
	tetragonal $ThSi_2$				
	orthorhombic $GdSi_2$				
$LuSi_2$	hexagonal AlB_2	3.747 (-2.42)		4.046 (+5.36)	[36]
	tetragonal $ThSi_2$				
	orthorhombic $GdSi_2$				

1.1.2.1 Epitaxial growth of RE silicides on Si substrate

Since RE silicides are extremely reactive with oxygen, which hindered early attempts at fabrication, both growth technique and epitaxial conditions are very important for improving epitaxial quality in silicides. Continued *in-situ* work in UHV systems is necessary for the production of RE silicide films of adequate quality.

RE silicides can be grown on Si substrates by codeposition of RE and Si at elevated temperatures or by solid-phase epitaxy, i.e. by RE deposition on Si and subsequent annealing [25, 26, 36, 47-49]. In the latter case, the diffusion processes necessary for silicide formation give rise to a complex interplay of energetic and kinetic processes, requiring a detailed control of the process parameters.

A Si(111) substrate favors the epitaxial growth on it of the RE silicide phase with the AlB_2 structure, because it contains three equivalent directions (the three <110> directions) related with a three-fold symmetry [Figure 1.2 (a)]. In the case of a Si(001) substrate, there are only two <110> directions related with a two-fold symmetry [Figure 1.3 (a)]and thus a tetragonal phase is favored for the formation of thin films.

1.1.2.1.1 Epitaxial growth of RE silicides on Si(111)

Small lattice mismatch to Si(111) substrates makes epitaxial layer growth possible and ensures an ideal interface structure with minimized defect states [36]. For the growth of trivalent RE metals (except for Sm, Eu, and Yb) on Si(111) at elevated temperatures, a $p(1\times1)$ interface is formed in the submonolayer range and consists of a bulk-like Si substrate with a single RE T_4 site (second-layer substrate atom) with a rotated Si bilayer on top on the RE [50, 51] as shown in Figure 1.2. The growth of divalent RE metals

(Sm, Eu, and Yb) on Si(111) behaves differently. Low energy electron diffraction (LEED) and scanning tunneling microscopy (STM) studies show 3×1, 3×2, 5×1, and 7×1 periodicities for Sm [52] and Yb [52-54], and 3×1, 3×3, and 5×5 for Eu [55].

As the coverage increases, $\sqrt{3}\times\sqrt{3}R30^\circ$ structure has been mainly observed for most of the RE metals [51, 56, 57] although two-dimensional (2D) Eu or Yb layer on Si(111) has 2×1 reconstruction [58, 59]. The $\sqrt{3}\times\sqrt{3}R30^\circ$ structure is assigned to an ordered superlattice of Si vacancies producing a $\sqrt{3}\times\sqrt{3}$ mesh in the silicide film [60]. This silicide film is identified to be hexagonal $RESi_{2-x}$ with AlB_2 structure where the Si atoms are arranged in a hexagonal plane normal to the silicide *c*-axis, which has a good matching of the lattice parameters (a_{Si} = 0.384 nm) of the Si(111) surface. This allows interface configurations with lattice mismatches of less than 2 %, resulting in high quality epitaxial growth. The orientation relationships of hexagonal $RESi_{2-x}$ on Si(111) [46, 61-63] are determined to be:

$RESi_{2-x}(0001)$ // Si(111) and $RESi_{2-x}[1\bar{1}00]$ // Si$[\bar{1}2\bar{1}]$

as shown in Figure 1.2.

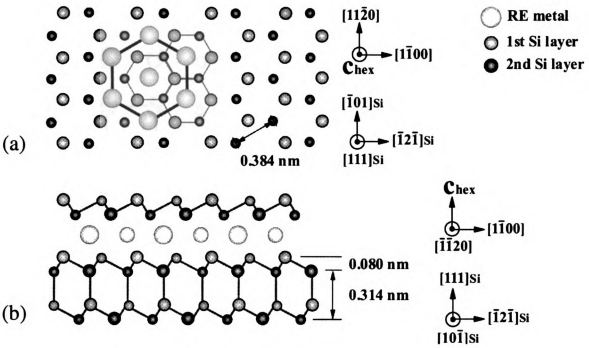

Figure 1.2 Structural model for Si(111)1×1-RE: (a) top view and (b) side view.

1.1.2.1.2 Epitaxial growth of RE silicides on Si(001)

Many studies of thin RE silicide film growth on Si(111) have been reported due to the easy epitaxial growth in this crystallographic orientation. However, until the discovery of self-assembled RE disilicide NWs [1, 3, 13], only a few studies were performed on Si(001) [61, 64-66] which exhibits a square unit cell as shown in Figure 1.3 (a). Most prior thin film growth studies looked at film thicknesses between 25 and 200 nm, where the most interesting features were the crystallographic phases present, and the epitaxial relationship with respect to the substrate.

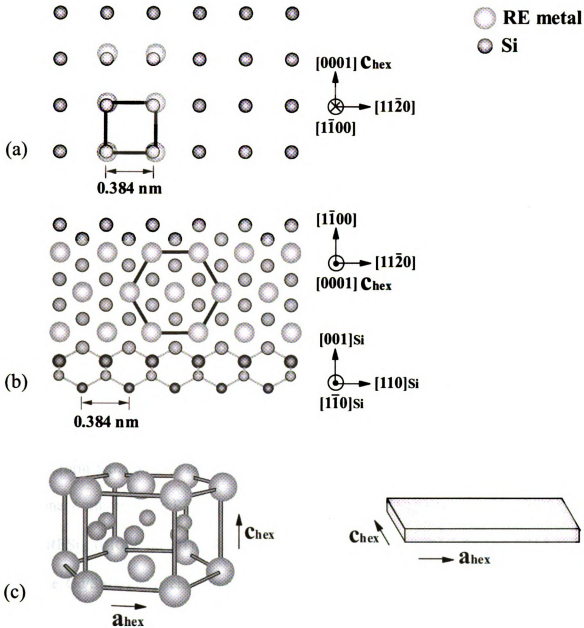

Figure 1.3 Structural model of Si(001)1×1-RE: (a) top view and (b) side view. The orientation relationship between hexagonal AlB_2 and NW structures are shown in (c).

As already mentioned before, a Si(001) substrate contains only two <110> directions and thus the growth mode is different from Si(111). In the case of $ErSi_2$ thin films, the lattice parameters of hexagonal AlB_2-type $ErSi_2$ (a_{hex} = 0.379 nm and c_{hex} = 0.409 nm) are relatively close to the lattice parameter of Si(001) (a_{si} = 0.384 nm) (see Table 1.2).

Epitaxy with the a_{hex}- and c_{hex}-axes parallel to the two mutually perpendicular <110>$_{Si}$ directions of the substrate has two obvious orientation variants, with the a_{hex}- and c_{hex}-axes interchanging directions in the two variants. Although there are several epitaxial modes as observed in hexagonal $ErSi_{2-x}$ [67], the orientation relationships of hexagonal $RESi_{2-x}$ (h-$RESi_{2-x}$) on Si(001) [46, 61-64] are generally determined to be:

h-$RESi_{2-x}(1\bar{1}00)$ // Si(001) and h-$RESi_{2-x}$ [0001] // Si[$1\bar{1}0$]

or h-$RESi_{2-x}(1\bar{1}00)$ // Si(001) and h-$RESi_{2-x}$ [$11\bar{2}0$] // Si[$1\bar{1}0$] (rotated by 90°)

The vacancy ordering superstructure of unit cell ($a\sqrt{3}$ $a\sqrt{3}$ $2c$) is also found in epitaxial hexagonal YSi_{2-x}, $TbSi_{2-x}$, $DySi_{2-x}$, and $ErSi_{2-x}$ thin films with AlB_2 structure on Si(001) [61].

The tetragonal $ThSi_2$ and orthorhombic $GdSi_2$ structures are grown in the similar way. Several $RESi_{2-x}$ thin films such as $DySi_{2-x}$ [68], $ErSi_{2-x}$ [46, 62], and $LuSi_{2-x}$ [69] on Si(001) form tetragonal or orthorhombic structures and the orientation relationships of tetragonal / orthorhombic $RESi_{2-x}$ (t-$RESi_{2-x}$) on Si(001) are determined to be:

t-$RESi_{2-x}$(010) // Si(001), t-$RESi_{2-x}$ [100] // Si[110], and t-$RESi_{2-x}$ [001] // Si[$1\bar{1}0$]

For the Gd/Si(001) system, the coexistence of epitaxial h-$GdSi_{2-x}$ and o-$GdSi_{2-x}$, and polycrystalline o-$GdSi_2$ is observed depending on the growth conditions [48, 63]. The formation of an epitaxial $HoSi_2$ layer by solid phase reaction is reported, but no structural detail is given [70].

When the amount of metal deposited onto the Si surface is insufficient to create a continuous thin film, then the RE silicide grows in what can be described as the Stranski-Krastanov mode. In reality, the RE grows as a 2D metal induced surface reconstruction involving at most 1 ML of metal, and 3D silicide nanostructures that can

be described as either NWs or islands [1, 3-9, 11-14, 17]. Various types of periodicities due to the surface reconstruction are observed at low metal coverages: 2×3 and 2×4 for Nd [71], 2×4 and 2×7 for Gd [72], Dy [10, 72], and Ho [14], 2×3, c(6×2) and 2×1 for Sm [73], 2×3 and *c*(2×4) for Er [74], 1×5 [17]or 2×3, 2×4, 2×6, and c(6×2) [71, 75] for Yb. As mentioned previously, in the initial stages of 3D silicide growth, several RE metals form silicide NWs.

The formation of these NWs arises from the anisotropic lattice mismatch between the RE silicide and the Si(001) substrate. The RE disilicide NW has a hexagonal AlB_2 structure. The orientation relationships of hexagonal $RESi_2$ on Si(001) are determined to be:

h-$RESi_2(1\bar{1}00)$ // Si(001), h-$RESi_2$[0001] // Si[$1\bar{1}0$], and h-$RESi_2$[$11\bar{2}0$] // Si[110]

as shown in Figures 1.3 (a) and 1.3 (b). The atomic resolution on top of NW shows *p*(1×1) [12, 17] and *c*(2×2) [8, 9, 11, 12, 14] which are consistent with a hexagonal AlB_2 structure.

Comparing the lattice mismatch in *a* and *c* directions of the hexagonal structure with Si(001) 1×1 unit cell, the lattice mismatch in *a* direction is very small (within ± 1.64 % for Y, Sm, Gd, Dy, Ho, Er, and Yb) as shown in Table 1.2. On the other hand, the lattice mismatch in *c* direction is large (over 6.51 %). Because of those anisotropic lattice-mismatch strains, hexagonal $RESi_2$ grows faster in *a* direction than in *c* direction. Therefore, *a* and *c* directions of hexagonal structure correspond to a length and width of NW, respectively, as shown in Figure 1.3 (c).

For $ScSi_2$, the direction of large and small lattice mismatches is opposite, and thus the growth direction of $ScSi_2$ NW is perpendicular to that of other $RESi_2$ NWs. Also, $YbSi_2$

NWs grow in a wide variety of orientations [17]. $YbSi_2$ NWs grow along the [001] direction which is 45 degrees rotated with respect to the other $RESi_2$ NW-growth direction. They also merge into the other NWs running in the different orientation. This behavior might be controlled by larger lattice mismatch (-1.46 %) in *a* direction, and thus there is a competition between different orientations of $YbSi_2$ NWs on Si(001).

When the lattice mismatch is large in both *a* and *c* directions such as $NdSi_2$, three-dimensional (3D) compact silicide islands form instead of elongated NWs [71]. Those 3D islands are also observed in most of the $RESi_2$/Si(001) system [1, 7, 12, 14, 16, 76] depending on the annealing temperatures and annealing durations.

1.1.2.2 Schottky barrier height of RE silicides on Si

Almost all metals can form silicides, but most of them result in high Schottky barrier heights on *n*-type silicon and low barrier heights on *p*-type silicon. Unlike most other silicides, RE silicides produce a high Schottky barrier height of 0.7~0.8 eV on *p*-type Si and a low barrier height of 0.3~0.4 eV on *n*-type Si [24, 25, 49, 56, 60, 77-79] as listed in Table 1.3. This behavior makes them in particular interesting for applications as Ohmic contacts for *n*-type Si [25]. Furthermore, the corresponding high barrier height on *p*-type Si substrates [24] is an interesting property for infrared detectors or photovoltaic applications. In case of $ErSi_{2-x}$/Si diodes, excellent rectifying behavior is observed for *p*-type Si, whereas the electrical characteristics of the film to *n*-type Si are relatively Ohmic at RT and rectifying at low temperatures [49]. Most of the values in Table 1.3 are quite close to one another, which reflects the great physical and chemical similarities of the different RE metals (including Sc and Y).

1.1.2.3 Electrical resistivity of RE silicides

Our knowledge of the electrical properties of RE silicides is very limited and fragmentary. There are only a few reported works on electrical properties of RE silicide thin films. The values of resistivity of RE silicides are summarized in Table 1.4. RE silicide thin layers exhibit an almost metallic behavior. The resistivity decreases linearly with decreasing temperature and tends to a limiting residual resistivity, ρ_o, at very low temperatures. The abrupt decrease of $\rho(T)$ at very low temperatures is due to the antiferromagnetic ordering arising from the incomplete $4f$ shell of the RE^{3+} ion, which is operative below the Néel temperature T_N. La [80], Gd [81-86], Tb [83, 87], Dy [68, 83], Er [29, 49, 83, 84, 86, 88, 89], Tm [29, 62], and Yb [29] have a significant resistivity drop, but Y [29, 88] and Lu [69] do not. In case of $LaSi_{2-x}$ ($0 \leq x \leq 0.4$), there is a superconducting transition at 2.5 K [80].

The resistivity $\rho(T)$ is determined using Matthiessen's rule which includes the various independent scattering mechanisms:

$$\rho(T) = \rho_o + \rho_m(T) + \rho_{e\text{-}ph}(T)$$

where ρ_o and $\rho_m(T)$ are the residual resistivity and the magnetic contribution to the resistivity, respectively. ρ_o arises due to imperfections in the crystalline lattice such as defects and impurities. $\rho_m(T)$ is the magnetic contribution to the resistivity above the Néel temperature T_N and generated by scattering from randomly oriented spins [90]. The temperature dependent term $\rho_{e\text{-}ph}(T)$ is the contribution of the electron-phonon scattering mechanism expressed by the Bloch-Gruneisen formula [91]:

$$\rho_{e-ph}(T) = \rho' T \left(\frac{T}{\Theta_D}\right)^4 \int_0^{\Theta_D/T} \frac{x^5}{(e^x - 1)(1 - e^{-x})} dx$$

where Θ_D is the Debye temperature, ρ' is the high temperature limit of $\rho_{e\text{-}ph}$. At very low temperatures ($\Theta_D/T > 20$), the Bloch-Gruneisen formula can be expressed as $\rho_{ph}(T) \sim T^5$ and at higher temperatures ($T \sim \Theta_D$), the relation is approximated by the linear formula: $\rho_{ph}(T) \sim T$.

Table 1.3 Schottky barrier heights, Φ_B, of RE metals and silicides on *n*- and *p*-type Si substrates.

RE metal or RE silicide	Diode fabrication technique	Φ_B^n (eV)	Methods of measurement	Ref	Diode fabrication technique	Φ_B^p (eV)	Methods of measurement	Ref
Sc, ScSi	TE	0.4	I-V	[77]	TE	0.7	I-V	[77]
Y						0.69	photo	[24]
						0.68	I-V	
$YSi_{1.7}$					TE	0.74	photo	[24]
						0.75	I-V	
Ce					TE	0.63	photo	[78]
Sm	TE	0.9 ± 0.1	photo	[27, 92]				
$GdSi_2$	TE	0.37 ± 0.02	I-V	[25]	TE	0.71 ± 0.03	I-V (n=1.05)	[25]
	VPD	0.32 ± 0.05	photo	[56]				
Tb						0.69	Photo	[24]
						0.68	I-V	
$DySi_2$	TE	0.37 ± 0.02	I-V	[25]				
	VPD	0.32 ± 0.05						
$HoSi_2$	TE	0.37 ± 0.02	I-V	[25]				
$ErSi_2$	TE	0.39 ± 0.02	I-V	[25]				
	VPD	0.32 ± 0.05	photo	[56]				
	TE	0.28	I-V	[49, 79]	TE	0.74	I-V	[49]
Yb					TE	0.64	I-V	[24]
$LuSi_2$	VPD	0.32 ± 0.05	photo	[56]				

TE: thermal evaporation; VPD: vapor-phase deposition; MBE: molecular beam epitaxy; photo: photoemission method;

Table 1.4 Resistivity of RE silicides.

Silicide	Bulk			Film/Si(001)				Film/Si(111)			
	ρ_0 (μΩ cm)	ρ (μΩ cm)	Ref	ρ_0 (μΩ cm)	ρ (μΩ cm)	θ (nm)	Ref	ρ_0 (μΩ cm)	ρ (μΩ cm)	θ (nm)	Ref
Sc_5Si_3		143	[40]								
ScSi		30	[40]	1.5	21		[38]				
$ScSi_{1.66}$		40.6	[40]		38		[38]				
Y_5Si_3	60	375	[94]								
		102	[40]								
YSi		51	[40]								
Y_3Si_5	5.1	101	[29]								
$YSi_{1.7}$	23		[83]					39	69	48	[88]
YSi_2		59	[40]	26		200	[26, 81]				
La_5Si_3	65 (10 K)	210	[94]								
LaSi		340	[40]								
$LaSi_{1.9}$	33		[83]								
$LaSi_{2-x}$	S (< 2.5K)	350	[95]	20 (T)	24 (T)	90	[93]	13	45	30	[80]
(0≤x≤0.4)	ρ_0 = 13	45	[80]	24 (O)	57 (O)			S (< 2.5K)			
Ce_5Si_3	230 (10 K)	330	[94]								
$CeSi_2$		408	[96]								
Pr_5Si_3	90 (10 K)	275	[94]								
$PrSi_2$		202	[96]								

ρ_0: Residual resistivity, ρ: Intrinsic resistivity at RT, θ: Film thickness, (H) hexagonal, (T) tetragonal, (O) orthorhombic structure, S: superconductive below the temperature

Table 1.4 (cont'd)

Silicide	Bulk			Film/Si(001)				Film/Si(111)			
	ρ_0 (μΩ cm)	ρ (μΩ cm)	Ref	ρ_0 (μΩ cm)	ρ (μΩ cm)	θ (nm)	Ref	ρ_0 (μΩ cm)	ρ (μΩ cm)	θ (nm)	Ref
Nd_5Si_3	113 (10K)	288	[94]								
$NdSi_2$		349	[96]								
Sm_5Si_3	95 (10 K)	380	[94]								
Gd_5Si_3	220	410	[98]								
$GdSi_{1.7}$								26 (H)	86 (H)	70, 80	[81]
$GdSi_{1.95}$				58.6	94	68	[85]				
Tb_5Si_3	113	350	[98]								
$TbSi_2$											
$DySi_{2-x}$				31.4 (T)	70 (T)	60~80	[97]	109 (H)	155 (H)	60~80	[97]
				34 (T)	76 (T)	65	[68]	42 (H)	114 (H)	65	[68]
$HoSi_{1.67}$		~220	[99]								
$HoSi_{1.82}$		~260									
Er_3Si_5	19	71	[29]								
$ErSi_{2-x}$	9.5	35	[89]	162.4 (H)	265 (H)	60~80	[97]	41.8 (H)	135 (H)	60~80	[97]
$(0 \le x \le 0.4)$				4.21 (T)	70 (T)			8.5	34	33	[49]
$TmSi_{2-x}$	30	290	[29]	39.65 (H)	113 (H)	66	[62]	34.69 (H)	96 (H)	66	[62]
Yb_5Si_3	140	305	[98]								
Yb	S (< 2.5K)										
Lu_5Si_3	171	375	[98]								
$LuSi_{2-x}$	14	97	[29]	75 (H)	180~500	50	[69]		180~500	50	[69]

1.2 Organization of the thesis

The remainder of this thesis is organized as follows. In Chapter 2, experimental background will be provided. The principles of scanning tunneling microscopy (STM) and low energy electron microscopy (LEEM), and the basic structure of the of Si(001) surface are presented.

From Chapter 3 to Chapter 6, the growth behavior and electrical properties of RE silicides on Si(001) are discussed. In Chapter 3 and Chapter 4, the growth behavior of two different RE silicides, Ho and Sm silicide NWs and/or islands on Si(001) is studied by STM. The results of scanning tunneling spectroscopy (STS) show that $HoSi_2$ NWs and 3D islands are metallic. Chapter 5 contains LEEM studies of growth kinetics of Dy silicide islands on longer length scales and at elevated temperatures that are not accessible by STM. The LEEM studies were carried out at the University of Illinois in collaboration with Dr. W. Swiech of the Frederick Seitz Materials Research Laboratory. In Chapter 6, transport measurements of Dy thin films are presented. The details of ultra-high vacuum (UHV) sample preparation for transport are also provided.

In Chapter 7, suggestions for future work will be described, continuing the themes of this thesis in several different areas.

The Appendices include: a summary of studies of hydrogen on Si(001), a definition of sheet resistance, the principles of two- and four-terminal measurements, a description of the van der Pauw's method, and a list of publications.

Chapter 2 Experimental

In this chapter, the experimental methods used, the basic principles and mechanisms of scanning tunneling microscope (STM) and low energy electron microscope (LEEM), and the basic structures of Si(001) substrate are introduced.

2.1 Experimental and research methods

All experiments except transport measurements were performed in an ultra high vacuum (UHV) system with a base pressure of $< 2\times10^{-10}$ Torr. The chamber was equipped with an STM, a four-grid low energy electron diffraction (LEED) optics, and facilities for sample heating and metal deposition. The Si(001) samples were chemically cleaned, and then outgassed by heating to 975°C. After outgassing, they were flashed briefly at 1175°C to remove surface oxide, and held at 975°C for 10 min, and then cooled slowly to room temperature (RT). The temperatures of the samples were measured using an optical pyrometer. Metals were evaporated from a tungsten wire basket, and the evaporation rate was calibrated by a quartz-crystal thickness monitor.

For holmium (Ho) deposition, typical evaporation rates were 0.05~0.09 monolayers (ML) per minute [1 ML = $1/a_{Si}^2$ = $1/(0.384\ nm)^2$ = 6.78×10^{14} atoms/cm^2 for Si(001): see p.35 for details of silicon surface] and total coverages studied were between 0.06~0.9 ML. For dysprosium (Dy) and samarium (Sm) depositions, typical evaporation rates were 0.1~0.6 ML/min and 0.03~0.09 ML/min and total coverages were between 0.16~3 ML and 0.05~1.5 ML, respectively. The chamber pressure remained below 1×10^{-8} Torr during evaporation, and immediately recovered to below 5×10^{-10} Torr after the metal source was turned off. All growth was done at a substrate temperature of 600°C unless

specifically mentioned. All STM imaging and LEED observation were done at RT.

2.2 Scanning tunneling microscopy (STM)

STM was invented in 1981 [100, 101] by G. Binnig and H. Rohrer, IBM in Zurich, Switzerland, gaining them the 1986 Nobel prize in physics. Their first STM image of Si(111)-7×7 reconstructed surface with its display of individual atoms [102] was the stimulus that initiated many STM projects all over the world.

STM is a powerful technique for studying the structural and electronic properties of surfaces with real-space atomic resolution. When a sharp metallic tip is brought close enough (~10 Å) to a conducting surface and a bias voltage (mV~10V) is applied, the tunneling current flows between the tip and sample. The lateral resolution is about 1 Å whereas a vertical resolution up to 0.01 Å can be achieved. In addition, STM can be used not only in UHV, but also under other environments such as in air or in solution.

Recently, atoms and molecules have been able to be moved controllably on surfaces, either by sliding them by means of the tip or by lifting them off the surface by the tip and depositing them at a different location [103-116]. The atomic-scale manipulation of surfaces by STM-tip is a promising candidate for future nanoelectronic device applications.

2.2.1 Basic principles of STM

The operating principle of the STM is based on the quantum mechanical phenomenon of tunneling. Electrons transmit through a vacuum barrier between two conductors, in this case the sample and the tip, when they are brought very close together. A simple

understanding of this principle follows from consideration to the solution of the Schrödinger equation for a one-dimensional square barrier of height V_0, as shown in Figure 2.1. For a particle of energy $E < V_0$ incident on this square barrier from the left, the solutions of the Schrödinger equation have the form:

$$\psi(x) = \begin{cases} e^{+ikx} + \mathrm{Re}^{-ikx} & (x < 0) \\ Ae^{-\kappa x} + Be^{+\kappa x} & (0 \le x \le s) \\ Te^{+ikx} & (\mathrm{s} < x) \end{cases} \quad (1)$$

where $\hbar k = \sqrt{2mE}$, $\hbar\kappa = \sqrt{2m(V_o - E)}$, R and T are reflection and transmission coefficients, respectively, and A and B are constants.

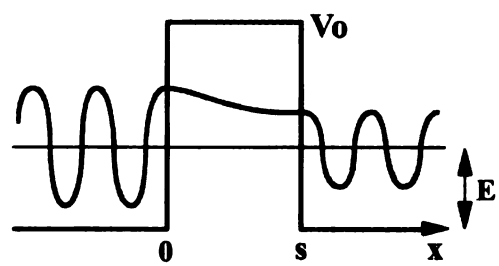

Figure 2.1 Wave function ψ for an electron with kinetic energy E tunneling a thin potential barrier of height V_0 and width s. The wave function is oscillatory in the left and right regions of the barrier. Within the barrier, the wave function decays exponentially.

The wave function ψ decays exponentially into the classically forbidden region $0 \le x \le s$ with a decay length of $1/\kappa$. For an electron at the Fermi level of a conductor with a work function ϕ, this decay length would be $1/\kappa = \sqrt{\hbar^2/2m\phi}$ ($V_0 - E$ is just the work function). Since most work functions are around 4~5 eV, the decay length is typically $1/\kappa \sim 1$ Å. When a barrier of width s is much thicker than the wave function decay length of $1/\kappa$, the transmission probability T, or the tunneling current J decays

exponentially as:

$$J = \frac{\hbar k}{m}|T|^2 \propto e^{-2\kappa s} = e^{-2s\sqrt{2m\phi/\hbar^2}} \quad (2)$$

Thus the tunneling current drops by an order of magnitude for every 1 Å. For the tip-sample distance of ~10 Å, the tunneling current is a few nA.

For tunneling between two conductors with a voltage difference V across the gap, only the states within eV above or below the Fermi level can contribute to tunneling; electrons in states within eV below the Fermi level on the negative side tunnel into empty states within eV above the Fermi level on the positive side. In the case of Figure 2.2, the tunneling current flows from a tip to a sample, since the positive bias voltage is applied to the sample. When the sample is positively and negatively biased, it is called "empty" and "filled" states, respectively.

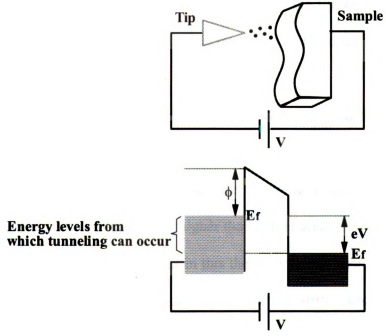

Figure 2.2 Energy diagram for tunneling between a tip and a sample. Tunneling is possible only when there are empty states on the right. Such empty states are created when eV is applied to lower the Fermi level on the right.

2.2.2 STM data acquisition and image processing

STM can be operated in several imaging modes: constant current mode, constant height mode, barrier height imaging, and scanning tunneling spectroscopy (STS). Most of the STM images presented in this thesis are acquired in the constant current mode unless specifically mentioned.

In the constant current mode, the tip is scanned in the two lateral (x and y) dimensions, while a feedback circuit constantly adjusts the tip height to keep the current constant. The position of the tip is accurately controlled by the piezoelectric drivers. The tip position is recorded as a function of the x-y surface coordinates as shown in Figure 2.3. All STM bias voltages were applied to the sample with the tip at virtual ground.

According to equation (2), the tunneling current reflects the surface topography only when the work function does not change during scanning. In addition, the tunneling current changes with the electronic state of the tip and sample. Therefore, essentially, STM image shows the electronic density of states at the sample surface instead of surface topography of the sample.

The most common method of displaying STM data is to construct a grayscale image where the brightness represents the surface electronic density: Brighter areas are higher density of electrons at the surface. For easy understanding, brighter areas can be considered topographically higher than darker areas.

In all of the STM images in this thesis, only minimal image processing has been done, consisting of planar background subtraction, drift correction, or contrast adjustment in order to extract the desired information. Image processing was done with either "Image SXM" which is the public domain image analysis software written by Steve Barrett [117],

or NOeSYS "Transform" software for the correction of image distortion.

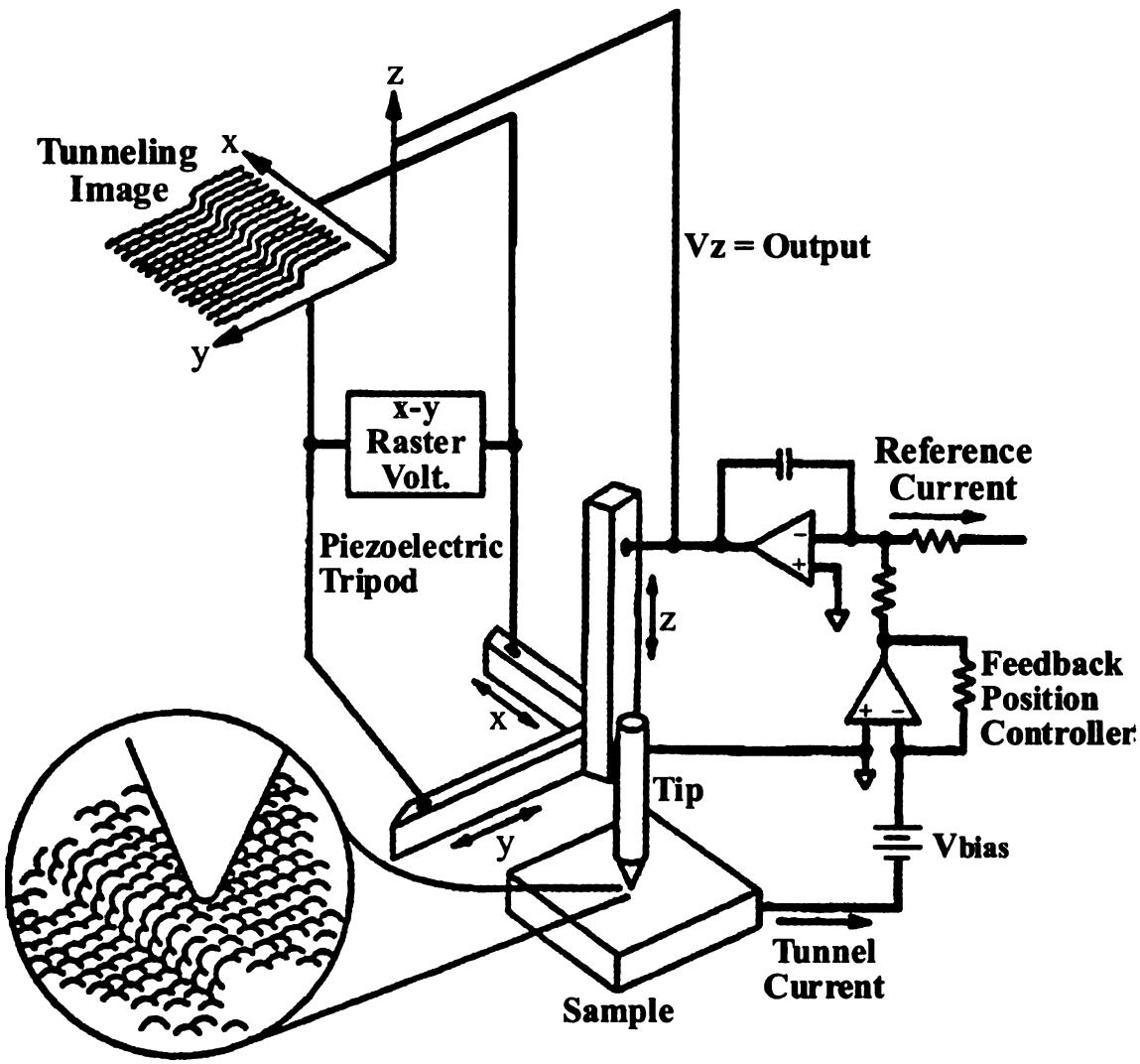

Figure 2.3 Schematic diagram of an STM [118]. A metallic tip is mounted on a piezoelectric tripod actuator which can move the tip in the *x-y* plane of the sample surface, and in the *z* direction normal to the surface, with atomic resolution.

2.2.3 Scanning Tunneling Spectroscopy (STS)

STS is used for studying local surface density of states with atomic resolution because the probe apex is very small consisting of a few atoms. The sensitivity of STS to

electronic structure can be a tremendous advantage over other spectroscopic methods such as ultraviolet photoelectron spectroscopy (UPS), X-ray photoelectron spectroscopy (XPS), Auger electron spectroscopy (AES), and inverse photoelectron spectroscopy (IPES). A single tunneling spectrum can show surface states both above and below the Fermi level simultaneously, at the same spatial location.

Figure 2.4 shows the schematic of an STS experiment. The sample-tip separation is fixed and the tunneling current I is recorded as a function of applied bias voltage V (I-V curve). Since I-V characteristics depend exponentially on the sample-tip separation, the logarithmic derivative $\frac{d\ln I}{d\ln V}$ or the normalized differential conductivity $\frac{dI/dV}{I/V}$, which is a dimensionless quantity, is generally used to remove the influence of sample-tip separation. The approximate expression for the tunneling current [119] is given by:

$$I \propto \int_0^{eV} \rho_s(E)T(E)dE \quad (3)$$

where ρ_s is the surface density of states, T is the transmission probability in equation (1), and V is the applied sample voltage. After the first order approximation of E (or V), the normalized differential conductivity $\frac{dI/dV}{I/V}$ can be expressed as:

$$\frac{dI/dV}{I/V} \approx \frac{\rho_s(eV)}{\frac{1}{eV}\int_0^{eV} \rho_s(E)dE} \quad (4)$$

Therefore, $\frac{dI/dV}{I/V}$ is proportional to the normalized surface density of states.

For the STS data plot and graphing, WaveMetrics "Igor Pro" software was used.

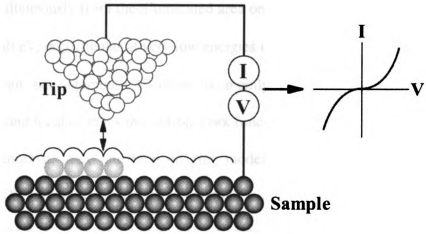

Figure 2.4 Schematic of an STS experiment. An STM tip is held above the sample, and the current is measured while the voltage is ramped. This measures the conductivity in the surface normal direction.

2.3 Low energy electron microscopy (LEEM)

LEEM is a relatively new electron microscopy technique for *in-situ* real-time studies of surface dynamics, such as epitaxial growth, phase transitions, interface formations, strain relaxation phenomena, and chemisorption over a wide temperature range. LEEM was developed by E. Bauer and his student W. Telieps in 1985 [120] after its invention by E. Bauer in 1962 [121]. R.M. Tromp and M.C. Reuter designed a new LEEM that has higher resolution and wider capability of the instrument in 1991 [122].

Electron microscopes use beams of electrons instead of light, and magnets instead of lenses. However, the working principle of electron microscopes is more or less the same as in the optical microscope. In LEEM, the sample is illuminated with a well-collimated beam of low-energy electrons which diffract from the sample. The diffracted electrons are then used to form an image. In contrast to STM in which the probe tip is scanned back and forth across the surface to form images, all pixels are

imaged simultaneously from the illuminated area on the surface. At low energies of the order of 1~50 eV, in particular at very low energies (< 10 eV), high brightness and a good resolution can be obtained. Contrast is mainly produced by diffraction, surface topography, and local changes in electron work function and/or electron density. For the diffraction contrast, there are three imaging modes in LEEM as shown in Figure 2.5: bright-field (BF) imaging, tilted bright-field (TBF) imaging, and dark-field (DF) imaging. When electron beam is on the optical axis of objective lens, and the specularly reflected (0,0) beam is used to form a BF image. TBF image is also formed by using (0,0) beam, but with tilted incident angle. In DF imaging, non-specular diffracted beam (any beam other than (0,0) beam) is used. TBF or DF contrast must be used for the observation of azimuthally rotated domains, because domains are equivalent at normal incidence and they do not produce contrast in BF.

For the interface contrast, surface steps are surrounded by stress and strain fields which cause local changes of the diffraction conditions. The resulting diffraction contrast may enhance or reduce the geometric phase contrast.

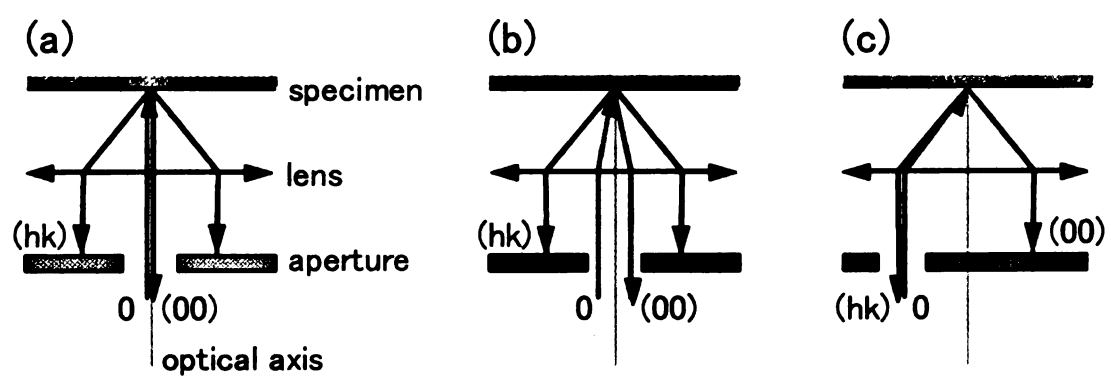

Figure 2.5 Diffraction contrast in LEEM (a) Bright field, (b) tilted bright field, (c) dark field.

The spatial resolution is determined mainly by the spherical and chromatic aberrations of the objective lens and by diffraction at the contrast aperture. Lateral resolution of LEEM is 5~10 nm on video-rate imaging [123, 124] , but in principle the best resolution of 3 nm is achievable [123]. Diffraction contrast provides depth resolution of a single atomic layer.

2.3.1 Basic physics of the low-energy electron interaction with surface: Elastic scattering and inelastic scattering

For the low energy electrons in the LEEM geometry, inelastic scattering and elastic backscattering are important (No forward scattering). At low energies, the elastic backscattering does not increase monotonically with nuclear charge because the incident electrons can 'feel' the details of potential distribution of neighbor atoms. Incident electrons can be reflected from surfaces with a high reflection coefficient within the first few atomic layers when their energy is in a band gap. (When electrons have wave vectors at the Brillouin zone at which the band gaps occur in the band structure, they fulfill the Laue condition $\mathbf{k} - \mathbf{k_0} = 2\pi\mathbf{h}$ and are reflected.) Or they can penetrate deeply into the crystal when the incident energy E matches to $E(\boldsymbol{k})$ states in the solid.

The electron energy loss mechanism in solids is excitation of valence band electrons. For low energy electrons, the inelastic processes do not involve inner electron shells because of the insufficient energy but only outer electron shells. The electron density in the valence band (or Fermi energy E_F) is nearly constant for most materials, and it gives the 'universal curve' of inelastic mean free path $\lambda = 1/\mu$, where $\mu(E)$ is the attenuation coefficient for *inelastic* scattering.

$\mu(E)$ dominates $\nu(E)$, the attenuation coefficient for *elastic* scattering, above the

threshold E_T for plasmon excitation. E_T varies with E_F from 11 to 27 eV when E_F changes from 5 to 15 eV [125]. At $E>E_T$, inelastic scattering processes determine the penetration depth corresponding to a mean free path in the range of 0.3 to 1 nm. On the other hand, at $E<E_T$, elastic backscattering determines the penetration depth. The influence of inelastic scattering is negligible at $E<E_T$, because the inelastic mean free path increases rapidly as the incident energy E decreases. Therefore, energies up to 20~30 eV are advantageous for LEEM from the point of view of electron-surface interaction.

2.3.2 LEEM instrumentation and image acquisition

The schematic of a LEEM instrument (IBM Type I) is shown in Figure 2.6. The design of LEEM requires full UHV compatibility. The sample is held at about –20 kV to decelerate the electrons to a few eV at the sample surface. The magnetic objective lens is entirely at ground potential. The incident beam comes from a Schottky emission gun and is focused with condenser lenses, an octupole stigmator, and steering coils. Condenser lenses relay the cross-over point into the back focal plane of the objective lens in which a diffraction pattern is formed as in Figure 2.7. Two sets of steering coils control the shift and tilt of the e-beam. A beam-separating deflection magnet is necessary because the reflected beam has to be separated from the illuminating beam. The reflected electrons pass through the deflection magnet again and enter the imaging column. The image is projected onto a channel plate screen. LEEM images are recorded using a video camera outside the vacuum chamber and digitized for analysis at 30 frames per second.

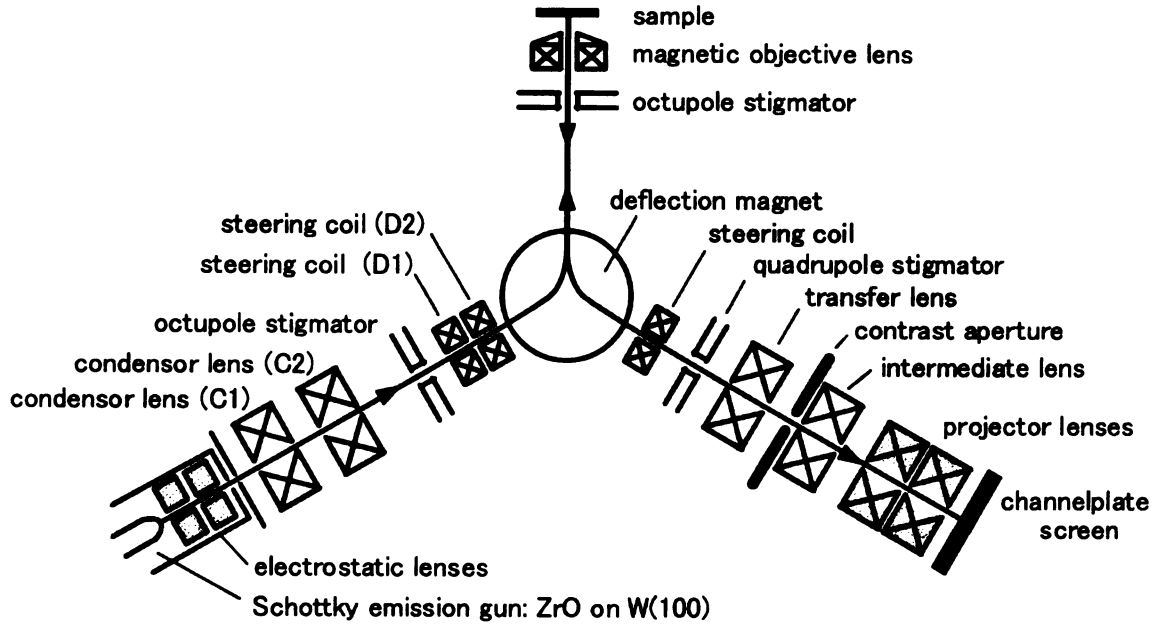

Figure 2.6 Schematic of LEEM instrument (IBM Type I).

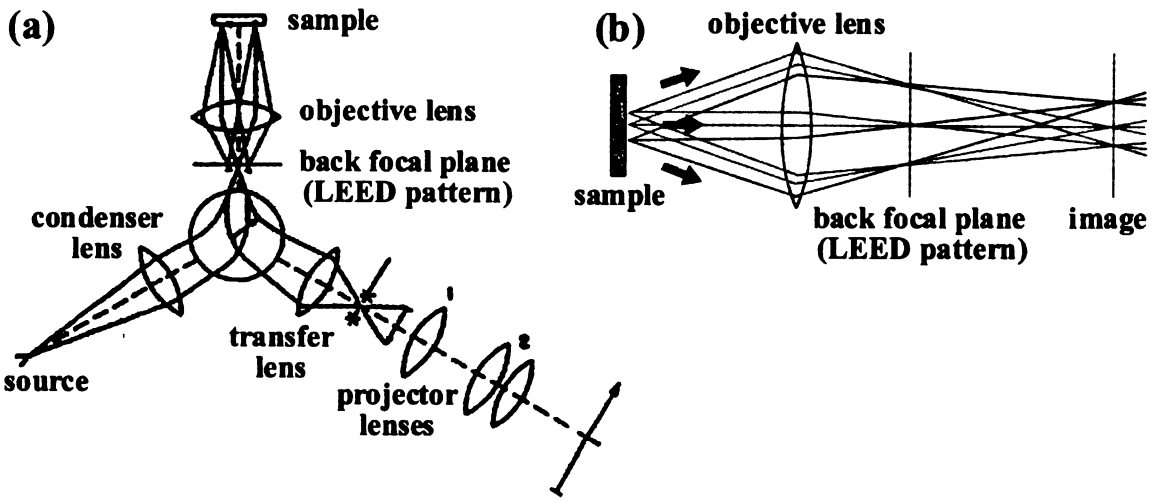

Figure 2.7 Schematic ray diagrams for LEEM [126, 127].

2.4 Si (001) surfaces

On unreconstructed Si(001), each Si atom on the top layer has two broken covalent bonds (dangling bonds) with a nearest-neighbor separation of $a_{Si} = a_o/\sqrt{2} = 0.384$ nm, where a_o equals the Si lattice constant of 0.543 nm as shown in Figure 2.8 (a). a_{Si} is defined as a unit length of Si(001) surface and a square 2D lattice in Figure 2.8 (b) represents a 1×1 unit cell. Since this surface is not an energetically favorable state, the surface reconstruction occurs to lower the surface energy. Adjacent atoms on the surface move toward each other at the expense of inducing a large surface stress and make a new bond forming a "dimer" [Figure 2.8 (c)]. Intradimer atomic distance is 0.24±0.02 nm which has been studied experimentally [128-130] and theoretically [131-135].

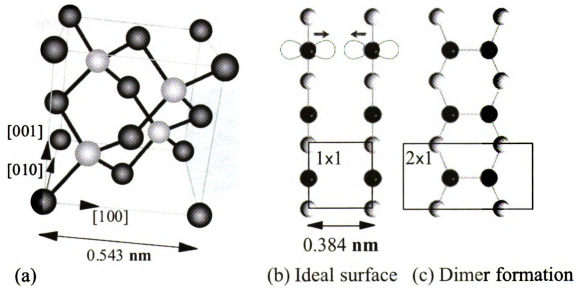

Figure 2.8 (a) Diamond structure of silicon, and (b), (c) top view of model of the dimer reconstruction on Si(001).

The valence electrons of an isolated Si atom are in 3*s* and 3*p* atomic orbitals. These orbitals are 'hybridized' into sp^3 orbitals [136] when the atoms arrange in tetrahedral structures like in a diamond-lattice crystal. As shown in Figure 2.9, in the dimer surface state, the π states, π bonding and π^* anti-bonding, are formed from even and odd combinations of the left and right dangling bond state. On the other hand, σ states, σ bonding and σ^* anti-bonding, arise from the bridge states [137]. During STM imaging, the spacial distribution of these π bonding and π^* anti-bonding states are probed by electrons tunneling out of and into the sample, giving the filled- and empty-state images, respectively. In the filled states, bright maxima appear in the center of dimers where electron density is localized as shown in Figure 2.9 (a). Since each Si atom has one dangling bond which is a half-occupied electron state, two corresponding maxima appear at both edges of the imer with small rounded shape in empty states as shown in Figure 2.9 (b). White rectangles marked in Figures 2.9 (a) and 2.9 (b) correspond to a black rectangle showing the dimer position in Figure 2.10.

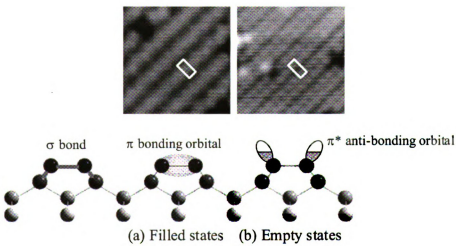

Figure 2.9 (a) filled- and (b) empty-state STM images of Si(001) surface with a side view of Si dimer model. 2×1 unit cells corresponding to the dimer position are marked.

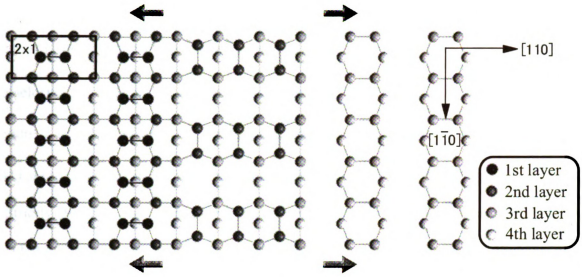

Figure 2.10 Schematic drawing of Si(001) 2×1 reconstructed surface consisting of three terraces. Si atoms on top, second, third, and fourth layers are shown with black, dark gray, light gray, and white colors, respectively. The height of the terrace lowers from left to right. The directions of surface stress are marked with black arrows.

Si dimers form rows consisting of $p(2\times1)$ structure on Si(001) surface as shown in Figure 2.10. Since the dimer rows are rotated by 90° on each atomic step on the surface, the Si(001) surface has two degenerate phases 2×1 and 1×2 and its surface stress field is anisotropic. The surface is under tensile stress along the dimer row direction and under compressive stress normal to the dimers [138] as marked with black arrows in Figure 2.10. In this thesis, the Si dimer row direction is defined as [1$\bar{1}$0] and the Si dimerization direction as [110] as indicated in Figure 2.10.

The LEED pattern of a Si(001) surface provides 1/2-order spots corresponding to the 2×1 periodicities on the surface as shown in Figure 2.11. The diffraction spots with white (gray) circles in Figure 2.11 are diffracted from the highest and lowest (the middle) terraces in Figure 2.10, respectively. For real space imaging, one of these diffraction spots can be used. In LEEM images, the intensity changes sharply at the step with TBF

or DF contrast. Figure 2.12 shows the DF images of Si(001) surface with opposite contrast [139]. When $(\frac{1}{2}, 0)$ diffraction spots (marked with white circles in Figure 2.11) are selected for a DF image, 2×1 terraces appear bright, while 1×2 terraces appear dark [Figure 2.12 (a)]. When $(0, \frac{1}{2})$ diffraction spots (marked with gray circles in Figure 2.11) are selected, the diffraction contrast appears opposite [Figure 2.12 (b)].

Strictly speaking, there are several other reconstructions on Si(001) surface due to the buckled (twisted) dimers at low temperatures: $p(2\times1)$ asymmetric phase, $p(2\times2)$ phase, or $c(4\times2)$ phase [135, 140-147]. However, at RT, a fast flip-flop motion of the buckled dimers is thermally activated, which mostly shows symmetric dimer rows in the STM images. Therefore, it is plausible to assume that the Si(001) surface has a symmetric $p(2\times1)$ structure as far as the experiments are performed at RT.

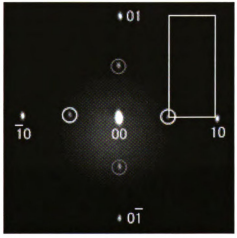

Figure 2.11 LEED pattern of a Si(001) surface with 2×1 superstructure. $(\frac{1}{2}, 0)$ and $(\frac{\bar{1}}{2}, 0)$ diffraction spots and $(0, \frac{1}{2})$ and $(0, \frac{\bar{1}}{2})$ diffraction spots are indicated with white and gray circles, respectively. 2×1 unit cell is marked with a white rectangle as well.

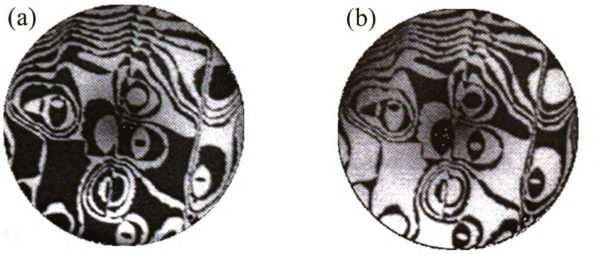

Figure 2.12 Dark-field LEEM image of Si(001) surface with opposite contrast. Images (a) and (b) are acquired using one of the diffraction spots with (a) white and (b) gray circles, respectively [139].

Chapter 3 Ho growth on Si(001): surface reconstructions and nanowire formation

In this chapter, the growth behavior of Ho on Si(001) is described in detail, including coverage dependence, nanowire (NW) and 3D island formation, 2D substrate surface reconstructions, and the results of scanning tunneling spectroscopy (STS).

3.1 Results and discussion

3.1.1 Coverage dependence

Figure 3.1 shows the coverage dependence of Ho growth on Si(001) at 600°C. The horizontal axis is the metal coverage in monolayers (ML), and both LEED pattern and topography are shown. Black circles are the metal coverages at which experiments were done. There are roughly two types of topographies, both of which are comprised of a 2D reconstructed substrate, coexisting with 3D silicide islands. The LEED patterns reflect the 2D ordered surface. For low metal coverage, $\theta \leq 0.4$ ML, the islands are highly elongated NWs with typical width 1.1~7.3 nm, height 0.2~1.2 nm, and lengths 100~500 nm [Figure 3.2 (a)]. As the coverage increases, 3D compact silicide islands are found of varying shape [Figure 3.2 (b)]. NWs and 3D islands coexist at coverages above 0.4 ML. A 2×4 phase dominates the 2D reconstructed surface structure at most of the coverages shown in Figure 3.1 although clean Si 2×1 dimer rows are observed in places below 0.18 ML. In addition, a 2×7 phase appears in the 0.40~0.55 ML coverage regime, and it coexists with the 2×4 phase.

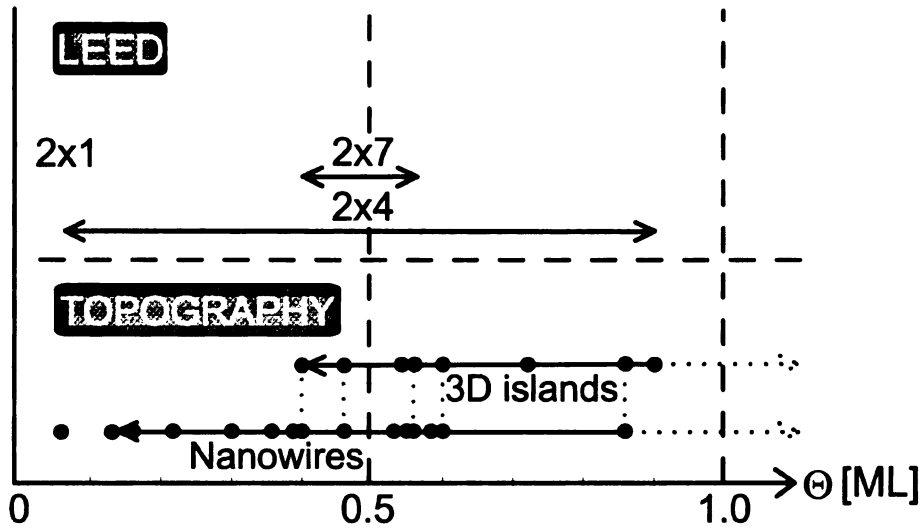

Figure 3.1 Coverage dependence of LEED patterns and topography for Ho growth on Si(001) at 600°C.

The percentage of the 2D surface covered with Ho in either the 2×4 or the 2×7 phase is not monotonic with coverage as shown in Figure 3.3. At lowest coverage, 0.06 ML, there is only 2×4 structure and bare Si on the 2D surface. As the coverage is increased, most of the 2D surface is covered by the 2×4 structure, and both the density and the average height of NWs increase. When 3D islands appear, the percentage of the 2D surface covered by 2×4 decreases and bare Si substrate reappears. From mass conservation, Ho atoms moved from the 2D surface to the 3D islands. This fact implies 3D silicide islands are preferable to either a Ho reconstructed substrate, or the elongated NWs in terms of accommodation of Ho. The initial stage of NW growth can be described as Stranski-Krastanov. However, the reappearance of bare Si once 3D islands are formed shows that the growth mode changes to Volmer-Weber at higher coverage.

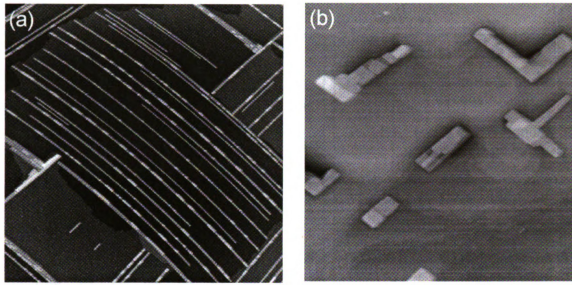

Figure 3.2 Two 400×400 nm^2 images of $HoSi_2$ NWs and 3D islands. (a) NWs formed by 0.36 ML of Ho. Each NW grows on a single terrace. (b) As the coverage is increased (0.90 ML), 3D compact silicide islands are found.

3.1.2 NWs and 3D islands

As seen in Figure 3.2 (a), every NW grows on a single atomic terrace, and runs along a $<1\bar{1}0>$ type direction. Each NW usually terminates at a step edge or at a perpendicular NW, but perpendicular NWs are on different terraces and do not cross. At higher coverages, rectangular islands can nucleate at the intersection of NWs. The NWs in Figure 3.2 (a) are comparatively long as the step density on this substrate is low. On substrates with higher step density, steps can flow to accommodate NWs, as shown in Figure 3.4 (a). In this image, the steps curve to follow the NWs so that each remains on a single terrace. Nevertheless, there is some limit to the number of steps that can flow to accommodate a NW, and so NW length is still limited by step density.

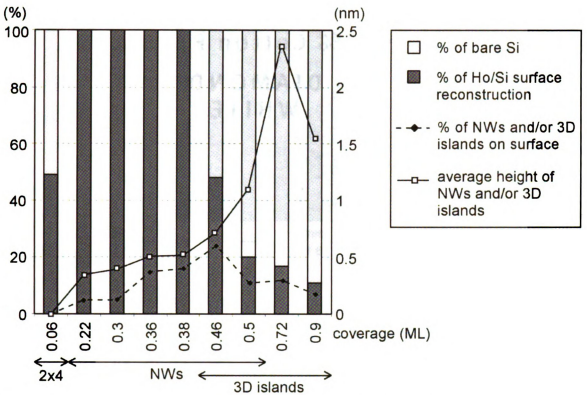

Figure 3.3 Relationship between coverage and the percentage of surface covered with Ho surface reconstruction, NWs, and 3D islands.

As shown in Figure 3.4 (a), there are two distinct NW morphologies; one is triangular in cross section, and the other is rectangular. Figures 3.4 (b) and 3.4 (c) are cross-sectional profiles of these NWs. At 0.2~0.3 ML, both types of NWs are seen at equal probability. As the coverage increases up to 0.4 ML, rectangular NWs are more often observed and at the same time NWs tend to form parallel bundles as shown in Figure 3.5 (a). While the narrow NWs in the edges of bundles are mostly triangular in cross section, those in the middle of the bundles are certainly rectangular.

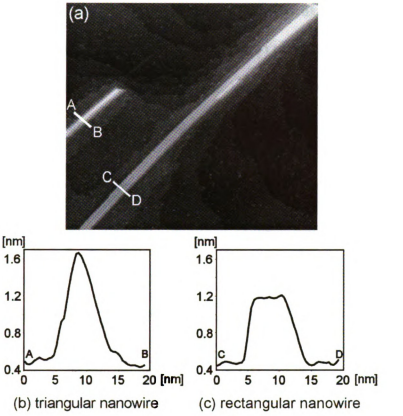

Figure 3.4 (a) Triangular (left) and rectangular (right) NWs at 0.3 ML (200×200 nm^2). Steps on the substrate flow to accommodate the NWs. Lines A-B and C-D show the locations of the cross sections shown in (b) and (c).

The structure of the rectangular NWs can be understood in terms of the bulk silicide $HoSi_{1.7}$, which has a hexagonal AlB_2 type structure, with the [0001] axis parallel to the surface, and the $[11\bar{2}0]$ direction along the long axis of the NW as shown in Figure 1.3 in Chapter 1. Atomic resolution on the top surface of rectangular NWs shows $c(2\times2)$ periodicity [Figure 3.5 (b)]. The same periodicity is seen on the surface of second layer NW growth. The height of the second layer NW is always 0.33 nm which corresponds to 1 bulk $HoSi_2$ unit cell height [9]. This height includes one metal layer and two Si layers. The apparent height of the first NW silicide layer varies because the electronic properties of the NW and substrate surface are different. The structure of the triangular

cross section NWs is not clear from the STM data, but it is likely that it has the same epitaxy characteristic as the rectangular NW with the $[11\bar{2}0]$ direction lying along the long axis. It is possible that these triangular wires are simply a minimal width rectangular wire with perhaps a different step edge structure.

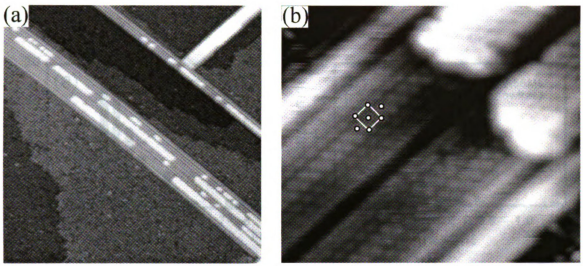

Figure 3.5 (a) Bundled NWs with second layer growth at 0.36 ML (90×90 nm^2). (b) Atomic resolution on bundled NWs (12×14 nm^2). A single $c(2\times2)$ unit cell is marked with a white square.

When the widths and the heights of silicide islands are measured, it is clear that the 3D compact silicide islands have widely varying dimensions whereas those of NWs are restricted to narrow ranges. Figures 3.6 (a) and 3.6 (b) are the distributions of the width and the height of single NWs and compact silicide islands, respectively.

The top graphs show the details of the leftmost bar on the bottom graphs, and include data from both isolated NWs and NWs in bundles. Narrower widths shown by 'A' come from the edges of bundled NWs, and except for these data, there is no particular difference between the widths of bundled and isolated NWs. For isolated NWs,

rectangular NWs are wider than triangular ones. The most probable NW width is in the range in 2~3 nm, which corresponds to 5~9 silicide cells wide. The maximum NW width of ~5 nm can be related to the 6.8 % lattice mismatch between $HoSi_2$ and Si substrate along the *c* axis. This was also noted for $DySi_2$ NWs which have similar lattice mismatch and maximum width [9].

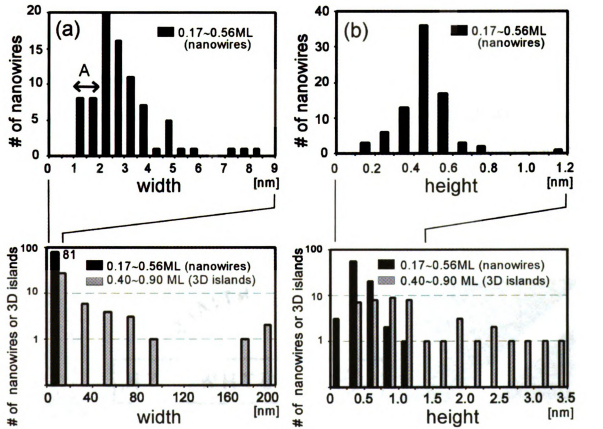

Figure 3.6 The distributions of (a) the width and (b) the height of single NWs and 3D islands.

The most probable NW height is 0.4~0.6 nm, which is 1~2 bulk $HoSi_2$ unit cell heights. Although we have statistics for comparatively few compact 3D islands, it is clear that both the width and the height of the compact silicide islands are spread over a much

wider range than those for the NWs. The fact that the 3D islands' sizes can exceed the maximum width of the NWs suggests that their growth is not coherent. It is possible that there are dislocations at the interface that do not propagate up to the surface of the islands. However, for most islands there is no clear indication of such dislocations from the STM images, unlike the dislocation networks observed for other epitaxial silicides grown on Si(111) [148]. Further work with transmission electron microscopy (TEM) would be useful in clarifying the structure of the islands.

3.1.3 Two dimensional substrate surface reconstructions

Figures 3.7 (a) and 3.7 (b) are empty- and filled-state images of slightly different areas of the same surface with 0.55 ML Ho. Coexistence of 2×4 and 2×7 structures on the 2D surface is observed. A NW runs diagonally across the image, and gray circles on both Figures 3.7 (a) and 3.7 (b) indicate the same physical position on the surface.

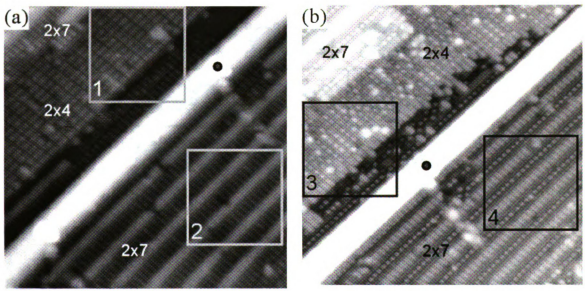

Figure 3.7 (a) Empty- and (b) filled-state images of slightly different areas of the same surface with 0.55 ML Ho showing both 2×4 and 2×7 structures (30×30 nm^2). The position of gray circle on the NW in (a) corresponds to that in (b).

Figures 3.8 (a) and 3.8 (b) show the empty-state (1.76 V) and filled-state (-1.76 V) images of the 2×4 structure corresponding to the square areas numbered by '1' and '3' in Figure 3.7, respectively. These images are of the same area of the surface. Both figures have three sets of 2×4 unit cells along the Si dimer row direction [$1\,\bar{1}\,0$] outlined in white. In the empty-state image [Figure 3.8 (a)], three maxima are visible in each

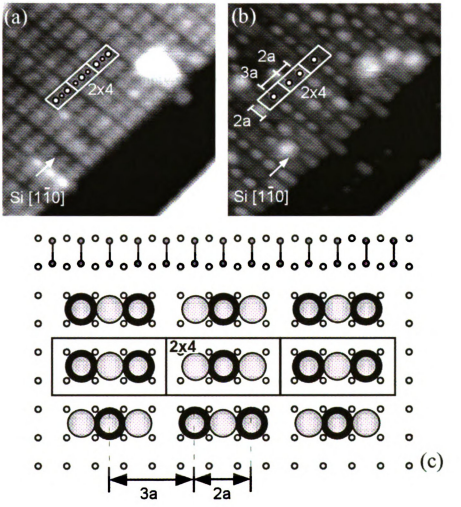

Figure 3.8 (a) Empty-state (1.76 V) and (b) filled-state (-1.76 V) images of the 2×4 phase in the reconstructed surface shown in Figure 3.7 (10×10 nm^2). (a) and (b) correspond to the square areas numbered by 1 and 3 in Figure 3.7, respectively. (c) Line drawing showing the empty-state (gray circles) and filled-state (dark circles) maxima of the 2×4 structure. Clean 2×1 Si dimer positions are shown as a reference on the topmost row.

2×4 unit cell. There are two types of maxima that are lined up in one of two possible configurations; a darker maximum (small circle) between brighter maxima (big circles), or a brighter maximum between two darker maxima. Either combination is equally probable. In the filled state image [Figure 3.8 (b)], the contrast between the two types of maxima is reversed, and more pronounced. Bright oval maxima appear in the positions of the darker empty-state maxima.

By comparison of both bias images with respect to the Si(001) substrate, the registration of empty and filled state of maxima of the 2×4 structure can be diagrammed as in Figure 3.8 (c). All the empty-state maxima are positioned in what would normally be Si dimer positions, and the filled-state maxima are located in the same positions as the darker empty-state maxima. The overall character of the 2×4 structure is the same as that seen for Dy on Si(001) [10].

Figures 3.9 (a) and 3.9 (b) show enlargements of the 2×7 structure corresponding to the square areas numbered by '2' and '4' in Figure 3.7, respectively. Two types of rows (row A and B) are observed and three types of maxima are visible in both biases. In the empty-state image [Figure 3.9 (a)], row A consists of oblong maxima elongated along the 7× direction. Row B consists of three maxima and the smaller maximum is located between two larger maxima. In the filled-state image, row A includes paired maxima, and row B has three maxima and the larger maximum is located between two smaller maxima. The registration of 2×7 phase can be obtained by comparison with positions of 2×4 phase from both bias images.

The registration and approximate spatial extent of the empty- and filled-state maxima of the 2×7 structure are diagrammed in Figure 3.9 (c). This illustration contains five

rows (row ABABA) which are seen in Figure 3.9 (b), and the clean 2×1 Si dimer row positions are shown on top as a reference. The empty-state maxima of the bright features in row A and B are represented by gray oblongs and circles, respectively. The filled-state maxima are illustrated using dark circles in three sizes. In row A, the paired filled-state of maxima are located on the bridge site, and an oblong empty-state maximum is positioned off bridge site. In row B, in both states, the middle maximum is located on

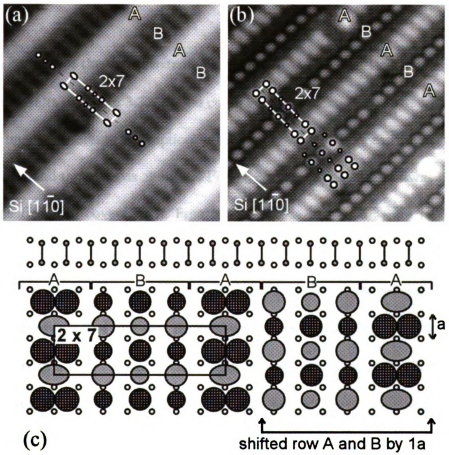

Figure 3.9 (a) Empty-state (1.76 V) and (b) filled-state (-1.76 V) images of the 2×7 phase extracted from Figure 3.7. (a) and (b) correspond to the square areas numbered by 2 and 4, respectively. A 2×7 unit cell consists of three types of maxima in rows labeled A and B in both images. (c) Line drawing showing the empty-state (gray circles and oblongs) and filled-state (dark circles) maxima of the 2×7 structure. 2×1 Si dimer positions from the clean surface are shown as a reference on the topmost row.

the bridge site, and both edges of the maxima are positioned off bridge site. Row A or B in the both states often shifts by $1a_{Si}$ in the perpendicular direction to the 2×1 Si dimer row ($[1\bar{1}0]$ direction). In this sense, the overall periodicity should be defined as the coexistence of 2×7 and c(2×14) unit cells. For simplicity, we denote this phase by 2×7. Since at a given coverage Ho metal can be distributed in NWs and both the 2×4 and the 2×7 reconstructed surfaces, it is difficult to decide the density of Ho in the 2×7 structure. Therefore we are not proposing an atomic structure for the 2×7 phase.

3.1.4 Ho content of the 2×4 substrate reconstruction and the NWs

From the results in Figure 3.3, one can compare experimental coverage with calculated coverage under different assumptions for Ho content of both the 2D substrate reconstruction and the NWs as shown in Figure 3.10. The calculation was done on the basis of the first five coverages in Figure 3.3. The table on the right in Figure 3.10 shows two different assumptions of Ho content. The first assumption is the number of Ho atoms per 2×4 unit cell on the 2D surface: 'A', 'B', and 'C' indicate one, one and half, and two Ho atoms per 2×4 unit cell, respectively. The second assumption is the number of metal layers in a NW: '1' and '2' represent one and two metal layers in the minimum height NW, respectively. Here we also assumed that each metal layer in the NW has a density of 1 ML as implied by the bulk crystal structure as shown in Figure 1.3 in Chapter 1. The coverages shown in the graph on the left hand side where calculated under the six possible combinations of assumptions enumerated to the right, along with the measured percentage of the surface covered by bare surface, 2×4, and NWs as shown in Figure 3.3. The best model should come closest to the diagonal line. Error bars are

omitted for clarity. The error in coverage is less than 20 %, and the error in the vertical position of the symbols is less than 10 %.

As can be seen in the figure, the best fit is for 'B1' which implies 1.5 Ho atoms per 2×4 unit cell, and one layer of metal atoms in the minimum height NW. There is one layer of metal atoms in each bulk unit cell of the silicide, and so this is not a surprising result. Nevertheless, this coverage dependent analysis was necessary to deduce this fact since the geometric height of the first layer NWs as seen by STM was bias dependent. We cannot exclude the possibility that the minimum height NW may have more than two layers of Si atoms, but this depends in some sense on the definition of where the substrate ends and the NW begins.

The 1.5 Ho atoms per 2×4 unit cell is somewhat more surprising. The simplest interpretation is that one of the two types of filled state maxima is associated with a single Ho atom. As shown in Figure 3.8, two possible configurations of 2×4 unit cells alternate on the surface, one with a bright-dim-bright arrangement of maxima, and the

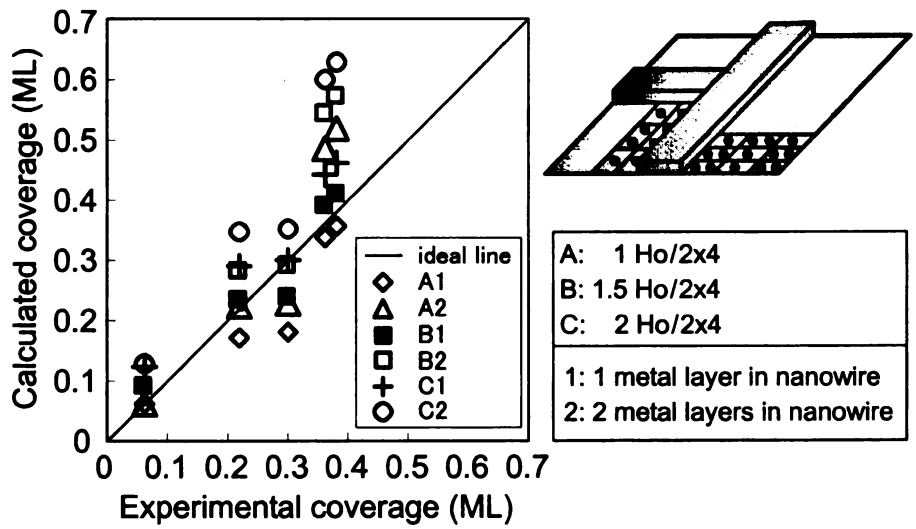

Figure 3.10 Comparison of experimental coverage with calculated coverage under different assumptions of Ho content (see text).

other with a dim-bright-dim arrangement. There are equal populations of both types of unit cells, meaning that the average density of either type of maxima is 1.5 per 2×4 unit cell. This is not to say necessarily that the maxima seen in either bias is a Ho atom. In the case of the Dy 2×4, there appears to be three metal atoms per unit cell and yet bright and dim maxima are seen as well. Determination of the atomic structure of the 2×4 surface and the origin of the differences between the Ho and Dy induced structures will require complementary information from other surface analytic techniques.

3.1.5 Scanning Tunneling Spectroscopy

Figure 3.11 (a) shows the STS *I-V* curves and normalized spectra of a NW, 3D island, and the adjacent areas of reconstructed substrate at 0.56 ML. Since the 2D surface is reconstructed by Ho, the spectrum of the substrate is different from that of clean Si. The upper three curves are the actual *I-V* data, and the lower three curves are the normalized differential conductivity $\frac{dI/dV}{I/V}$. STS data were acquired at every pixel of the image shown in Figure 3.11 (c) which is a partial image of Figure 3.11 (b). Each STS curve is an average of the data taken in the area enclosed by the solid or dashed lines. The normalized spectra show that the NW has non-zero conductivity at near-zero bias. Figure 3.11 (d) is the STS *I-V* curves at near-zero bias voltage. It is clear that the *I-V* curve of the NW is steeper than that of 3D island and the reconstructed substrate. Although both NW and 3D island are metallic, NW has greater surface conductivity. Bulk $HoSi_2$ is metallic with a conductivity of approximate 4.4×10^3 $[\Omega\ cm]^{-1}$ at RT [99].

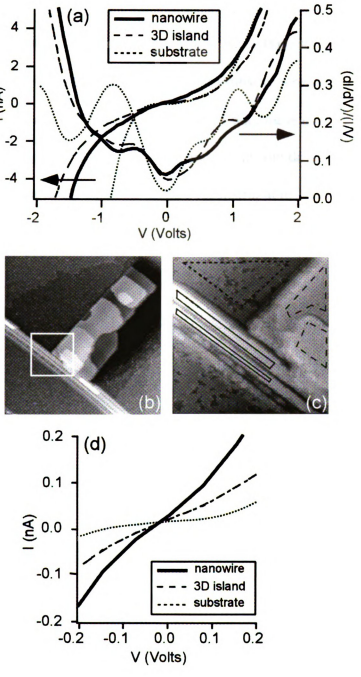

Figure 3.11 (a) The STS *I-V* curves and normalized spectra for a NW, 3D island, and the reconstructed substrate. The surface topography is shown in (b) (150×150 nm^2). The image (c) is a partial image of (b). Each STS spectrum was averaged from the STS data acquired in the areas shown by solid or dashed lines in the STM image shown in (c) (40×40 nm^2). (d) Magnification of the STS *I-V* curves at near-zero bias voltage.

3.2 Conclusions

We have studied the initial stages of Ho growth on the Si(001) surface. Metal coverages between 0.06~0.9 ML were deposited onto substrates heated to 600°C, and the samples were then cooled to RT for study by STM. Under these growth conditions, Ho forms either highly elongated silicide NWs or compact 3D silicide islands, together with several possible Ho induced 2D substrate surface reconstructions. STS spectra reveal that the NWs are more metallic than either the large 3D islands or the reconstructed substrate.

Chapter 4 Samarium induced surface reconstructions of Si(001)

In this chapter, the growth behavior of Sm on Si(001) is described, including coverage dependence, 2D substrate surface reconstructions, and 3D island formation. Also we provide the first report that there are two different surface reconstructions: a lower coverage 2×3 phase and a higher coverage 3×2 phase.

4.1 Results and Discussion

4.1.1 Coverage dependence

Figure 4.1 shows the coverage dependence of Sm growth on Si(001) at 600°C. The horizontal axis indicates the metal coverage in monolayers (ML), and both LEED patterns and topography as seen by STM are shown. Gray circles are the metal coverages at which the experiments were performed. The error in coverage is less than 20 %. Generally, a 2×3 phase dominates the 2D reconstructed surface for the coverages

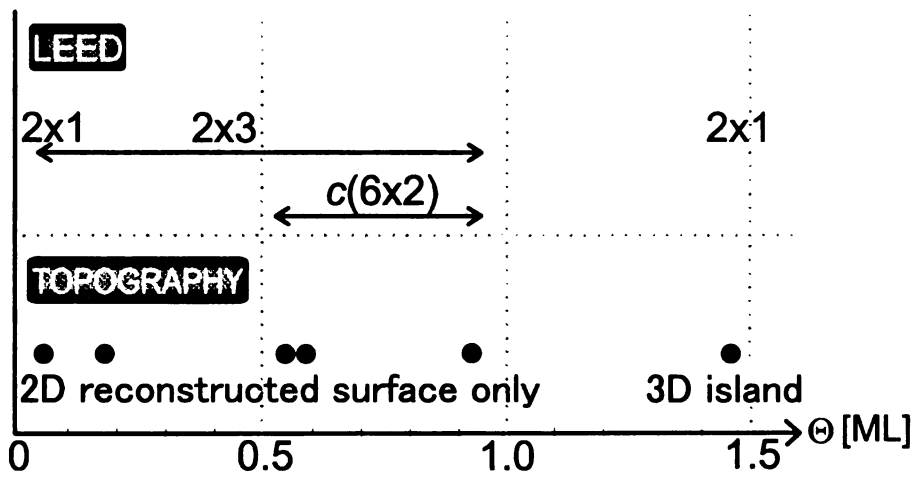

Figure 4.1 Coverage dependence of LEED patterns and topography for Sm/Si(001) at 600°C.

below 1 ML. At very low coverages (below 0.07 ML), only a 2×1 LEED pattern is observed. A $c(6\times2)$ phase coexists with 2×3 phase above 0.54 ML as in the LEED pattern shown in Figure 4.2.

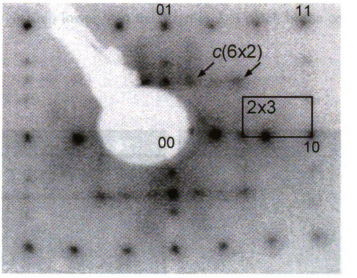

Figure 4.2 LEED pattern of Sm/Si(001) at 0.54 ML shows 2×3 (black rectangle) and $c(6\times2)$ (black arrows) periodicities. The LEED pattern was obtained from the surface shown in Figures 4.8 (c) and 4.9 (a). The electron beam energy is 63 eV.

4.1.2 General surface structure evolution with metal coverage

An overall description of all of the ordered surface reconstructions will be presented, followed by a more detailed discussion of each surface structure.

At low coverages, $\theta < 0.2$ ML, there are two Sm associated surface structures: a 2×3 ordered phase and a more sparse zigzag chain structure. Figure 4.3 shows a pair of images (15×15 nm^2) in (a) empty and (b) filled states at 0.067 ML. Two 2×3 unit cells on the different terraces are shown with white and black rectangles on each image. The rectangles are slightly distorted as a result of drift while acquiring the images. Also shown are line traces taken from both images along the dashed lines *A* shown in Figures

4.3 (a) and 4.3 (b). A small terrace of clean 2×1 Si dimers is seen in the central part of the image. Zigzag chains of brighter features are seen on the upper part of the terrace, and there is a small patch of brighter ordered 2×3 reconstruction on top of this terrace as well. Surrounding the central terrace are larger ordered areas of 2×3 reconstruction that are one atomic height step lower than the brighter 2×3 patch in the central lower part of the image.

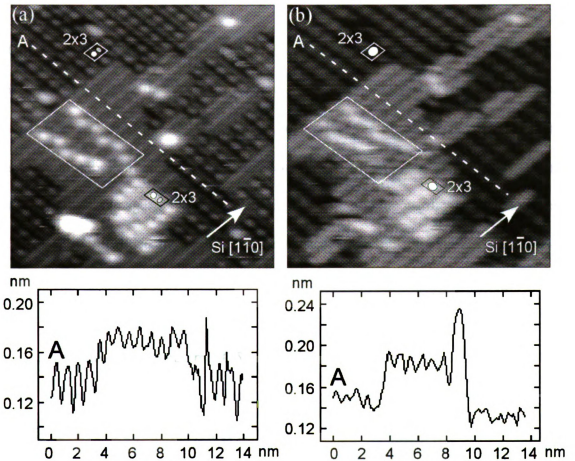

Figure 4.3 (a) Empty-state (1.90 V) and (b) filled-state (-1.91 V) STM images of the same area showing 2×3 phase and the zigzag chain structures at 0.067 ML (15×15 nm^2). Cross-sectional profile along the line A is shown on the bottom of each image.

The trace along *A* in both images shows that the large areas of 2×3 are lower than the central 2×1 terrace at both bias polarities [0.019 (0.039) nm lower in empty (filled) states]. This makes it reasonable to assume that the 2×3 is geometrically lower than the 2×1. The height of the zigzag chains is similar to that of the 2×3 area on top of the central terrace [about 0.116 (0.065) nm in empty (filled) states], and the upper 2×3 structure is about 0.12 nm higher than the lower 2×3, which is about the single atomic height step (0.125 nm) on the Si(001) surface. This supports the view that the 2×3 structure on both terraces is in fact the same.

One can describe this 2×3 structure as being built up on top of a Si(001) terrace, or embedded in a terrace that is one level lower. For the purposes of this thesis, we will describe the 2×3 as being embedded into the level of the central terrace. This means that the upper 2×3 structure is effectively embedded in the terrace above the one that is not visible in this image. With this definition, the ordered reconstruction is denoted as a 2×3 structure embedded in a 2×1 clean Si terrace, implying that the 2× periodicity is along the same direction as the Si dimerization direction of the surrounding clean Si areas.

In the medium coverage regime ($0.5 < \theta < 1$ ML) the surface looks at first glance to be similar to the lower coverages. Figure 4.4 shows an image of a surface at 0.59 ML, which is covered in a combination of 2×1 Si and a 2×3 reconstruction. However, closer examination reveals several differences. Firstly, the uncovered Si areas have a large concentration of dark missing dimer defects that are arranged in zigzag patterns, rather than bright protrusions. Secondly, the 3× periodicity of the "2×3" is perpendicular to the Si dimer rows in the 2×1 terrace at a similar height in the center of this image. This

is perpendicular to the 2×3 structure seen at the lower coverages, and so this structure is denoted as "3×2". It should be noted that anti-phase defects in this 3×2 structure can also produce a $c(6\times2)$ periodicity that can also be seen in the LEED patterns as shown in Figure 4.2.

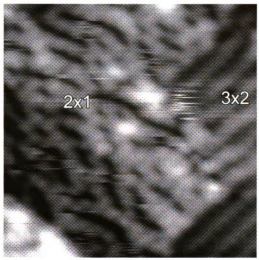

Figure 4.4 15×15 nm^2 image of a surface at 0.59 ML. Both a 3×2 phase and a highly defected Si 2×1 surface are seen. The bias voltage is –1.77 V.

In the high coverage regime ($\theta > 1$ ML), 3D silicide islands are seen in coexistence with a 2×1 reconstructed substrate. An STM image of a 3D island is shown in Figure 4.5. It is known that Sm-Si system forms Sm_3Si_5 and $SmSi_2$ compounds [42, 44]. Although no elongated structure is observed for 3D Sm silicide compounds in this work, it has been reported that $SmSi_{2-x}$ forms NWs on vicinal Si(001) substrate at the same growth temperature [6]. This structural difference in the formation of silicide is likely due to the metal deposition rate, sample annealing temperature, and substrate type.

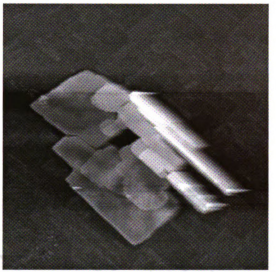

Figure 4.5 Sm silicide island at 1.46 ML (300×300 nm^2).

4.1.3 The low coverage 2×3 and zigzag chain structures

Figures 4.6 (a) and 4.6 (b) show empty-state (1.57 V) and filled-state (-1.57 V) images of the same area at 0.067 ML, respectively. Two 2×3 unit cells are marked with white rectangles on each image. An out-of-phase boundary is also indicated with a dashed line. This type of phase shift in 2×3 structures can be frequently observed. Si dimer rows running diagonally are shown in the lower right region.

In both empty and filled states, two round maxima can be observed with different size and contrast within each 2×3 unit cell. Here, the bright and dim maxima are represented by circles and ovals in the 2×3 unit cell, respectively, on each image. By comparing both bias images of Figures 4.6 (a) and 4.6 (b) with respect to the Si(001) substrate, the registration of empty (white) and filled (gray) states of maxima of the 2×3 structure can be diagramed as in Figure 4.6 (c). The 2×3 maxima are in registry with the centers of Si dimers on any line that is drawn along the Si dimer row directions and 3× periodicities are aligned along the $[1\bar{1}0]$ direction, as is readily apparent from these images. The

registry in the perpendicular direction has been determined from other similar images that are not shown here. This registry of features is different from Ragan *et al.*'s result of Sm on vicinal Si(001) where Sm atoms are positioned on the trenches between the Si dimer rows [6].

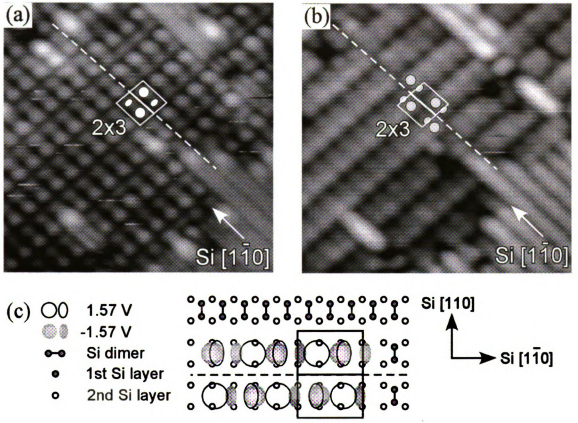

Figure 4.6 (a) Empty-state (1.57 V) and (b) filled-state (-1.57 V) STM images of the same area showing 2×3 phase at 0.067 ML (10×10 nm^2). There are out-of-phase boundaries shown with dashed lines. Two 2×3 unit cells are marked with white rectangles. (c) Line drawing showing the empty-state (white circles and ovals) and filled-state (gray circles and ovals) maxima of the 2×3 structure.

On the line drawing, in empty states, the maxima (white circles and ovals) are situated almost in the center of an underlying Si square lattice consisting of four Si atoms in each

corner, but they are slightly off center. The filled-state maxima (gray circles and ovals) lie between two Si atoms, which is shifted by half a_{Si} (a_{Si} = 0.384 nm) from the underlying Si square lattice. The dim maxima in empty states (white ovals) are positioned almost between the filled-states maxima, while the bright maxima in empty states (white circles) positioned on the dark region of filled states.

In fact, the number and the appearance of the maxima appearing in STM images are bias dependent. In empty states, below 2.56 V, two maxima can be seen with different contrast in the 2×3 unit cell [Figures 4.3 (a) and 4.6 (a)]. Above 2.74 V, only one maximum is visible (not shown). In filled states, below –1.85 V, there are two maxima in the 2×3 unit cell [Figure 4.6 (b)], while only one maximum can be seen above –1.90 V [Figure. 4.3 (b)]. The bias can also affect the relative height of the 2×3 structure and the 2×1 clean Si surface.

Zigzag chain structures are also observed perpendicular to the Si 2×1 dimer rows as shown in Figures 4.3 (a) and 4.3 (b). The maxima of the zigzag chain structures in empty and filled states are located over the trenches between the Si dimer rows. The features of maxima in 2×3 structure and zigzag chain structures appear the same, although they look different due to a tip effect in Figure 4.3 (a). Figure 4.7 (a) shows the more detailed features of zigzag chain structures with surrounding buckled Si dimers. An area of 2×3 phase can be also seen in the lower right area. In this bias voltage (-1.82 V), the maxima of dimerlike pairs can be observed to have an oblong shape. Comparing the two filled-state images [-1.91 V for Figure 4.3 (b), and -1.82 V for Figure 4.7 (a)], the paired maxima in Figure 4.7 (a) are positioned over the large maximum in Figure 4.3 (b). The dimerlike pairs are $2a_{Si}$ wide in [110] direction and shifted by $1a_{Si}$ in $[1\bar{1}0]$ direction

resulting zigzag chain structures. Since these dimerlike pairs have a width of $2a_{Si}$, there is not enough space to align straight on the trenches with a $2a_{Si}$ periodicity, and thus zigzag chains are generated. However, they can align in a row with a $3a_{Si}$ periodicity forming 2×3 structure as indicated with a rectangle *A* in Figure 4.7 (a).

The maxima in the zigzag chain structure can move along the dimer rows under repeated scanning with STM, and so the pattern of zigzag chain structure slightly changes from image to image. In fact, the movement of zigzag chain causes noise in STM images as appears in the oval area *B* in Figure 4.7 (a). However, the arrangement of 2×3 reconstruction in the small patch does not change even after 10 scans.

In addition, Sm zigzag chain structures induce buckling of the Si dimer rows with *c*(4×2) arrangement in which the pattern of buckling is out of phase as illustrated in Figure 4.7 (b). A *c*(4×2) unit cell is marked with a black rectangle. The Si dimer buckling extends possibly more than 20 dimers along a row without decay. However, the buckling does not affect the adjacent row: if there is no Sm atom in a certain row, the buckling does not occur in this row even though there are Sm atoms forming zigzag chain structures in the adjacent rows. This implies that the interaction between Sm and Si atoms in the same row is very strong, whereas the Sm-Si interaction in the perpendicular to the dimer rows is ignorable.

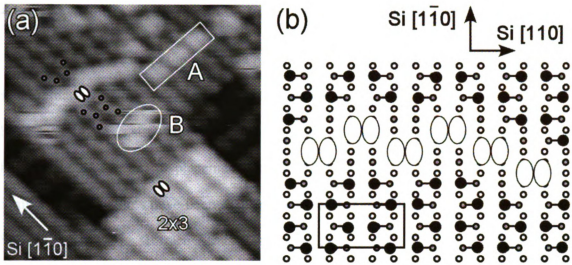

Figure 4.7 (a) Filled-state (-1.82 V) image of zigzag chain structures with buckled Si dimers below 0.1 ML (10×10 nm^2). The 2×3 unit cell is also shown as a pair of two maxima on the lower right area. (b) Line drawing illustrating the zigzag chain structures with surrounding buckled Si dimers. This dimer buckling causes $c(4\times2)$ periodicity. A $c(4\times2)$ unit cell is marked with a black rectangle.

The comparison of the experimental coverage with the percentage of the 2D surface covered with Sm provides a result that there is one Sm atom in 2×3 unit cell. This is again different from Ragan *et al.*'s result which suggests two Sm atoms in a 2×3 unit cell [6]. It is not possible to propose a model for this phase based on the limited amount of information that we can deduce from the STM data. However, we note that the appearance, bias dependence, and registration of STM maxima are all very similar to that observed for a Ba induced 2×3 phase on Si(001) [149]. Ba is divalent with an ionic radius of 0.135~0.163 nm and so it might be expected to behave similarly to divalent Sm (ionic radius 0.113 nm). However, the Ba model proposed in ref [149] requires 2 metal atoms per unit cell.

4.1.4 The medium coverage regime 3×2 and *c*(6×2) phases

As noted previously in the coverage regime ($0.5 < \theta < 1$ ML), the surface is covered in a combination of highly defective Si 2×1, and Sm reconstructed 3×2 and *c*(6×2). A large-scale image is shown in Figure 4.8 (a). The unusual step structure is a signature of large scale Si adatom displacement during the formation of a reconstructed surface. Similar step structures have been seen in the case of B on Si(001) [150, 151] and Ge on Si(001) [152, 153]. Terrace *A* has a straight step edges (S_A step) which run along the dimer row direction, and terrace *B* has jigsaw-shaped step edges (S_B step). Both terraces are covered with the same surface structures: the mixture of 3×2 and *c*(6×2) phases, and Si dimer rows with zigzag defect structures.

In Figure 4.8 (b), the area of the front edge of the jigsaw shape on terrace *B* shows the alternate terraces *A* and *B*. 3×2 and *c*(6×2) phases can be seen in the four corners of the image and Si dimer rows with diagonal rows of missing dimer defects appear in the middle. Close-up image of zigzag defects is shown in Figure 4.8 (c). The ends of zigzag defects are indicated with white or black arrows in Figures 4.8 (b) and 4.8 (c). The angles between Si dimer rows and the zigzag defects ($0^\circ \leq \theta \leq 90^\circ$) vary from 41 to 76 degrees depending on the surface area. These missing dimer defects relieve strain due to a low density of Sm atoms substituting into the Si surface. The Sm atoms do not show up directly in the empty state images, but they make the filled state images of the 2×1 structure appear disordered.

Figures 4.4 and 4.8 (b) shows the coexistence of Si 2×1 and the 3×2 phase. From this image, the 3×2 phase is measured to be about 0.079 (0.078) nm below the surrounding Si 2×1 areas in empty (filled) states. This measured height is slightly different from that of the lower coverage 2×3 structure, and once again, the reconstruction is rotated by 90°.

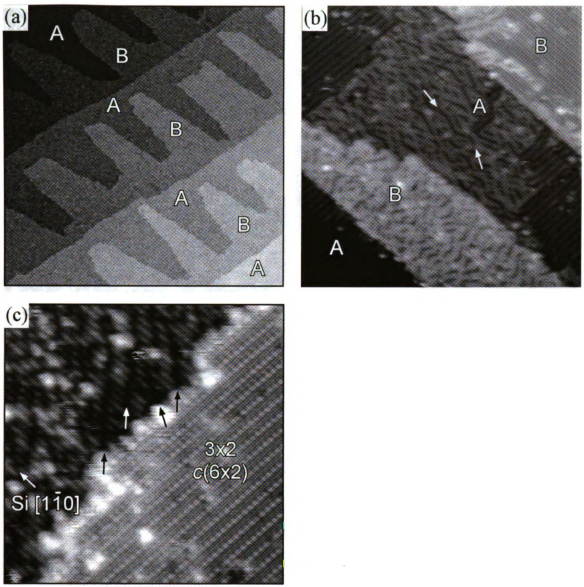

Figure 4.8 (a) Large-scale STM image of a surface consisting of two types of step edges. Straight step edges (S_A step) run along the dimer row direction on terrace *A*, and terraces *B* have jigsaw-shaped step edges (S_B step). (b) Both types of terraces consist of 3×2 and *c*(6×2) phases and Si 2×1 dimer with zigzag defects shown with white arrows. (c) Close-up image of zigzag defects on Si dimer rows. The ends of four zigzag defect structures are marked with black and white arrows. All three images were at different Sm coverages: (a) 0.93 ML, (b) 0.59 ML, and (c) 0.54 ML. The image sizes are (a) 300×300 nm^2, (b) 50×50 nm^2, and (c) 25×25 nm^2. Bias voltages are (a) –2.31 V, (b) –1.77 V, and (c) 1.28 V.

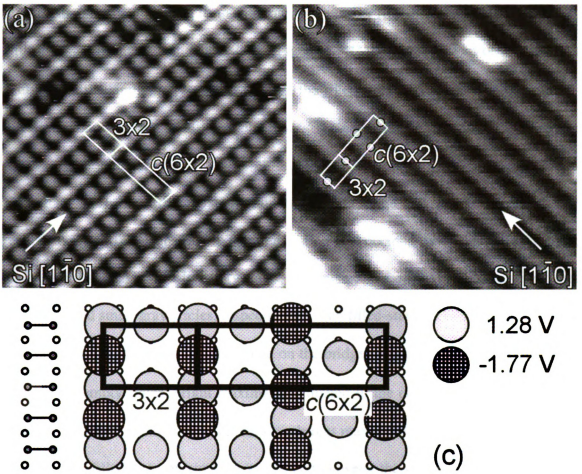

Figure 4.9 10×10 nm^2 images in (a) empty states (1.28 V) and (b) filled states (-1.77 V) showing 3×2 and *c*(6×2) phases at different coverages: (a) 0.54 ML and (b) 0.59 ML. Both 3×2 and *c*(6×2) unit cells are marked with white rectangles on each image. (c) Line drawing showing the empty-state (gray circles) and filled-state (dark circles) maxima of the 3×2 and *c*(6×2) structures. Si dimers are shown on the leftmost row as a reference.

Figures 4.9 (a) and 4.9 (b) show the empty- and filled-state images of 3×2 and *c*(6×2) structures, respectively. Both 3×2 and *c*(6×2) unit cells are marked with white rectangles on each image. The STM images were acquired from the surfaces at different coverages. In empty states [Figure 4.9 (a)], two types of round maxima are observed with slightly different contrast. Bright and dark maxima appear alternatively with a $1.5a_{Si}$ periodicity in the perpendicular to the dimer rows (along the [110] direction). The

bright and dark maxima each form rows along the dimer row direction ([1 $\bar{1}$ 0] direction) with a $2a_{Si}$ periodicity. In filled states [Figure 4.9 (b)], only one type of maximum is visible. In the similar way as empty states, the filled-state maxima lie along the [1 $\bar{1}$ 0] direction with a $2a_{Si}$ periodicity forming rows. These rows appear along [110] direction with a $3a_{Si}$ periodicity.

Figure 4.9 (c) shows the registration of the maxima in the 3×2 and *c*(6×2) phases with respect to the Si(001) substrate. The registration was decided by the same surface area which is not shown here. In empty states, the bright and dark maxima are distinguished with large and small gray circles, respectively. The filled-state maxima are marked with dark circles. All the maxima are located on the bridge site in both biases. For the 3×2 structure in empty states, bright maxima are situated in the center of underlying 1×1 Si lattice, while dark maxima locating between bright maxima lie on the two underlying Si atoms. The filled-state maxima are positioned between the empty-state bright maxima on the same rows. When the positions of the maxima are shifted by $1a_{Si}$ in the dimer row direction, *c*(6×2) structure can be obtained. Thus 3×2 and *c*(6×2) phases have basically the same structure. The number of Sm atoms per 3×2 unit cell is definitely more than 2 according to the experimental coverages (0.54 and 0.59 ML). However, this coverage can be affected by the possibility that 3D silicide compounds sparsely exist somewhere on the surface which STM did not find. When the coverage increases to 0.93 ML, more than 90 % of the surface is covered with Si 2×1 with zigzag defects and few 3×2 phase can be observed, although the LEED pattern shows 2×3, *c*(6×2), and 2×1 phases.

4.2 Conclusions

In the initial stage of Sm deposition on Si(001) at 600°C, the surface is reconstructed with a 2×3 phase. Sm-induced zigzag chain structures coexist with a 2×3 structure. STM observations show that the appearance of the 2×3 structure is bias-dependent. As the coverage is increased, a second 3×2 phase appears with a co-existing *c*(6×2) phase. The 3×2 phase is different in appearance from the lower coverage 2×3 phase. At higher coverages, large 3D Sm silicide islands are found. This research was partially supported by NSF grant DMR-0305472.

Chapter 5 Topographic evolution of Dy silicide on Si(001): Shape transitions from nanowires to 3D islands

In this chapter, we show that $DySi_2$ NWs can be formed with a uniform width by controlling the deposition rate and the deposition duration, which will play an important role for nanodevice assembly. The shape transition from NWs to 3D islands is studied by scanning tunneling microscopy (STM). Low energy electron microscopy (LEEM) is used to study Dy growth on longer length scales that are not accessible by STM. Dynamic behavior and growth of 3D Dy disilicide islands at elevated temperatures are reported.

5.1 Results and Discussion

5.1.1 STM experiments

Figure 5.1 shows STM images of $DySi_2$ NWs at 0.58 ML (a) before and (b) after annealing at 600°C for 8 minutes. As shown in Figure 5.1 (a), almost the whole surface is covered with a 2×7 substrate reconstruction. There are also some NWs with a comparatively uniform width of 7 times the lattice constant of silicon a_{Si} (= 0.384 nm). Formation of NWs with uniform widths with $7a_{Si}$ may be attributed to coexistence with the well-ordered 2×7 substrate reconstruction.

A more detailed image of the 2×7 superstructure is shown in Figure 5.2 (a). Two unit cells are marked with white rectangles. The detailed atomic structure of Dy 2×7 superstructure on Si(001) surface is reported by B.Z. Liu *et al.* [72]

Rapid deposition provides only 2×7 superstructure on the 2D surface regardless of the metal coverage. Six different metal coverages from 0.19 to 0.84 ML were obtained by

adjusting the deposition rates and keeping the deposition time fixed for rapid deposition experiments. Surface morphology at those coverages only consists of 2×7 superstructure on 2D surface and NWs for 3D structure. More NWs are observed at higher coverages and NWs tend to bundle above ~0.8 ML. On the other hand, 2×7 superstructure dominates on 2D surface at any coverage between 0.19 and 0.84 ML.

After 8 min annealing at 600°C, bundled NWs are more often observed and there are more second layer growth on top of the NWs as shown in Figure 5.1 (b). In comparison with 'before' annealing, the NW width distribution 'after' annealing is broader because of the presence of bundled NWs. However, the overall percentage of the surface occupied by NWs does not change significantly 'before' (15.1 %) and 'after' (18.5 %) annealing.

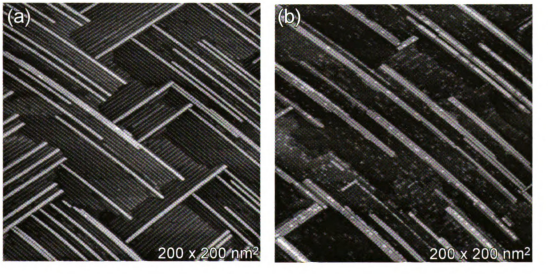

Figure 5.1 STM images of $DySi_2$ NWs at 0.58 ML (a) before and (b) after annealing at 600°C for 8 minutes. (a) Dy was deposited at 600°C. Almost all the 2D surface is covered with 2×7 stripe structure and NWs have comparatively uniform width distribution. 2×7 phase generally disappears after 1 min annealing at 600°C. (b) After annealing, 2×4 superstructure coexists with bare silicon. More bundled NWs are observed and the width of NWs becomes wider. There is also more second layer growth on top of the NWs.

The 2×7 superstructure is swept away and a disordered 2×4 superstructure appears with bare silicon on the 2D surface as shown in Figure 5.2 (b). Two 2×4 unit cells are marked with white rectangles. The 2×4 superstructure consists of one or two round bright maxima in filled states. The detailed atomic structure of Dy 2×4 phase on Si(001) is explained by B.Z. Liu *et al.* [10]

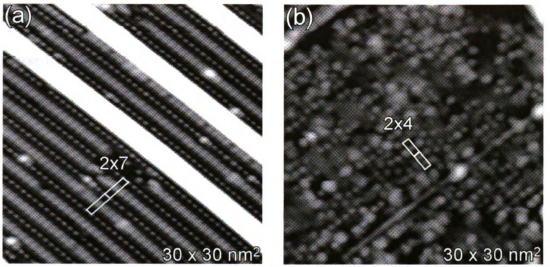

Figure 5.2 Small-scale images of (a) and (b) in Figure 5.1 showing (a) 2×7 (-1.80 V) and (b) 2×4 (+1.04 V) reconstructed surface around NWs. Two unit cells are marked with white rectangles in each image.

Generally, more than 1 min annealing at 600°C replaces the whole 2×7 superstructure by 2×4 superstructure coexisting with bare silicon surface. Immediate disappearance of the 2×7 phase can be seen by LEED when the sample heating starts. 2×1 and ×4 LEED patterns are observed during annealing at 600°C after the 2×7 phase disappears.

The extreme sensitivity of the 2×7 superstructure to annealing is characteristic of the overall ease with which the 2×7 can be converted to the 2×4 structure. It can be further noted that the balance between 2×7 and 2×4 on the substrate is also sensitive to

deposition rate. In earlier work where the Dy deposition was slower, 2×7 and 2×4 coexist on the substrate over a range of metal coverages. The present results show that fast deposition with post deposition quenching results in a pure 2×7 substrate phase which can be converted rapidly to 2×4 by annealing.

Figure 5.3 shows the evolution of the 0.58 ML sample shown in Figures 5.1 and 5.2, after repeated annealing cycling. The percentage of the surface covered with 2D substrate reconstructions (2×7, 2×4, or 2×1) and 3D structure (NWs or islands) is expressed in the vertical axis. Annealing processes are shown in the horizontal axis. The sample was annealed seven times in total: 1st annealing (600°C 8min), 2nd (600°C 20

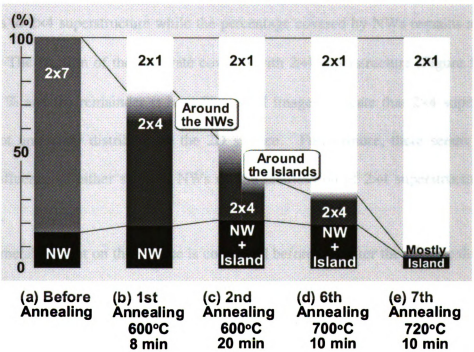

Figure 5.3 Annealing behavior of Dy grown on Si(001) at 0.58 ML. 3D structures of $DySi_2$ transit from large 3D islands by annealing. 2×7 superstructure dominates on the 2D surface after rapid deposition of Dy. After 1 min annealing at 600°C, 2×7 superstructure is replaced by 2×4 superstructure and bare Si. Less 2×4 structure appears with higher temperature annealing or longer annealing time.

min), 3rd (635°C 12 min), 4th (655°C 10 min), 5th (678°C 10 min), 6th (700°C 10 min), and 7th (720°C 10 min). STM images were taken after each annealing step. The large-scale STM images of changes in surface morphology (a)~(e) in Figure 5.4 correspond to the bar graphs labeled with the same letters in Figure 5.3. The measured areas were averaged over more than five images after each annealing step. The results of 3rd ~ 5th annealing are omitted for simplicity because the surface morphologies after 3rd ~ 5th annealing are very similar to that after 2nd annealing.

Elongated NWs with uniform width and 2×7 superstructure dominate on the surface after rapid deposition without post-annealing [Figure 5.3 (a)] as already shown in Figures 5.1 (a) and 5.2 (a). After 1st annealing, the substrate surface reconstruction completely changes to 2×4 superstructure while the percentage covered by NWs remains almost the same. The fraction of the substrate covered with 2×4 superstructure [Figure 5.3 (b)] is 66 ± 8 % and the remainder is bare Si. STM images indicate that 2×4 superstructure does not uniformly distribute on the 2D surface. Furthermore, there seems to be no clear influence of either steps or NWs on the distribution of 2×4 superstructure on the surface.

The metal content on the surface is conserved before and after the 1st annealing step at 600°C. The calculation below indicates that the increased quantity of Dy atoms in the NWs is equal to the decreased quantity of Dy atoms on the 2D surface. Firstly, the calculation for the metal content in NWs is performed. Dy metal density in the $DySi_2$ is ρ_{Dy} = 19.1 atoms/nm^3, where the lattice parameters of hexagonal $DySi_2$ structure are a = 0.3831 nm and c = 0.4121 nm [36]. If we assume that the minimum height NWs include one bulk $DySi_2$ unit cell high (= one Dy layer plus two silicon layers = 0.33 nm

high), 0.93 ML (= 19.1 atoms/nm^3 × 0.33 nm = 6.30×10^{14} atoms/cm^2) of Dy covers the whole surface as $DySi_2$ NWs. Because there is ~20% of second layer growth on top of NWs after annealing, the percentage difference of metal content in NWs before and after annealing is: Δ(NWs) = 18.5 % × 1.2 (after annealing) – 15.1 % (before annealing) = 7.1 %. Therefore, 0.066 ML (= 7.1% of 0.93 ML) of Dy atoms is expected to have moved from the 2D reconstructed surface to the NWs by annealing.

The second part is the calculation of the metal content on 2D surface. If we assume that there are five (three) Dy atoms per 2×7 (2×4) unit cell [72], the difference in metal content on the 2D surface before and after annealing is: Δ(2D) = 0.357 ML × 85 % (before annealing: 2×7) – 0.375 ML × 66 ± 8 % (after annealing: 2×4) = 0.055 ± 0.030 ML. Therefore, there are less Dy atoms on the 2D surface after annealing. This coverage range of 0.055 ± 0.030 ML for 2D surface also agrees with the change in coverage of 0.066 ML from the calculation for NWs.

After the 2nd annealing, 3D compact silicide islands start appearing, although NWs are still dominant on the surface [Figure 5.4 (c)]. This phenomenon supports the results reported by B.Z. Liu *et al.* [12] The longer side of small 3D islands tends to be oriented along the direction of NWs. More 2×4 superstructure can be seen around NWs than 3D islands [Figure 5.3 (c)]. The percentage of the 2D surface covered with 2×4 superstructure is 36 ± 13 % (21 ± 4 %) around NWs (3D islands). This result implies that 3D islands are a more favorable state than NWs since there are less Dy atoms around 3D islands than NWs. Additional annealings increase the number of 3D islands and the island size. At the same time, the number of NWs decreases and the surface reconstruction is gradually swept away. After the 7th annealing at 720°C, various sizes

of 3D islands are visible and very few NWs are observed on the surface [Figure 5.4 (e)]. There is no obvious metal induced reconstruction left on the surface, but surface defects are present on approximately 10 percent of the 2×1 bare Si(001) substrate. It is difficult to confirm the mass conservation of Dy in this limit since the 3D islands are very sparse and the size range of the 3D islands is very wide. Also, Transmission Electron Microscopy (TEM) study reveals that large 3D silicide islands extend underneath the plate of the surface [154], making it difficult to accurately calculate their volume from what is seen in the STM data.

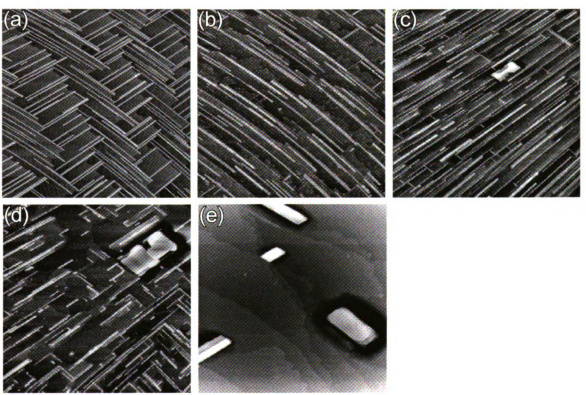

Figure 5.4 Transition from NWs to large 3D islands of $DySi_2$ by annealing. (a) 0.58 ML of Dy was deposited at 600°C, (b) 1st annealing at 600°C for 8 min, (c) 2nd annealing at 600°C for 20 min, (d) 6th annealing at 700°C for 10 min, and (e) 7th annealing at 720°C for 10 min. All image sizes are 400×400 nm^2.

5.1.2 LEEM experiments

Figure 5.5 shows (a) the LEED pattern, (b) a dark-field LEEM image, and (c) a bright-field LEEM image of 0.78 ML of Dy grown on Si(001) at ~600°C. Under these conditions, the surface should be covered in the 2×7 reconstruction plus NWs as in Figures 5.1 (a) and 5.4 (a). All three images were taken at RT after deposition. The

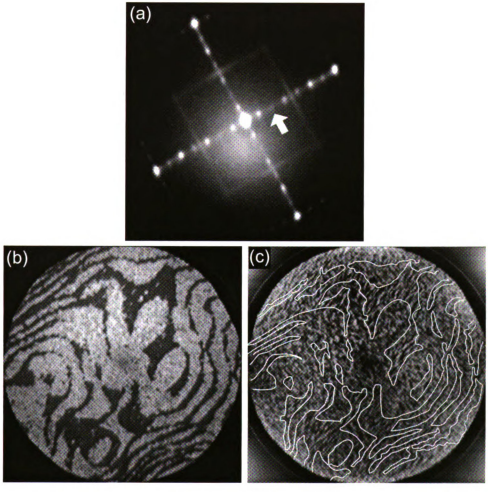

Figure 5.5 (a) The LEED pattern of Dy grown on Si(001) at ~600°C (0.78 ML). 1×7 phase and 1/2 order streaks are shown. The electron beam voltage is 60 V. (b) Dark-field LEEM image (2 eV) taken from 2/7 spot shown with the white arrow in (a). The field of view is 4 μm. (c) Bright-field LEEM image (9 eV) in the same area of (b) showing the stripe structure. Contours of terraces are drawn with white lines. The stripes are oriented at an angle of 90 degrees on each terrace, which correspond to the NWs.

electron beam voltage is 60 V in Figure 5.5 (a). The diffraction pattern with 7× periodicity and 1/2-order streaks are similar to typical LEED pattern observed from 2×7 reconstructed surface of Gd, Dy, or Ho grown on Si(001) at 600°C [72]. Figure 5.5 (b) shows the dark-field LEEM image (2 eV) taken from the 2/7-order diffraction spot denoted with the white arrow in Figure 5.5 (a). The field of view is 4 μm. A clear bright-dark contrast is observed on alternate terraces. Each terrace shows a cross-hatched texture, as well as a few small isolated islands. The spacing of the cross-hatching is about 50 nm, and it is oriented along $<1\bar{1}0>$ directions but it is not a direct image of the NW structures. Figure 5.5 (c) is a bright-field image (9 eV) in the same area of Figure 5.5 (b) showing the striped structure. The contours of terraces are drawn with white lines. There is a rough alteration in stripe direction across the terraces, which is consistent with NW related features, but and again, the apparent size and spacing are too large to be the NWs.

Figure 5.6 shows the sequence of LEEM images presenting the growth of Dy disilicide islands (0.78 ML) during annealing. Annealing duration time and the temperature are indicated on the lower left side, and imaging mode (BF: bright field, TBF: tilted bright field) and the incident electron energy are indicated on the lower right side of each image.

As already mentioned in Section 5.1.1, the 2×7 superstructure is replaced by a 2×4 superstructure after 1 min annealing. Also, for LEED pattern in Figure 5.5 (a), the position of 2/7-order diffraction spot is very close to that of 2×4-diffraction spot. Since the aperture used is not small enough to distinguish those two spots, 2/7-order and/or the 2×4-diffraction spot are used to form the dark-field image during annealing. The shape of the terraces in the dark-field image remains the same up to ~620°C. This clarifies

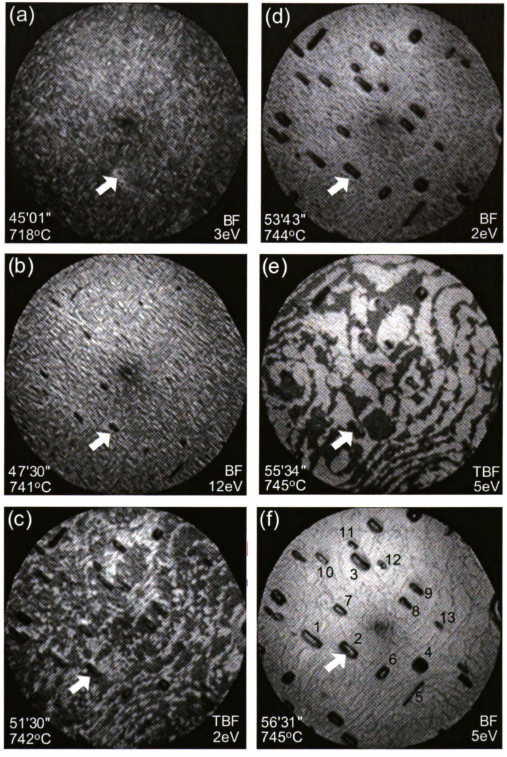

Figure 5.6 Sequence of LEEM images showing the growth of $DySi_2$ islands (0.78 ML). The field of view is 4 μm. The white arrows show the same island. Small grain structures start appearing at ~700°C and grow as islands. BF: Bright field, TBF: Tilted bright field.

that silicon atoms does not move on a macroscopic scale when the 2×7 to 2×4 phase transition occurs. The terrace contrast becomes weaker above ~700°C, although the terraces still have the original profile.

The annealing temperature was gradually increased from RT to ~750°C for 60 minutes. The relationship between annealing duration and temperature change above ~600°C is shown in Figure 5.7. In Figure 5.6, the white arrow points out the same island and its surrounding area in each image. Different islands labeled with numbers in Figure 5.6 (f) are classified as follows: (#1-5) large islands, (#6-10) medium islands, and (#11-13) small islands. The incident electron energies of 2~3 eV, 4.5 eV, and 11~12 eV give the best contrast for surface terrace in the dark-field image [Figure 5.5 (b)], step phase in the bright-field image [Figure 5.6 (f)], and stripe structures in the bright-field image [Figures 5.5 (c) and 5.6 (b)], respectively. Tilted bright field (TBF) image provides the information of both island growth and surface terrace morphology.

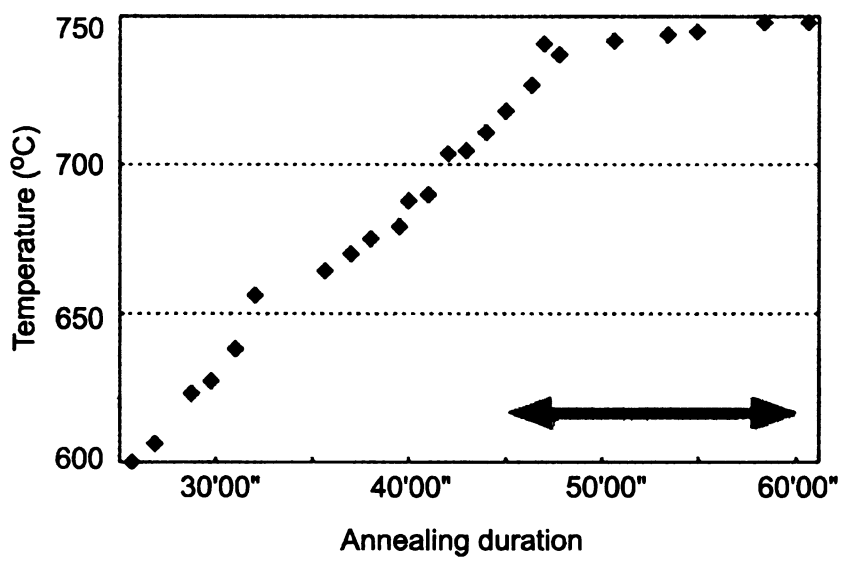

Figure 5.7 Annealing duration vs. temperature. Annealing temperature was gradually increased from RT (00'00") to 750°C. The black arrow shows the time range during which the islands are observed as shown in Figures 5.8 and 5.9.

The nucleation of small structures that eventually grow into islands starts at ~700°C [Figure 5.6 (a)]. However, the initial stage of the nucleation process cannot be seen because of the limited resolution, and small islands are hardly distinguishable from the darker contrast in the stripe structure. Islands become clearly visible 15 seconds after nucleation. In most cases, the shape of the islands is a rounded rectangle, but a few square (#4) and elongated (#5) shapes can be also found [Figure 5.6 (f)].

During annealing process, three types of island growth are observed as shown in Figure 5.8. Time evolution of the length and the width of three different islands [#4, 5, and 6 in Figure 5.6 (f)] are plotted. The length and the width of islands are marked with black squares and white triangles, respectively. Note that the vertical axes in Figure 5.8 (and Figure 5.9) show the length and the width of 3D islands including the area of surrounding trenches which are clearly visible in STM [Figure 5.4 (e)] but are not resolvable from the actual islands in the LEEM. Therefore, the actual island dimensions are slightly smaller than those shown in the graphs. However, it is clear enough to understand the growth behavior of islands since the surrounding Si depletion areas approximate the shape of islands.

The first type of island growth is square growth [Figure 5.8 (a)] in which the width and the length of the island increase at the same rate. The square island (#4) grows in this manner. The second type of growth is elongated growth [Figure 5.8 (b)] in which the length increases while the width remains constant. The elongated island (#5) is this case. The third type of growth is the most common growth, rectangular growth [Figure 5.8 (c)]. Both width and length increase uniformly but the growth rate of length is faster than that of width. Here, island #6 was illustrated by an example in Figure 5.8 (c) although the

other islands (#1-3 and #7-13) grow in the similar way. Except for the elongated island (#5), the island width and length grow uniformly in all the directions while maintaining the same aspect ratio. The aspect ratios of square (#4) and elongated (#5) islands are 1.2:1 and 7.3:1, respectively, while those of rectangular islands are in the range of 1.8:1 ~ 4.6:1.

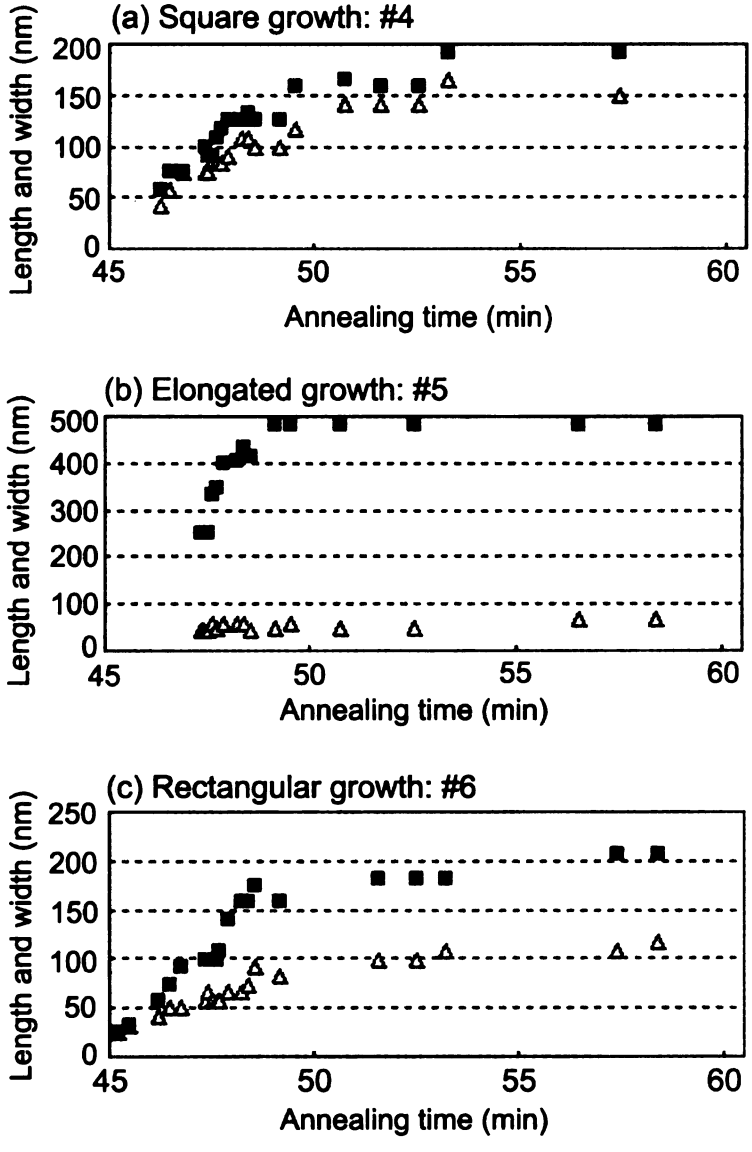

Figure 5.8 Time evolution of the length and the width of 3D islands and the surrounding Si depletion areas in different growth types during annealing.

Figure 5.9 shows the change in the size of the islands by annealing. Black, gray, and white marks indicate large, medium, and small islands, respectively. Numbers from 1 to 13 correspond to the islands labeled with the same numbers in Figure 5.6 (f). The labels (a)~(f) indicate times at which the LEEM images in Figure 5.6 were captured. The island growth starts and ceases in the same time regardless of the island size. This implies that the growth rate of larger islands is faster than that of smaller islands. After 5 minutes of island growth, the island size remains constant up to ~750°C. In general, the island sizes do not change up to ~760°C and Dy metals start leaving the surface by annealing at above ~780°C according to the experiments under similar conditions.

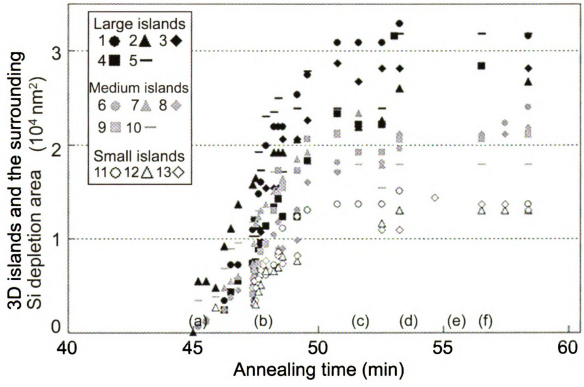

Figure 5.9 Change in the island size by annealing (0.78 ML of Dy). Black, gray, and white marks indicated large, medium, and small islands, respectively. The islands numbered from 1 to 13 correspond to the islands with the same numbers in Figure 5.6 (f). The labels (a)~(f) are marked for the time at which the LEEM images in Figure 5.6 were taken.

Silicon terraces start breaking up during the island growth [Figure 5.6 (c)]. After the island growth ceases, terraces start rearranging themselves to form regular Si(001) surface [Figure 5.6 (e)] with 2×1 periodicity of the LEED pattern. TBF images of Figures 5.6 (c) and 5.6 (e) have an opposite contrast due to the different incident electron energy and the different beam tilt in the azimuthal angle. As the traces of streaked structure shown in Figure 5.6 (d), small dots are left on the terraces with weak contrast. This might be a reflection of surface defect areas that are generally observed on STM images as explained in Section 5.1.1.

5.2 Discussion

A $DySi_2$ NW has a hexagonal AlB_2 structure. The formation of $DySi_2$ NWs arises from the anisotropic lattice mismatch between $DySi_2$ and the Si(001) substrate. The orientation relationships of hexagonal $DySi_2$ on Si(001) are determined to be [5, 9, 12]:

$DySi_2(1\bar{1}00)$ // Si(001), $DySi_2[0001]$ // $Si[1\bar{1}0]$, and $DySi_2[11\bar{2}0]$ // Si[110].

Comparing the lattice mismatch in *a* and *c* directions of the hexagonal structure with Si(001) 1×1 unit cell, the lattice mismatch in the *a* direction is very small (-0.23 %). On the other hand, the lattice mismatch in the *c* direction is large (+7.32 %). Because of those anisotropic lattice-mismatch strains, hexagonal $DySi_2$ is favored to grow in the *a* direction than the *c* direction. Therefore, *a* and *c* directions of hexagonal structure correspond to a length and width of NW, respectively.

When NWs are grown under conditions where the substrate is at least partially covered in the 2×4 phase, then the widths of NWs are relatively broadly distributed between about $2a_{Si}$ and $16a_{Si}$. The limit that one would expect for coherent growth is about $14a_{Si}$,

given the lattice mismatch in the direction of the NW width. However, as shown in this work, if the substrate is dominated by the 2×7 phase, most of the NW widths are $7a_{Si}$ which suggests that the presence of the 2×7 surface reconstruction can affect how the NWs nucleate and grown. The stronger influence of the 2×7 phase may be due to two factors. Firstly, even in the case of the 2×4 surface, most NWs are wider than 3 or $4a_{Si}$ which suggests that NWs prefer to grow wider than the width of the 2×4 unit cell. Secondly, it is clear in images of surfaces with a mixture of 2×4 and 2×7 that the 2×7 phase is much more highly ordered. As can be seen in Figure 5.1 (a), the bright rows of the 2×7 phase are ordered over a similar length scale as adjacent NWs. Annealing at 600°C [Figure 5.1 (b)] converts some of the 2×7 into 2×4, and at the same time, NWs appear to have moved and reconfigured since they are much more likely to be seen in bundles, and they are much more likely to show second layer growth. Figure 5.1 illustrates that the NWs are a metastable phase, and that the structural order and uniformity of the NWs are a very sensitive function of growth conditions.

Islands grow in the temperature regime where conversion from NWs to 3D islands is seen in the STM images shown in Figure 5.4. Specifically, significant conversion of NW to 3D islands is not seen even after extended annealing at 600°C [Figure 5.4 (c)], whereas the annealing above 700°C causes the significant conversion of surface morphology [Figure 5.4 (d)]: transition from NWs to 3D islands.

When the NW width reaches a certain critical width during annealing, where the maximum width mismatch between $DySi_2$ and Si(001) substrate reaches $1a_{Si}$, a dislocation is generated in order to release the misfit strain. Cross-sectional TEM observation shows two types of misfit dislocations at the interface between 3D islands

and Si substrate [154]. In a Type I dislocation, there are several tilted misfit dislocations along the interface between 3D islands and Si substrate. In a Type II dislocation, the whole island is tilted at a small angle with respect to the Si substrate, but there is no partial misfit dislocation. When the Type I dislocation occurs, the $DySi_2$ can readily grow in both directions resulting in the formation of rectangular islands.

For the elongated island [island #5 in Figure 5.6 (f)], there is a larger misfit strain along the width direction, since the width of an elongated island is narrower than that of rectangular islands. If the misfit dislocation along the width direction is suppressed during annealing for some reason, the misfit strain relaxation occurs in the length direction and the island length increases. The formation of the elongated island might be related to a Type II dislocation which has a tilted crystal structure. After all, it is possible that 3D islands can be formed in different growth modes.

$DySi_2$ NWs grow in the Stranski-Krastanov (SK) mode. As 3D islands start growing, the growth mode changes from SK mode to Volmer-Weber (VW) mode [Figure 5.3]. When the island nucleation occurs, Dy atoms are desorbed from the 2D surface and attach along the island edges resulting the linear increase of the island area. The island-size distribution is broadened. Once Dy atoms attach to the 3D islands, they preferentially remain on the island regardless of the island size. It seems that the attachment probability of Dy atoms to 3D islands is equal, so that larger islands can attract more atoms because of longer circumferences. Therefore, the island growth rate is size-dependent: Larger and smaller islands grow with faster and slower growth rates, respectively [Figure 5.9]. The relative size differences of large and small islands do not change during the island growth.

Even though the general behavior of islands in all size ranges is similar, Figure 5.8 clearly shows that islands can exhibit both a variety of morphologies and associated growth behaviors. The most common island is rectangular, and although there is a distribution of aspect ratios seen, each individual island is seen to maintain the same aspect ratio during growth. Square growth is a variation of this behavior. Finally, a few islands show elongated growth, where the width of the island is fixed as the island lengthens. This type of 1D growth has been seen in the case of other silicides, including $ErSi_2$, and it has been related to various theories. However, the diversity in growth behaviors and island morphologies seen in the LEEM data in Figure 5.6 make it clear that at least in this system, one cannot make any generalizations about growth in this system. Furthermore, it is dangerous to make a case for growth behavior base on just one type of island.

For the RE silicides, it is possible that some of these different behaviors could be related to the presence of different silicide structures. $DySi_2$ can crystallize into hexagonal, orthorhombic and tetragonal phases, all of which have different lattice constants. It is tempting on geometrical grounds to associate square, rectangular, and elongated growths with the tetragonal, orthorhombic, and hexagonal phases, respectively. In fact, TEM studies of 3D islands grown in this system have shown that islands can be either hexagonal or orthorhombic / tetragonal, at least at a growth temperature of 600°C. Correlation of island morphology and silicide crystal structure requires further plan view TEM work. The LEEM data relates island morphology to growth behavior.

All NWs are gone at 720°C, which is roughly the temperature at which the 3D islands stop growing in the LEEM measurement. Essentially, growth stops at the point where

there is no longer a source of Dy available, from either the substrate reconstruction, or the NWs.

After island growth stops, there is no further evolution of the islands, even after extended annealing at 750°C. No ripening or coarsening is seen. This is consistent with the behavior reported for Er silicide islands on Si(001) annealed at 800°C [76].

One other interesting point is that the Si steps are observed to wander after island growth stops, whereas they are largely static during the conversion of NW to islands. Given the strong interaction between NW and single height step configuration seen in the STM images, it is possible that the substrate steps are pinned in place by a few remaining NW, until the conversion to 3D silicide islands is complete.

5.3 Conclusions

After rapid Dy deposition, almost all 2D surface is covered with 2×7 superstructure, and NWs have uniform width with $7a_{Si}$ which is 7 times as wide as the lattice constant of silicon. Surface reconstruction phase immediately changes from 2×7 to 2×4 superstructure by annealing, while the percentage of NWs remains almost the same. Therefore, this fact insists that 2×7 superstructure is the metastable state. The metal content on the surface also conserves before and after annealing at 600°C. Annealing at 700°C increases the number of 3D islands and the average island size. At the same time, the number of NWs decreases and surface reconstruction is swept away. This fact insists that 3D islands are the stable state whereas NWs are a metastable state at 700°C.

When the sample is heated, the silicon terraces have the same contours up to ~620°C. Silicon terraces start breaking up and the terrace contrast weakens at ~700°C as the

nucleation of islands starts. The island growth starts and ceases in the same time regardless of the island size. Larger 3D islands grow at a faster growth rate than smaller islands.

Chapter 6 Transport Measurements

Deposition of a RE metal on the Si(001) surface at an elevated temperature results in the formation of silicide islands and NWs coexisting with a reconstructed substrate surface. Although it is important to understand the electrical properties of RE silicide NWs and islands in air for practical applications, no one so far has done the transport measurements of ultra high vacuum (UHV)-prepared samples in air.

We describe our approach for making transport measurements on nanometer scale thickness films grown on atomically clean silicon in UHV. A combination of *ex-situ* Ti silicide and *in-situ* Au deposition is used for contacts. Samples are passivated with amorphous germanium (Ge) before being removed from UHV for transport measurements at 4.2 K. The transport properties are correlated with film morphology as observed by STM.

In this chapter, we will present the results of ongoing measurements on macroscopic networks of the Dy silicide islands.

6.1 Sample preparation

The procedure needs several steps for the sample preparation as shown in Figure 6.1. After a sample is chemically cleaned (Step 1), Si and Ta (or Ti) depositions are carried out in a dc-magnetron triode sputtering system with a base pressure of 3×10^{-8} Torr (Step 2). The sputtering Ar pressure is 2×10^{-3} Torr. Ar and Ta (or Ti) purities are 99.999 % and 99.99 %, respectively. The sample with pre-deposited Ta (or Ti) contacts is then transferred into the UHV chamber and flashed briefly at 1175°C to remove surface oxide (Step 4). At the same time, Ta (or Ti) forms silicides which serve as contacts for

transport measurements (Step 5). After a RE silicide thin film is made by the same experimental procedure as Section 2.1 (Step 6), gold (Au) is deposited through a shadow mask on top of $TaSi_2$ (or $TiSi_2$) (Step 7). Since Au partially covers the RE silicide thin film, there is a direct connection between Au contacts and the RE silicide thin film. In the end, the sample is passivated with amorphous Ge at RT to avoid surface oxidation (Step 8), and then removed from UHV chamber for transport measurements.

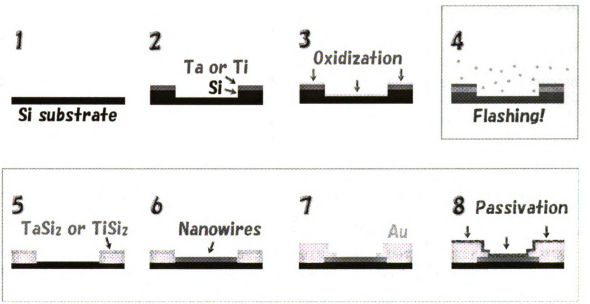

Figure 6.1 Sample preparation procedure for transport measurements. Si and Ta (or Ti) depositions are done in the high vacuum chamber (Step 1 and 2). Sample flashing, deposition of RE metals, Au contacts, and amorphous Ge are performed in the UHV chamber (Step 4~8).

6.1.1 Pre-deposited Ta (or Ti) silicide contacts

Refractory metal disilicides have been of special interest due to their temperature stability and relatively low resistivity [155-165]. $TaSi_2$ and $TiSi_2$ are the candidates for pre-growth deposited contacts for transport measurements, since these silicides can

survive the high temperature flash necessary to clean the Si(001) surface [166]. The contact resistances are in the range of 6.8~52 Ω for $TaSi_2$ and 5~15 Ω for $TiSi_2$ at 4.2 K [155].

$TaSi_2$ is a hexagonal structure (C40) with a *c/a* ratio of about 1.38 [155]. The sheet resistance of the $TaSi_2$ thin film decreases with an increase in film thickness and annealing temperature [156, 157]. On the other hand, $TiSi_2$ exists in two phases: a metastable C49 base-centered orthorhombic phase that is formed at lower temperature and the stable face-centered orthorhombic C54 phase formed at higher temperature [158]. The C54 phase is more desirable for device applications because the C54 phase has lower resistivity than the C49 phase. But the resistivity of $TiSi_2$ increases due to the failure of the C49 to C54 phase conversion as the lateral dimension of $TiSi_2$ shrinks to less than 1 μm [159]. However, the type of $TiSi_2$ phases will not affect our macroscopic measurements since our contact dimension and thickness are not in the submicron range.

Si diffuses into Ti layers from 500°C and then $TiSi_2$ is formed at 600°C. $TaSi_2$ is also formed from 600°C [160], but the crystallization of $TaSi_2$ occurs mainly between 800°C and 900°C [157]. The initial attempts at making Ta silicide contacts involved depositing just Ta onto the substrate, and then annealing in UHV. As shown in Figure 6.2, when the sample with a pre-deposited Ta is annealed, a deep trench is created on the boundary between $TaSi_2$ and Si surface because Si around Ta is consumed to form $TaSi_2$. The same phenomenon can be seen for $TiSi_2$. Since these trenches might interfere with connections to a RE thin film to $TaSi_2$ contacts, the deposition of Si with Ta is necessary beforehand as shown in Figure 6.1. The ratio of metal to deposited Si thickness is 1:2.23 (1:2.27) for Ta (Ti) in order for the stoichiometry of the deposited material to be

MSi_2. When this is done, the trenches around the contacts are largely gone, and also the rough boundary region around the contacts is narrower. Figures 6.3 (a) and 6.3 (b) show the surface morphology of $TaSi_2$ and $TiSi_2$ films, respectively. Although the films do not appear smooth, they are continuous.

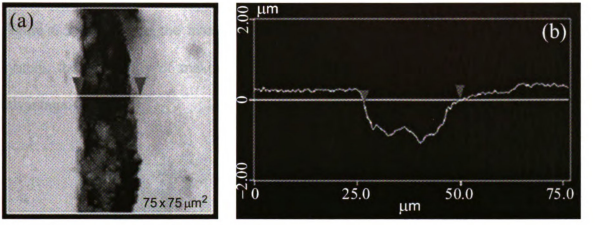

Figure 6.2 (a) Atomic Force Microscopy (AFM) image of the boundary between $TaSi_2$ and Si substrate after annealing 100 nm thick Ta on silicon. (b) Cross-sectional profile traced along a white line in (a) showing a deep trench. (Width = 23 μm, depth = 800 nm)

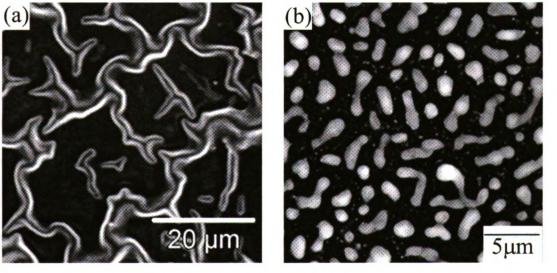

Figure 6.3 Scanning Electron Microscopy (SEM) images of (a) $TaSi_2$ and (b) $TiSi_2$ films. For (a), 200 nm of Si + 100 nm of Ta films are annealed after deposition. For (b), 100 nm of Si + 50 nm of Ti films are annealed after deposition.

For the deposition of Si and Ta (or Ti) in Step 2 in Figure 6.1, sputtering masks are used as shown in Figure 6.4 (a). Three samples are fitted on one mask. A rectangle in Figure 6.4 (a) indicates the position of the sample sitting in the middle of the sputtering mask. Other two samples can be put on the top and bottom of the middle sample. After Si and Ta (or Ti) deposition, four contacts are made on each sample as shown in Figure 6.5 (a). Since the maximum of 24 samples can be loaded on the sputtering system, the possibility of making many pre-deposited contacts at once offers a great advantage.

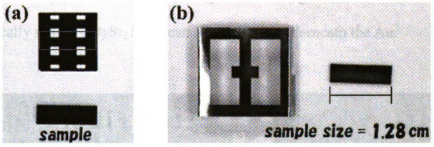

Figure 6.4 (a) Sputtering mask for Ta (or Ti) deposition. (b) Shadow mask for Au deposition.

6.1.2 *In-situ* Au contacts

After the RE silicide growth, Au contacts are deposited at RT by covering a sample with the middle of a shadow mask as shown in Figure 6.4 (b) (Step 7 in Figure 6.1). About 50 ML (~6 nm) of Au is deposited on top of $TaSi_2$ (or $TiSi_2$) contacts [Figure 6.5 (a)]. The Au thin-film contacts are composed of many small islands which are connected to each other [Figure 6.5 (c)]. Figure 6.5 (b) shows a magnified view of the edge of the Ti silicide contact overlaid with Au. As mentioned previously, the codeposition of Si and Ti before annealing eliminates any trenching around the silicide. At the same time, it is clear that the edges of the Au contact are not sharp. This is

because of a combination of the distance between the shadow mask and the sample (which is about 0.5 mm), the distance between the shadow mask and Au evaporation source (about 5 mm), the dimension of the shadow mask (2.5 mm), and the finite size of the Au evaporation source (about 2 mm diameter). Given the geometry of the source relative to the mask and the sample, one expects that the boundary of the Au deposition would be spread over about 0.1 mm as shown in Figure 6.6.

Figures 6.7 (a)~(c) show the STM images of the boundaries on the Au contact. The distance between the areas shown in these images is about 1 μm. The density of Au increases from image (a) to (c), meaning that the edge of the Au boundary is not microscopically sharp. $DySi_2$ NWs can be also seen underneath the Au.

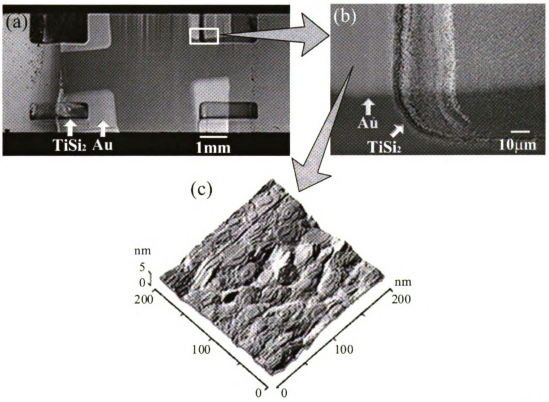

Figure 6.5 (a), (b) Optical microscope images of Au contacts covering beneath $TiSi_2$ contacts. (b) Close-up image of the area marked with a white rectangle in (a). (c) 3D STM image of the Au contact. The formation of many small Au islands is observed.

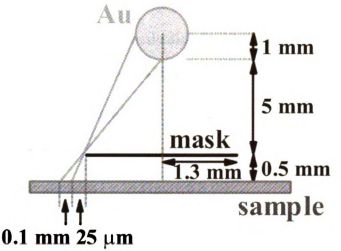

Figure 6.6 Schematic diagram of Au evaporation with a shadow mask.

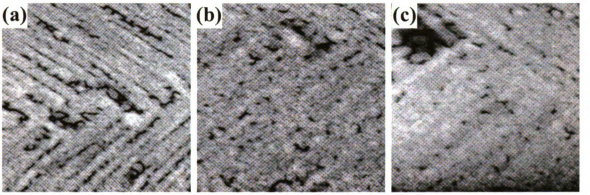

Figure 6.7 STM images of the Au boundaries (200×200 nm^2). The density of Au increases from (a) to (c). $DySi_2$ NWs can be seen underneath of Au.

6.1.3 Amorphous Ge passivation

Since RE elements and RE silicides are very reactive with oxygen, it is important to protect the sample surface from oxidation in air. The materials used for surface passivation should meet the following two conditions. Firstly, it must not affect the conductance of the sample. Hence, it should be nonconductive at 4.2 K at which transport measurements are performed. Secondly, it should not be reactive with RE

silicide and Si at RT so that surface morphology underneath does not change. Although we first used hydrogen for the surface passivation for historical reasons (see Appendix A), Ge seems to work better in terms of more reliable transport measurements.

Figures 6.8 (a) and 6.8 (b) show the STM images of 'before' and 'after' 5 ML of Ge deposition on $DySi_2$ NWs and interconnected 3D islands, respectively. NWs still survive underneath the amorphous Ge in Figure 6.8 (b).

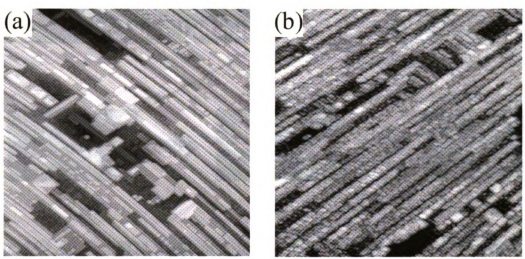

Figure 6.8 (a) Before Ge deposition: $DySi_2$ NWs with interconnected 3D islands. (180×180 nm^2) Coverage is unknown. (b) After 5 ML of Ge deposition on top of NWs. (200×200 nm^2)

6.2 Transport measurements: Results and discussion

All transport measurements are done at liquid helium temperature (4.2 K) as shown in Figure 6.9 (b). Four-terminal surface resistances are measured by a Keithley digital multimeter. Note that four-terminal measurements can exclude the contact resistance and provide only sample resistance (see Appendix C). From the two-terminal measurements, contact resistances are a few Ω at RT and >1 MΩ at 4.2 K.

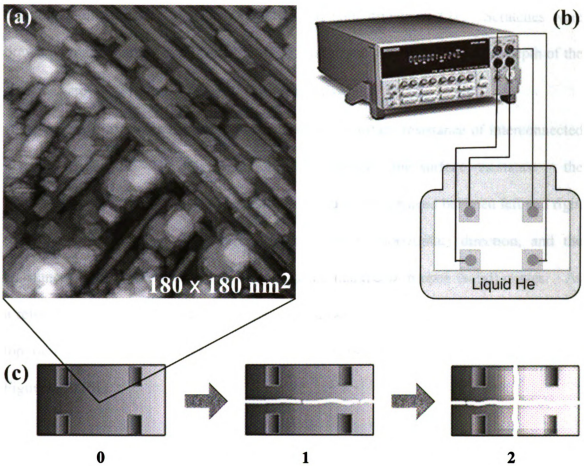

Figure 6.9 (a) The STM image of 3 ML of interconnected Dy silicide islands. (b) Experimental setup for transport measurements. Surface resistances were measured at liquid helium temperature (4.2 K). (c) In order to measure the change in surface resistance of the sample (a), the sample was scratched in the horizontal and vertical directions. The numbers labeled on the bottom 0, 1, and 2 indicate 'before scratch', 'scratched in the horizontal direction', and 'scratched in the both directions', respectively.

In the first part of the experiments, changes in surface resistance due to sample scratching was investigated. The surface topography of the sample with 3 ML of Dy is shown in Figure 6.9 (a). The surface is covered with interconnected Dy silicide islands. The surface resistances were measured in three steps: without scratch (Step 0), with a scratch in the horizontal direction (Step 1), and both directions (Step 2). The numbers labeled in Figures 6.9 (c) and 6.10, indicate 'before scratch (0)', 'scratched in the

horizontal direction (1)', and 'scratched in the both directions (2)'. Scratches were drawn with a diamond tipped pencil. AFM images show that the width and depth of the scratches are ~6±2 μm and ~200±100 nm, respectively.

Figure 6.10 (a) shows the change in four-terminal surface resistance of interconnected Dy silicide islands. The left (right) diagram represents the surface resistance in the vertical (horizontal) direction. The resistance values are averaged between left and right (top and bottom) sides of contacts for the vertical (horizontal) direction, and the resistances in three steps of sample scratching are marked with open (solid) circles. As a reference, the surface resistance of clean Si surface is indicated with a dashed line on top of each diagram. Corresponding current flows are schematically diagramed in Figure 6.10 (b).

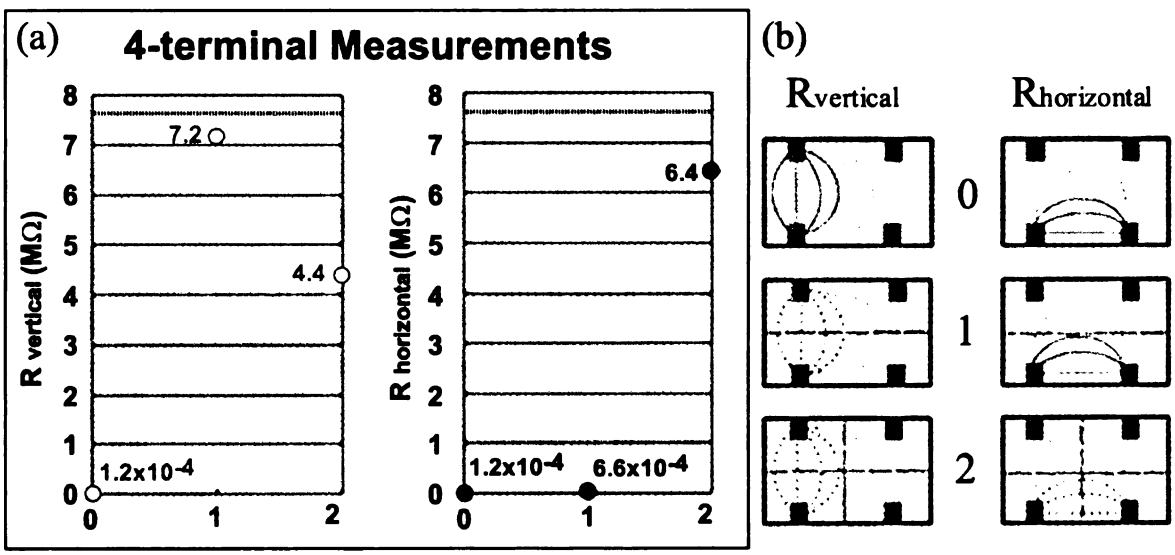

Figure 6.10 (a) Change in 4-terminal surface resistance of interconnected Dy silicide islands due to the sample scratching. A diagram shows the resistances in the vertical (open circles) and horizontal (solid circles) directions, respectively. Dashed lines on top are the surface resistance of clean Si surface. (b) Schematic diagrams of each step of sample scratching and corresponding current flow.

Before the sample scratching (Step 0), surface resistances in both vertical and horizontal directions are ~1.2×10^2 Ω. For this particular sample, the distance between two contacts in the vertical (horizontal) direction is 1.45 mm (1.75 mm). In case of the surface resistance in the vertical direction (open circles), the resistance increases dramatically to 7.2 MΩ after scratching in the horizontal direction (Step 1), because there is a large barrier between contacts and the current cannot pass though easily [$R_{vertical}$ '1' in Figure 6.10 (b)]. After scratching in the vertical direction (Step 2), the resistance drops, because the vertical barrier tends to confine the flowing current to the left side [$R_{vertical}$ '2' in Figure 6.10 (b)] thereby decreasing the voltage drop measured across the right hand side contacts.

In the similar way, the change in the surface resistance in the horizontal direction can be explained. After scratching in the horizontal direction (Step 1), the resistance slightly increases, but the resistance value remains the same order of magnitude as that before scratching. After scratching in the vertical direction (Step 2), the resistance jumps up to 6.4 MΩ due to the barrier between the contacts. It should be also mentioned that the surface resistance values of interconnected Dy silicide islands are smaller than that of clean Si surface which is drawn by dashed lines in Figure 6.10 even after scratching the sample in both directions. This is a reasonable result because there is small electrical contribution to the surface conductivity from Dy metals on Si substrate, although there are deep boundaries in the middle of the sample. In the conclusion for the first part of our experiments, the destruction of interconnected Dy silicide islands increases the surface resistance.

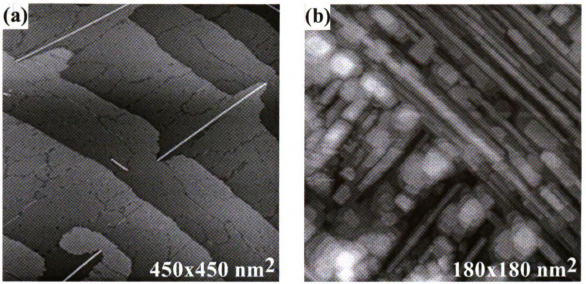

Figure 6.11 STM images of (a) $DySi_2$ NWs at 0.22 ML and (b) interconnected Dy silicide islands at 3 ML.

The second part of our transport measurements is the comparison of surface conductivity at different metal coverages. Figure 6.11 shows the STM images of (a) $DySi_2$ NWs (450×450 nm^2) and (b) interconnected Dy silicide islands (180×180 nm^2). A few NWs are seen with 2×4 reconstructed surface at 0.22 ML [Figure 6.11 (a)], while the varying shape of 3D islands are connected and bare Si is not visible on the surface at 3 ML (≈1 nm) [Figure 6.11 (b)].

Figure 6.12 shows Dy and Ho film conductivity at 4.2 K vs. metal coverages. Solid (open) circles show the surface conductivity of Dy (Ho) on Si(001). The conductivity of Dy thick film with ~180 ML (60 nm) is added as a reference [68]. The values of conductivity are indicated in Table 6.1. A 3 ML (≈1 nm) thick film of interconnected $DySi_2$ islands shows surface conductivity at 4.2 K similar to the reported bulk silicide value. A sample with sparse and disconnected NWs (0.16 ML) shows lower surface conductivity than the 3 ML film but higher than that of the clean Si surface, because the

2D surface is reconstructed with Dy metal. The conductivity of a sample with a $DySi_2$ NW network (0.87 ML) is lower than that of the sample at lower coverage. One possible explanation for lower surface conductivity on the high-coverage sample is the contact type: instead of pre-deposited Ti and *in-situ* Au contacts, *ex-situ* Al contacts were used (see sample #12 on Table 6.2). For surface conductivities of Ho on Si(001) with *ex-situ* Al contacts, a sample with a $HoSi_2$ NW network shows higher conductivity than that with 2×4 reconstructed surface. Overall, the surface conductivity rises sharply somewhere in the coverage range of 1~3 ML.

Many variations in sample preparation were made to improve the reproducibility: changing the choice of contact materials, the thickness of the contacts, and sample cleaning procedures. The methods of sample preparation and the results of transport measurements of each sample are summarized in Table 6.2. The samples from which at least some resistance values could be obtained at 4.2 K, regardless of the adequacy of the values, are gray shaded on the background of the leftmost column. There is no consistency among the methods of sample preparation and the results of measurements. Although both two- and four-terminal surface resistances are all measurable at RT, low-temperature measurements lose the stability due to the background noise.

Unfortunately, the reliability of this experiments were not achieved from three-year efforts. Besides instability of low-temperature measurements, the limited amount of metal source and the multiple failures of the *in-situ* Au evaporator (Section 6.2.2) made the measurements very difficult. This work is supported by NSF ECS-0303801.

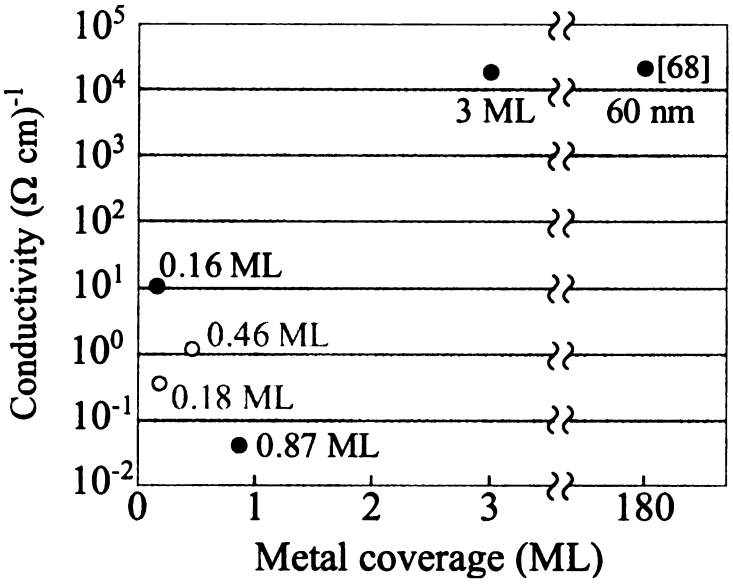

Figure 6.12 Dy and Ho film conductivity at 4.2 K vs. metal coverages. Solid (open) circles show the surface conductivity of Dy (Ho) on Si(001).

At 4.2 K	Metal layer coverage (ML)	Surface topography	Conductivity $(\Omega\ cm)^{-1}$	Sample # on Table 6.2
Dy	0.16	2×4	1.0×10^{1}	# 20
Dy	0.87	NW networks	3.9×10^{-2}	# 12
Dy	3	Interconnected islands	1.9×10^{4}	# 16
Dy	180 (60 nm)	Thin film	2.9×10^{4}	Ref [68]
Ho	0.18	2×4	3.7×10^{-1}	# 9
Ho	0.46	NW networks	1.3	# 6

Table 6.1 Dy and Ho film conductivity at 4.2 K vs. metal coverages. All the values correspond to those in Figure 6.12. There are no values for the conductivity of bulk Ho silicide in the literature, but the conductivity of the RE silicides lie in the range 4.5×10^{3} to 6.7×10^{5} $(\Omega\cdot cm)^{-1}$ at 4.2 K as in Table 1.4.

Table 6.2 Summary of transport samples measured. Data for the shaded samples are collected in Figure 6.12 and Table 6.1.

	Substrate type (ρ at RT)	Contact type	Surface topography	Measurements at 4.2 K
1, 2	*p*	Al	#1 blank, #2 flashed in UHV chamber	unstable
3	*n* (0.02 Ω·cm)		Ho (0.59 ML) sparse NWs and islands	—
4	*n* (2.76 Ω·cm)		Ho (0.58 ML) NW networks	
5	*n* (0.02 Ω·cm)		Ho (0.56 ML) unconnected NWs	—
6	*p*	*Ex-situ* Al (200 nm) annealed at 450°C for 35 min	Ho (0.46 ML) NW networks NW thickness ≡ 0.33 nm	ρ_{2V} = 0.80 Ω·cm ρ_{10V} = 0.25 Ω·cm
7	*p*	*Ex-situ* Al (200 nm) annealed at 450°C for 35 min	Ho (0.09 ML) 2×4, No NW	unstable
8	*n* (0.02 Ω·cm)	*Ex-situ* Al (200 nm) annealed at 450°C for 35 min	Dy (0.47 ML) unknown (Conductivity comes from the substrate.)	$\rho_{Si\ (2V)}$ = 3.5×10^{-3} Ω·cm
9	*p*	*Ex-situ* Al (138 nm) annealed at 450°C for 20 min	Ho (0.18 ML) 2×4 Thickness of 2×4 ≡ 0.11 nm	ρ_{2V} = 2.7 Ω·cm ρ_{10V} = 1.6 Ω·cm
10	*p*	*In-situ* Ag contacts (But Ag is peeled off easily.)	Ho (0.33 ML) a few NWs + 2×4	unstable
11	*p*	*Ex-situ* Al (250 nm) annealed at 450°C for 30 min	Ho (0.27 ML) 2×4	unstable
12	*p*	Al (245 nm) annealed at 450°C for 30 min	Dy (0.87 ML) NWs + 2×4 NW thickness ≡ 0.33 nm	ρ_{2V} = 26 Ω·cm ρ_{10V} = 16 Ω·cm
13	*p*	Al (180 nm) annealed at 450°C for 24 min	Dy (0.36 ML) unconnected NWs	R_{2t} = 10^9 Ω
14	*p*	Pre-deposited $TaSi_2$ (150 nm Si + 75 nm Ta at RT)	Dy (0.63 ML) NWs	unstable
15	*p*	Pre-deposited $TaSi_2$ (100 nm Si + 50 nm Ta at RT)	Dy (0.54 ML) 3D islsnds	unstable

$\rho_{2V\ (10V)}$: surface resistivity with applied voltage of 2 V (10 V); $R_{2t\ (4t)}$: 2- and 4-terminal resistances.

The resistivity of *p*-type substrate is 2.58 [Ω·cm] unless mentioned.

Table 6.2 (cont'd)

	Substrate type	Contact type	Surface topography	Measurements at 4.2 K
16	*p*	Pre-deposited $TiSi_2$ (170 nm Si + 75 nm Ti at –6°C) + *in-situ* Au (<90 ML)	Dy (3 ML ?) interconnected islands + Ge (5.6 ML) Layer thickness ≡ 1 nm	R_{4t} = 118 Ω ρ = 54 μΩ·cm
17	*p*	Pre-deposited $TiSi_2$ (170 nm Si + 75 nm Ti at –6°C) + *in-situ* Au (50 ML)	blank	R_{4t} = 7.65 MΩ ρ = 1.92 MΩ·cm
18	*p*	Pre-deposited $TiSi_2$ (170 nm Si + 75 nm Ti at –26°C) + *in-situ* Au (42~67 ML)	Ge (6.2 ML)	unstable
19	*p*	Pre-deposited $TiSi_2$ (114 nm Si + 50 nm Ti at –26°C) + *in-situ* Au (42~71 ML)	Dy (0.2 ML) + Ge (5.6 ML)	infinity
20	*p*	Pre-deposited $TiSi_2$ (170 nm Si + 75 nm Ti at –26°C) + *in-situ* Au (55 ML)	Dy (0.16 ML) 2×4 + Ge (4.5 ML) Thickness of 2×4 ≡ 0.11 nm	R_{4t} = 1.6~2.3 MΩ ρ = 9.6×10^{-2} Ω·cm
21	*p*	Pre-deposited $TiSi_2$ (170 nm Si + 75 nm Ti at 400°C) + *in-situ* Au (30~50 ML)	Dy (? ML) NW networks + Ge (4.5 ML)	unstable
22	*p*	Pre-deposited $TiSi_2$ (170 nm Si + 75 nm Ti at 40°C) + *in-situ* Au (30~50 ML)	Ge (4.8 ML)	R_{4t} = 16~200 MΩ ρ = 18 MΩ·cm
23	*p*	Pre-deposited $TiSi_2$ (170 nm Si + 75 nm Ti at 40°C) + *in-situ* Au (? ML)	Ge (4.5 ML)	infinity
24	*p*	Pre-deposited $TiSi_2$ (170 nm Si + 75 nm Ti at 40°C) + *in-situ* Au (11.4 ML)+ *ex-situ* Au (75+200 nm)	Dy (2.2 ML) + Ge (5.0 ML)	—
25	*n* (2.76 Ω·cm)	Pre-deposited $TiSi_2$ (170 nm Si + 75 nm Ti at 40°C) + *ex-situ* Ti (2 nm) and Au (200 nm)	Dy (~1 ML) NW networks	infinity

Chapter 7 Future work

In this chapter, suggestions for future work as a continuation of this thesis will be described: growth kinetics of RE silicide NWs and 3D islands, reproducibility of electrical contacts for transport measurements, single NW measurements, and temperature dependence and magnetic-field dependence of magnetic, structural and transport properties.

7.1 Further work on growth kinetics

In Chapter 5, we reported the LEEM observation of the evolution of Dy silicide islands during annealing. Our original purpose was to investigate the growth kinetics of RE silicide NWs such as NW nucleation, size and shape evolution, and Si step motion. Unfortunately, the width of RE silicide NWs (the width of single NW is typically < 5 nm) was below the lateral resolution limit of IBM Type I LEEM. The investigation of growth dynamics of RE silicide NWs, therefore, requires high-resolution LEEM/PEEM, or other alternative real-time surface analysis methods.

Recently, a few studies of the growth evolution of elongated Er silicide islands and Ti silicide NWs have been done by photoemission electron microscope (PEEM) or LEEM [76, 167, 168]. Since their dimensions are about 50 nm wide and several μm long, which is one order of magnitude larger than those of RE silicide NWs, they are resolvable in LEEM/PEEM.

Moreover, it is important to interpret a correlation of the growth behavior of the width and length (lateral directions) and the height (vertical direction) of NWs and 3D islands so that the surface diffusion mechanism, surface stress and strain relaxation can be better

understood. Combining these results with TEM data would provide stronger support, since TEM data offers information about the crystal structure (hexagonal, tetragonal, or orthorhombic structure) of the 3D islands and about the interface defects between the 3D islands and the Si substrate [154].

7.2 Reliability and reproducibility of electrical contacts for transport measurements

Normally, Si substrates with a resistivity of ρ ~2.5 Ω·cm at RT are used for our transport measurements so that the substrates do not contribute to the sample resistance in measurements at 4.2 K [169]. When the resistance of a highly-doped Si substrate which has low resistivity at 4.2 K (ρ ~10^{-2} Ω·cm at RT) was measured, resistance values were very stable and did not fluctuate during the measurements. Therefore, one can assume that the Si substrate and contacts, and the contacts and leads are well contacted.

However, the reproducibility of our measurements on RE silicides on Si substrates is rather poor as mentioned in Section 6.3. This implies that there is a possibility of an unstable connection between the RE silicide thin film (or NW network) and the contacts. To improve this situation, deposition of thicker Au layer (more than 10 nm) will be helpful in Step 7 in Figure 6.1. Additional Au deposition after Ge passivation (Step 8 in Figure 6.1) will be worth trying as well.

Ex-situ deposited contacts (e.g. evaporation of 5nm of Ti and 200 nm of Au in the clean room) will be an alternate method, although this has the disadvantage that samples are no longer totally UHV-prepared. Electron-beam (e-beam) lithography is another alternative method for contact deposition. In this case, very fine electrons can be defined so that measurements can be done on much smaller scales.

The use of intrinsic Si wafers allows transport measurements at RT, because the intrinsic resistivity of Si (ρ_{Si} ~2.4×10^5 [Ω·cm] at RT) is nine orders of magnitude larger than that of RE silicide thin films ($\rho_{RE\ silicide}$ ~10^{-4} [Ω·cm] at RT) [170]. However, STM on such high resistivity wafers is problematic.

7.3 Single NW measurements

Single NW measurements are even more challenging, because the measurement dimension is at the nanoscale. Determination of the precise positioning of contacts on a NW is a key for this measurement. Figure 7.1 shows a schematic diagram of post growth deposited Au contacts for single NW measurements. In Step 1, a sparse network of NWs are grown in UHV chamber. *Ex-situ* alignment marks are fabricated by e-beam lithography (Step 2). After the registration of NWs and marks is determined by AFM, appropriately configured fine Au contacts (~50 nm) will be deposited by e-beam lithography. When sparse, parallel NWs are formed on a vicinal Si substrate [7], deposition of four contacts on a single NW would be very possible, because the length of these NWs can be microns in length.

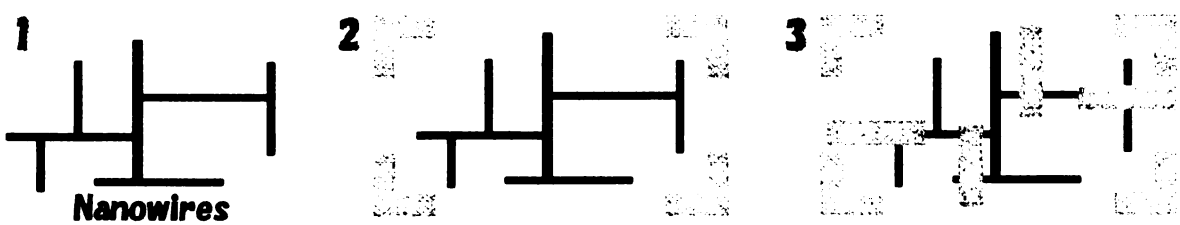

Figure 7.1 Post growth deposited contacts Step 1: Grow sparse network of NWs. Step 2: Deposit alignment marks: Use AFM to determine the NW/mark registration. Step 3: Deposit fine Au contacts.

7.4 Temperature dependence and magnetic-field dependence of magnetic, structural and transport properties of low-dimensional RE silicides

The investigation of magnetic properties of RE disilicide NWs and 3D islands at low temperature or in high magnetic field would be interesting topics, since the magnetism of one-dimensional (1D) systems is different from that of 2D or 3D systems. In case of Co atomic chains on a Pt substrate, long-range ferromagnetic order is stabilized by large anisotropy energy barriers which arise from large localized orbital moments [171, 172].

RE elements and bulk RE silicides have a variety of unusual magnetic properties. For example, several magnetic structures can be observed in heavy RE metals below RT: sinusoidal structure [Figure 7.2 (b)], circular cone structure [Figure 7.2 (d)], spiral antiferromagnetic structure [Figure 7.2 (e)], and ferromagnetic phase in the basal plane [Figure 7.2 (f)] [42]. Intermediate mixed phases, where the *c* axis component is modulated along the *c* axis (CAM structure) are often seen [Figures 7.2 (a)~(c)]. The same metal can have several of these structures at different temperatures.

Since the *4f* shell, which is responsible for almost all of the magnetism of RE ions, is localized deep inside the atoms and shielded by the filled outer *5s* and *5p* shells, it is not perturbed by the crystal field. Therefore, spin-orbit coupling (*LS*-coupling) dominantly contributes to the magnetic moment. Experimental results are fairly consistent with theoretical calculations as shown in Table 7.1. Although Sc, Y, La, Yb, and Lu ions are diamagnetic because of the absence of a partially filled *4f* shell (no unpaired electrons), they generally show paramagnetic behavior.

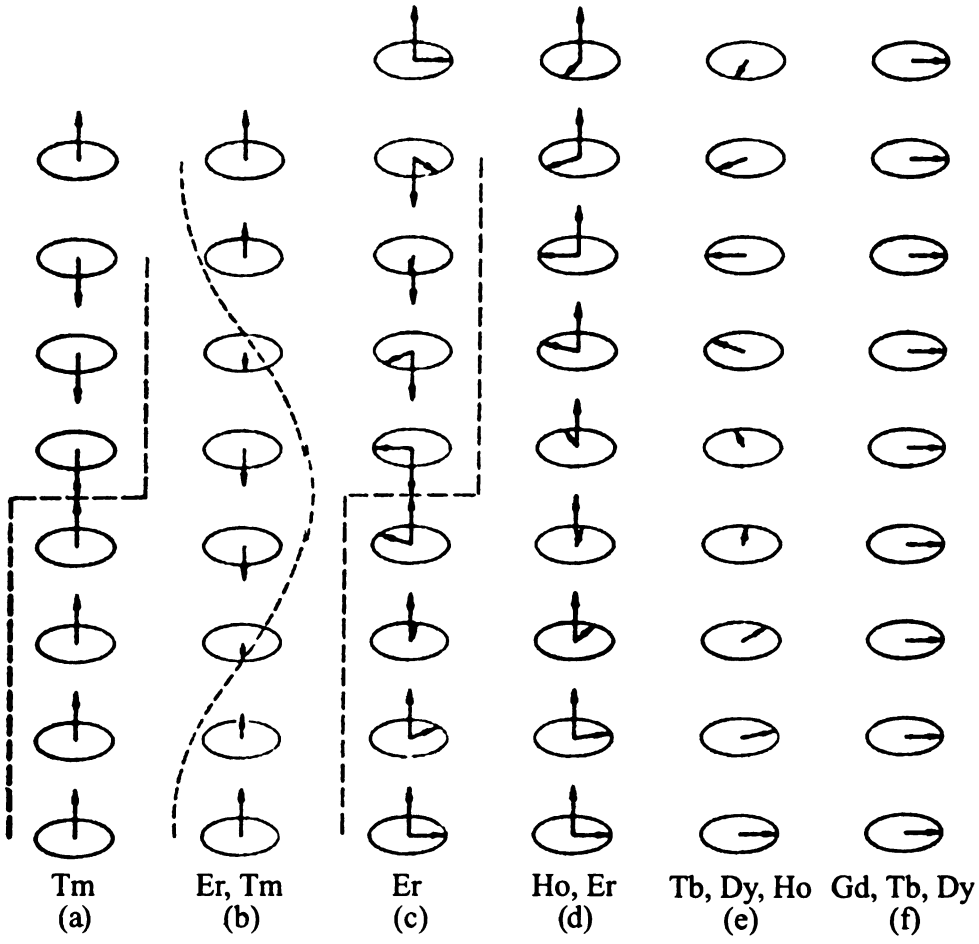

Figure 7.2 Magnetic structures of heavy RE metals [after Koehler (1972)] [42].

The magnetic properties of RE disilicides are also summarized in Table 7.2. There is a large variety of ordering: no magnetic ordering in $CeSi_2$, ferromagnetism in light RE silicides, $PrSi_2$ and $NdSi_2$, antiferromagnetism in heavy RE silicides, $GdSi_2$, $TbSi_2$, $DySi_2$, $HoSi_2$, and $ErSi_2$. Pierre *et al.* mentioned that these behaviors might be explained by the magnetocrystalline anisotropy, which is governed by the three different crystallographic structures (see Figure 1.1) in the series [173].

Before then, Sekizawa *et al.* described that the effective radial extent of *4f* wavefunction of RE metal may influence the sign of the exchange interaction J (J>0 for

ferromagnetic, and $J<0$ for antiferromagnetic) [174]. The theoretical calculation indicates that RE silicide compounds are ferromagnetic when the ratios of the radius of *4f* wavefunction to the half of the nearest neighbor distance of the RE ions in the silicide compounds, $r_{4f}/r_{N\text{-}N}$ is larger than 0.23~0.25 [174]. On the other hand, RE silicides are ferromagnetic when $r_{4f}/r_{N\text{-}N} < 0.23\text{~}0.25$. This result is consistent with the fact that the radial extent of *4f* wavefunction of light REs are much larger than that of heavy REs.

For transport properties of RE silicides, there is an abrupt decrease of resistivity at very low temperatures due to the antiferromagnetic ordering arising from the incomplete *4f* shell of the RE ion as described in Section 1.1.2.4.

Table 7.1 Bulk properties of RE elements [42, 175]

RE Ion	Electronic configuration	Ground State	$g[J(J+1)]^{1/2}$ (theory)	$g[J(J+1)]^{1/2}$ (experiment)	T_N (K)	T_C (K)	Easy direction at 4.2 K	$\theta_{//c}$ (K)	$\theta_{\perp c}$ (K)	Low temperature phase
Ce^{3+}	$4f^1 5s^2 p^6$	$^2F_{5/2}$	2.54	2.4						AF
Pr^{3+}	$4f^2 5s^2 p^6$	$^3H_4$	3.58	3.5	0.03	—	*a* axis			
					19.2[b]		*b* axis [b]			
Nd^{3+}	$4f^3 5s^2 p^6$	$^4I_{9/2}$	3.62	3.5	7.8[c]	—	*a* axis [c]			
					106 [b]		*a* axis			
Pm^{3+}	$4f^4 5s^2 p^6$	$^5I_4$	2.68	—						F
Sm^{3+}	$4f^5 5s^2 p^6$	$^6H_{5/2}$	0.84	1.5	14 [c]	—				complex
Eu^{3+}	$4f^6 5s^2 p^6$	$^7F_0$	0	3.4	90	—	<110>	18	18	spiral structure
Gd^{3+}	$4f^7 5s^2 p^6$	$^8S_{7/2}$	7.94	8.0	—	293	30° to *c* axis	317	317	F
Tb^{3+}	$4f^8 5s^2 p^6$	$^7F_6$	9.72	9.5	230	220	*b* axis	195	239	F
Dy^{3+}	$4f^9 5s^2 p^6$	$^6H_{15/2}$	10.63	10.6	178	86	*a* axis	121	169	F
Ho^{3+}	$4f^{10} 5s^2 p^6$	$^5I_8$	10.60	10.4	133	19	*b* axis	73	88	cone structure
Er^{3+}	$4f^{11} 5s^2 p^6$	$^4I_{15/2}$	9.59	9.5	84	18	30° to *c* axis	62	32.5	Ferri
Tm^{3+}	$4f^{12} 5s^2 p^6$	$^3H_6$	7.57	7.3	56	32	*c* axis	41	-17	Ferri
Yb^{3+}	$4f^{13} 5s^2 p^6$	$^2F_{7/2}$	4.54	4.5						

$g[J(J+1)]^{1/2}$: Effective number of Bohr magnetron (at RT); g: Landé *g* factor; T_N: Néel temperature;

T_C: Curie temperature; $\theta_{//c}$ and $\theta_{\perp c}$: paramagnetic Curie-Weiss temperatures for H // *c* and H $\perp$ *c*, respectively.

Ground state: $^{2S+1}L_J$ S and L are total spin and orbital angular momenta, respectively. J is a total angular momentum where J = |L-S| for less than half and J = L+S for more than half in the Hund's rule. [b]hexagonal sites; [c]cubic sites.

F: ferromagnetic; AF: antiferromagnetic; Ferri: ferrimagnetic.

Table 7.2 Magnetic properties of RE disilicides

Silicides	Crystallographic structure	θ_P (K)	μ_{eff} (μ_B)	T_{order} (K)	Magnetic structure	Ref
YSi_2					No magnetic ordering down to 4.2 K	[176]
$LaSi_2$					No magnetic ordering down to 4.2 K, but superconducting below 2.3 K	[176]
$CeSi_2$	T	-285	2.87		Nonmagnetic	[173]
$CeSi_2$	T		3.14		No magnetic ordering down to 100 mK	[177]
$PrSi_{1.9}$	T or O	-8 ± 3 (H // c_{hex}) 15 ± 2 (H⊥ c_{hex})		10.5	F ($\mu_s = 1\mu_B$ at 1.5 K)	[178]
$PrSi_2$	T	11	3.54	11	F	[173]
$PrSi_2$				11	F	[176]
				7	Second magnetic ordering transition	
$NdSi_{1.6}$	H	–30 (H // c_{hex}) 32 (H⊥ c_{hex})			F	[178]
				3.5	AF	
$NdSi_{1.73}$	O	-5 ± 2 (H // c) 8.5 ± 1 (H⊥ c)		10	F ($\mu_s = 1.4\ \mu_B$ at 1.5 K)	[83, 178]
$NdSi_{1.8}$	O	-10 ± 2 (H // c) 4 ± 1 (H⊥ c)		10	AF ($\mu_s = 1.68\ \mu_B$ at 1.3 K)	[178]
$NdSi_2$	O	-12	3.61	10	AF	[173]

θ_P: paramagnetic Curie-Weiss temperature; T_{order}: ordering transition temperature;
μ_B: Bohr magnetron = $e\hbar/2m_e = 9.27\times10^{-24}$ [J/T]; μ_{eff}: effective magnetic moment at RT; μ_s: spontaneous magnetization;
H: hexagonal; T: tetragonal; O: orthorhombic; F: ferromagnetic; AF: antiferromagnetic.

Table 7.2 (cont'd)

Silicides	Crystallographic structure	θ_P (K)	μ_{eff} (μ_B)	T_{order} (K)	Magnetic structure	Ref
$SmSi_2$					Paramagnetic down to 4.2 K	[176, 179]
$EuSi_2$				39	AF	[176]
				4.9	Second magnetic ordering transition	
$GdSi_{1.65}$	H	-53		33 ± 2	AF	[45]
Gd_5Si_5	H	-85	7.58	41	AF or spiral structure	[180]
$GdSi_{1.6-1.8}$	H			49~55	AF	[181]
				40, 41	Second magnetic ordering transition	
$GdSi_{1.85}$	O	-75	8.0	24	AF	[178]
$GdSi_2$	O	-75	8.13	26	AF	[173]
$GdSi_2$				39	AF	[176]
				25	Second magnetic ordering transition	
Tb_5Si_5	H	-42	9.79	38	AF or spiral structure	[180]
$TbSi_{1.6-1.7}$	H	-44~-47		32	AF or modulated structure	[45]
$TbSi_{1.7}$	O			38	AF	[87]
				16	Second magnetic ordering transition	
$TbSi_{1.8}$	O	-33		16	Short-range order at $T>T_N = 30$ K	[45]
$TbSi_2$	O	-33	9.62	16	AF	[173]
$TbSi_2$				17		[174, 176]
$DySi_{1.67-1.7}$	H			17	AF	[45]
				14	Second magnetic ordering transition	

Table 7.2 (cont'd)

Silicides	Crystallographic structure	θ_P (K)	μ_{eff} (μ_B)	T_{order} (K)	Magnetic structure	Ref
$DySi_{1.6}$	O			7	AF	[45]
Dy_3Si_5	H	+2	10.45	7	AF or spiral structure	[180]
$DySi_{1.75}$	O		6.3 (H // c) 5.2 (H ⊥ c)	10.5		[182]
$DySi_2$	O	-21	10.48	10.5	AF	[173]
$DySi_2$				18±1	AF	[174, 176]
$HoSi_{1.63}$	H	-19		17		[45]
$HoSi_{1.8}$	T + O	-12		14		
$HoSi_2$				14~18	AF	[174, 176]
$HoSi_2$	O	-12	10.52	14	AF	[173]
Er_3Si_5	H			4.4	AF	[29]
				3.1	Second magnetic ordering transition	
				1.7	Third magnetic ordering transition	
Er_3Si_5	H		~7.5 (H // c) 3.7 (H ⊥ c)	4.5	AF along the c axis F on the (0001) plane	[89]
$ErSi_2$					No magnetic ordering down to 4.2 K	[174, 176]
$ErSi_2$	H	-9.5	9.48	4.5	F	[173]
Tm_3Si_5	H			2.1~2.6	AF	[29]
$TmSi_2$				4.2	AF	[176]
$YbSi_2$	H				No magnetic ordering	[29]
Lu_3Si_5	H				No magnetic ordering, possible superconducting	[29]

APPENDIX A Hydrogen-passivation of Si(001) surface and $DySi_2$ NWs

A Si surface which is terminated by monolayers of hydrogen (H) protects against surface oxidation when the sample is exposed to air. It has been reported that the H-passivated Si(001) surface remains atomically pristine after 15 minutes ambient exposure [183]. In addition, the oxidation is not observed on this surface by X-ray photoelectron spectroscopy (XPS) after almost two days of ambient exposure. Our interest in H adsorption was the potential to use it as a passivation against oxidation of our NW samples in the course of doing the *ex-situ* transport measurements.

Interaction of atomic H with Si(001) surface was first presented by T. Sakurai *et al.* in 1976 [184]. They found that a H-saturated Si(001) surface produces 2×1 monohydride (M) and 1×1 dihydride (D) phases as shown in Figure A1. Later on, Y.J. Chabal *et al.* reported the presence of both M and D phases in the 3×1 structure [185].

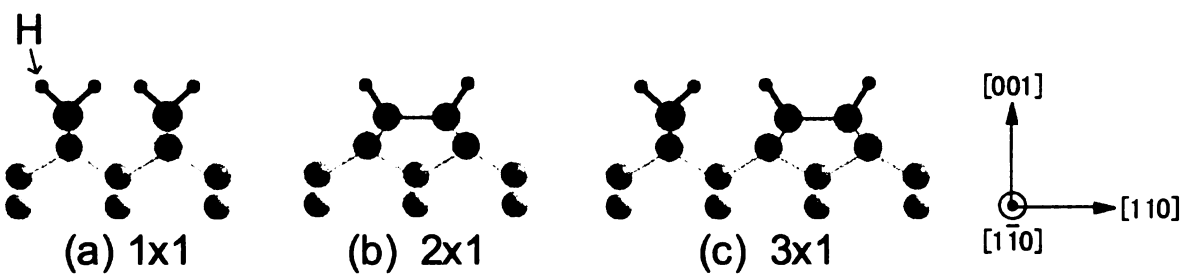

Figure A1 Schematic of the various possible hydrogenated structures on Si(001) surface.

On the bulk-terminated surface [Figure 2.8 (a)], each Si atom has two dangling bonds. The 1×1 D phase is obtained when two H atoms are attached on each Si atom [Figure A1 (a)] adopting a bulklike 1×1 structure. A 2×1 reconstructed Si(001) surface has one

dangling bond per Si atom. A 2×1 M phase is obtained when one H atom is attached to the rest of dangling bond on each Si atom without changing the superstructure [Figure A1 (b)]. The 'intermediate' 3×1 phase consists of alternating M and D sites [Figure A1 (c)]. In considering the relationship between the coverage and the hydride phases, the 2×1 M phase completely covers the surface at the coverage of 1.0 ML, since the ratio of H and Si atoms on the surface is one to one. For 1×1 D phase, there are double the number of H atoms on surface. Hence, the whole surface is covered with 1×1 D phase at the coverage of 2.0 ML. The coverage associated with 3×1 phase is 4/3 (=1.33) ML because four H atoms exist on every three Si atoms. Table A1 lists the H exposure conditions needed to prepare different types of surfaces.

The STM work on the H-Si(001) system has studied subjects such as surface structure [186-195], electronic structure [196-200], adsorption and desorption [106, 201-219], dangling bond structures [220-223], and oxidation in air [183, 224-228]. In particular, we can also use the STM tip to selectively desorb H from the surface to produce nanoscale patterns.

To prepare the H-terminated Si(001) surface, the sample is first cleaned in the same way as the experimental procedure described in Chapter 2. A 20-min atomic H exposure with the chamber pressure of 4×10^{-8} Torr seems to be sufficient to saturate the whole surface. The sample surface is exposed to atomic H produced by dissociating H_2 with a 1600°C W-filament placed 1 cm away from the sample. During the H exposure, the sample is heated at 330°C [Figures A2 and A3]. For the sample with $DySi_2$ NWs [Figure A4], H exposure is done at RT.

Table A1 Structure of the H-saturated Si(001) surface and H exposure conditions.

Surface structure	H exposure conditions (substrate temperature)	Ref
Monohydride (M) 2×1	Moderate RT dose	[187]
	Saturation dose at 600~650 K	[185, 187, 229]
Domains of 3×1 on the 2×1 phase (STM)	400~600 K	[211]
M+D 3×1	380±20 K	[185]
Dihydride (D) 1×1	Large dose at RT	[185]
2×1→3×1→1×1 (LEED)	Additional dose at 400 K	[230]
3×1→2×1 (LEED)	A mild annealing at 575 K	[185]
2×1→1×1→2×1 (LEED)	Additional dose at RT, then annealing at 600 K	[185]

Figure A2 (a) shows the schematic diagram of a Si dimer 'before' and 'after' H-passivation. For the 2×1 M structure, one H atom can attach to each Si dangling bond to fill the empty states. Therefore, in STM images, the brightness of the maxima 'before' and 'after' H-passivation appears different. The empty- and filled-state images of H-passivated Si(001) surface with 10-min H exposure are shown in Figures A2 (b) and A2 (c), respectively. Small white spots are contamination coming from the H source. In both images, the half left side is the depassivated area produced by STM-induced H desorption. H atoms are desorbed by applying high tip voltage. Here, a sample bias voltage of +8 V is used. In empty states [Figure A2 (b)], the depassivated surface appears brighter than the H-passivated surface because it corresponds to bare Si surface. In filled states [Figure A2 (c)], the H-passivated surface appears brighter than the depassivated surface because the electron density is higher when H atom is absorbed on the dangling bond.

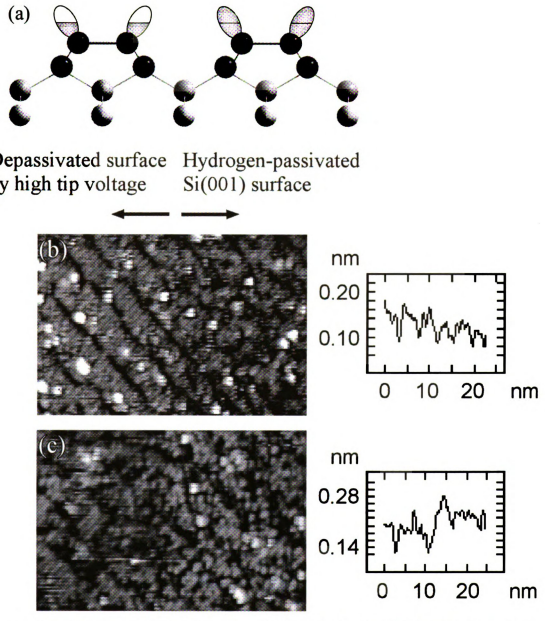

Figure A2 (a) Schematic diagram of a Si dimer 'before' and 'after' H-passivation. A half-filled π^* anti-bonding orbital is completely filled due to H-desorption. (b) Empty-state (1.74 V) and (c) filled-state (-1.82 V) images of H-passivated Si(001) surface. The left half of the images is the surface after it was passivated by applying high tip voltage (20×30 nm^2). Cross-sectional profile in the horizontal direction is shown next to each STM image.

This H desorption mechanism can be used for nanoscale patterning as shown in Figure A3. By manipulating the tip position and the voltage, the letters "MSU" have been

patterned with a bias voltage of +8 V. The average linewidth is ~10 nm. It is known that the desorption yield depends on the sample bias voltage [212]. A wider linewidth is obtained as the sample bias voltage increases.

Figure A3 STM image (90×120 nm^2) of a H-passivated Si(001) surface. Brighter areas correspond to an STM-induced H desorption. By operating the tip position and the voltage, we can write a "MSU" logo!

So far no study of a H-saturated RE silicide film on Si(001) substrate has been done, although there are a few studies of H adsorption on Er silicide films on Si(111) [231-237]. LEED studies show that at low H exposures on $ErSi_{1.7}$(0001), H is absorbed in the same manner as on Si(111), confirming that Er silicide is terminated by a buckled Si plane without Si vacancies [231, 234]. Moreover, H is not only *adsorbed* on but also *absorbed* in the layer. It is suggested that this form of chemisorbed H corresponds to a saturation of the dangling bonds related to the Si vacancies in the silicide bulk. H-passivation of both external and internal dangling bonds strongly stabilizes the films [233].

Here, our attempt of H passivation of $DySi_2$ NWs on Si(001) substrate is briefly reported. Figures A4 (a) and A4 (b) show the 'before' H-passivation of $DySi_2$ NWs on

Si(001) at 0.80 ML and 'after' H-passivation of the same surface, respectively. Although there are small gaps on the NWs shown by white arrows [Figure A4 (b)], the structures of NWs still survive after H-passivation. The change in the electrical properties of NWs due to the small gaps is unknown. There are no changes in the H-induced features on the NWs after an attempt to depassivate at +8V on the tip. This fact is very different from the depassivated Si(001) surface as shown in Figures A2 (b) and A2 (c). This implies that the bonding between the H atom and the RE silicide is stronger than that between H and Si.

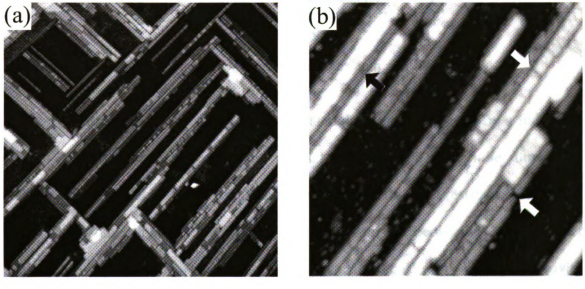

Figure A4 (a) Before H-passivation: $DySi_2$ NWs on Si(001) at 0.80 ML (180×180 nm^2). (b) After H-passivation: NWs still survive, although there are small gaps on the NWs shown by white arrows (50×50 nm^2). The change in the electrical properties of NWs due to the small gaps is unknown.

APPENDIX B Sheet Resistance [238, 239]

The resistance R of a thin film with a length l, width w, thickness t, and resistivity ρ can be written as

$$R = \rho\frac{l}{wt} = R_s\frac{l}{w} \ [\Omega] \qquad R_s \equiv \frac{\rho}{t} \ [\Omega/\text{square}]$$

where R_S is the sheet resistance of a layer. Here, we assume that the current density is uniform throughout the film.

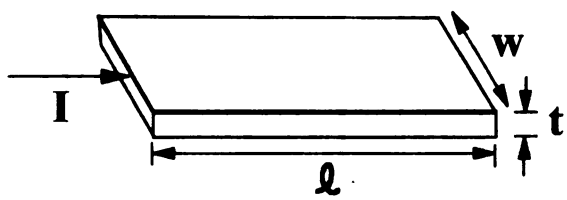

Figure B1 Schematic diagram of current passing through a thin film.

Sheet resistance is a resistance of a film, material, or layer measured by a four-point probe. The resistance represents the parallel resistance of an infinite number of infinitely thin parallel sheets. Strictly speaking, the unit for sheet resistance is the ohm (since l/w is dimensionless). However, to avoid confusion between R and R_S, sheet resistance is expressed as *ohms per square area* which is equal to the average resistivity of a layer divided by the thickness of the layer.

FYI

$$\rho = \frac{1}{\sigma} = \frac{m}{ne^2\tau} [\Omega\cdot\text{cm}]$$

where m, n, e, and τ are the electron mass, electron density, electron charge, and relaxation time, respectively.

APPENDIX C Two- and four-terminal measurements [240]

To measure a sample resistance R, the easiest way is to pass a constant current through the sample as shown in Figure C1. A known voltage V_o is connected to a series circuit consisting of a sample resistor R and a ballast resistor R_B. R_B is chosen to be $R_B >> R$ so that the current is $I = V_o/(R+R_B) \sim V_o/R_B$, which is independent of change in R.

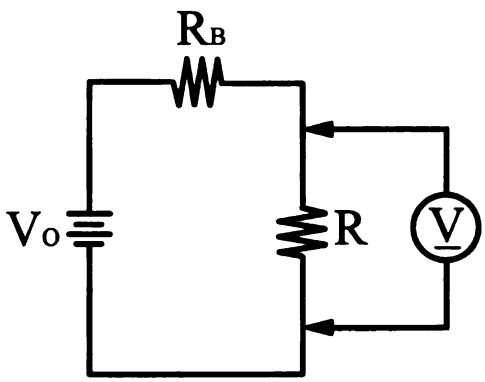

Figure C1 Constant-current circuit using a ballast resistor.

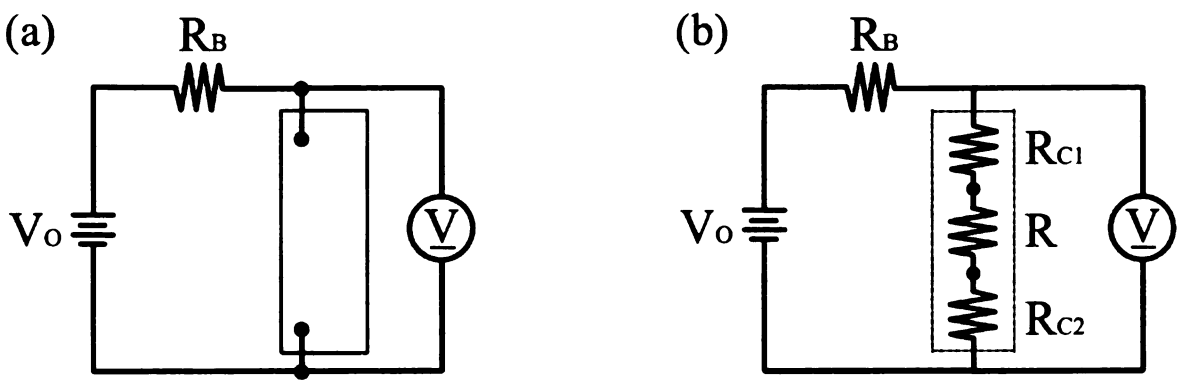

Figure C2 (a) Circuit showing a two-terminal resistance measurement. (b) Equivalent circuit for (a).

Figures C2 (a) and C2 (b) show a circuit for a two-terminal resistance measurement and its equivalent circuit, respectively. When the sample is connected to the circuit as in Figure C2 (a), the measured voltage drop V is $V = I(R_{C1} + R + R_{C2})$ as in Figure C2 (b),

where R_{C1} and R_{C2} are the contact resistances. Therefore, we are not measuring the sample resistance R itself but a sum of the sample resistance R and contact resistances R_{C1} and R_{C2}.

To eliminate the contact resistances from the total resistance, four-terminal connections are used as shown in Figure C3 (a). In four-terminal measurement, current leads are separated from voltage leads. Figure C3 (b) shows the equivalent circuit of Figure C3 (a). The current and voltage contacts are labeled as $R_{C1} \sim R_{C4}$. Since the contact resistances R_{C1} and $R_{C2} << R_B$, the current I is still $I = V_o/(R_B + R_{C1} + R + R_{C2}) \sim V_o/R_B$. A sample voltage is measured between the other two contacts with a voltmeter which has very large input impedance so that it draws very little current. Since no current will flow through the contact resistances R_{C3} and R_{C4}, the voltage drop across the sample can be measured as $V = IR$.

Unless the sample resistance is comparable with the internal resistance of the voltmeter, contact resistances R_{C3} and R_{C4} have no effect on the measurements.

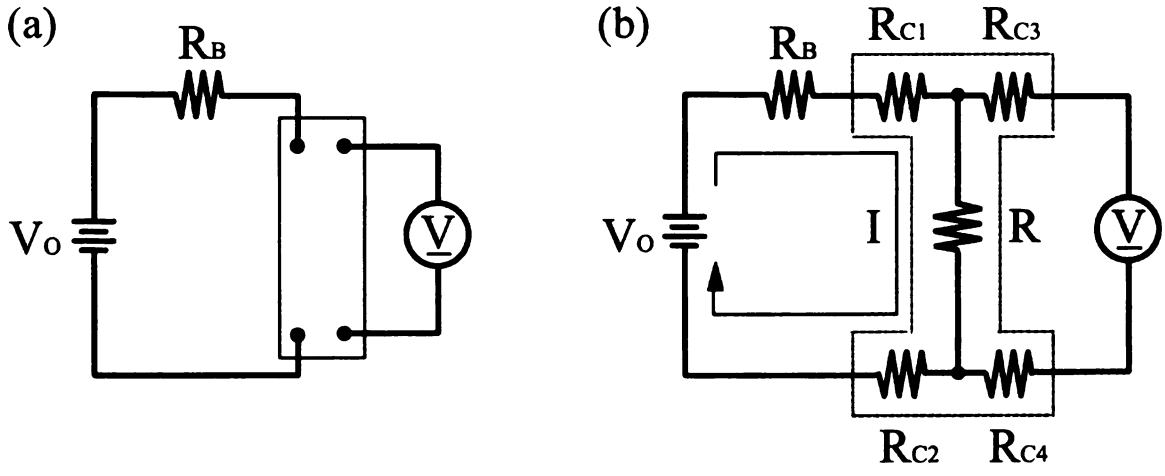

Figure C3 (a) Circuit showing a four-terminal resistance measurement. (b) Equivalent circuit for (a).

APPENDIX D Van der Pauw's method

The surface resistivity of a sample ρ can be determined from four-terminal resistances in the vertical and horizontal directions, R_{vertical} and $R_{\text{horizontal}}$. For a flat sample of anisotropic material of arbitrary shape with four points, van der Pauw equation [241, 242] is given by

$$\exp\left\{-\pi d\frac{R_{\text{vertical}}}{(\rho_x\rho_y)^{1/2}}\right\}+\exp\left\{-\pi d\frac{R_{\text{horizontal}}}{(\rho_x\rho_y)^{1/2}}\right\}=1 \quad (1)$$

where ρ_x and ρ_y are principal values of the resistivity in the plane of the sample, and d is the thickness of a sample (or thin film). From equation (1), $(\rho_x\rho_y)^{1/2}$ is obtained.

If the sample is rectangular in shape and the four contacts are placed at the corners of the sample, the second equation is derived as

$$(\rho_x/\rho_y)^{1/2}=-\frac{b}{a\pi}\ln\left\{\tanh\left[\frac{\pi d R_{\text{horizontal}}}{16(\rho_x\rho_y)^{1/2}}\right]\right\} \quad (2)$$

where a and b are the sides of the rectangle [243].

From $(\rho_x\rho_y)^{1/2}$ and $(\rho_x/\rho_y)^{1/2}$, the individual values of the principal resistivity can be obtained:

$$\begin{cases}\rho_x=(\rho_x\rho_y)^{1/2}\times(\rho_x/\rho_y)^{1/2}\\ \rho_y=(\rho_x\rho_y)^{1/2}\div(\rho_x/\rho_y)^{1/2}\end{cases}$$

In our transport measurements (Section 6.3), we assumed $\rho_x = \rho_y$ for simplicity. Therefore the surface resistivity of the sample ρ is given by equation (1), which is $\rho\equiv(\rho_x\rho_y)^{1/2}$.

APPENDIX E List of publications

1. Nogami, J., B.Z. Liu, M.V. Katkov, and C. Ohbuchi, *Self-Assembled rare earth silicide nanowires on Si(001).* Phys. Rev. B, 2001. **63**: p. 233305.

2. Ohbuchi, C. and J. Nogami, *Holmium growth on Si(001): surface reconstructions and nanowire formation.* Phys. Rev. B, 2002. **66**: p. 165323.

3. Ohbuchi, C. and J. Nogami, *Samarium induced surface reconstructions of Si(001)* (published)

4. Ohbuchi, C., W. Swiech, and J. Nogami, *Topographic evolution of Dy silicide on Si(001): Shape transitions from nanowires to 3D islands* (in preparation)

BIBLIOGRAPHY

[1] C. Preinesberger, S. Vandre, T. Kalka, and M. Dahne-Prietch, *Formation of dysprosium silicide wires on Si(001)*, J. Phys. D: Appl. Phys. **31**, p.L43 (1998).

[2] *http://www.nytimes.com/library/tech/99/11/biztech/articles/01nano.html.*

[3] Y. Chen, D.A.A. Ohlberg, G. Medeiros-Ribeiro, Y.A. Chang, and R.S. Williams, *Self-assembled growth of epitaxial erbium disilicide nanowires*, Appl. Phys. Lett. **76**(26), p.4004-4006 (2000).

[4] M. Katkov and J. Nogami. *Growth of Yttrium on Si(001).* in *Bulletin of the American Physical Society, March meeting*. 2002.

[5] Y. Chen, D.A.A. Ohlberg, and R.S. Williams, *Nanowires of four epitaxial hexagonal silicides grown on Si(001)*, J Appl. Phys. **91**(5), p.3213-3218 (2002).

[6] R. Ragan, Y. Chen, D.A.A. Ohlberg, G. Medeiros-Ribeiro, and R.S. Williams, *Ordered arrays of rare-earth silicide nanowires on Si(001)*, J. Crystal Growth **251**, p.657 (2003).

[7] B.Z. Liu and J. Nogami, *Growth of parallel rare earth silicide nanowire arrays on vicinal Si(001)*, Nanotechnology **14**(8), p.873-877 (2003).

[8] D. Lee and S. Kin, *Formation of hexagonal Gd disilicide nanowires on Si(100)*, Appl. Phys. Lett. **82**(16), p.2619-2621 (2003).

[9] J. Nogami, B.Z. Liu, M.V. Katkov, C. Ohbuchi, and N.O. Birge, *Self-Assembled rare earth silicide nanowires on Si(001)*, Phys. Rev. B **63**, p.233305 (2001).

[10] B.Z. Liu and J. Nogami, *An STM Study of the Si(001) (2x4)-Dy Surface*, Surf. Sci. **488**, p.399-405 (2001).

[11] C. Preinesberger, S.K. Becker, S. Vandre, T. Kalka, and M. Dahne, *Structure of DySi2 nanowires on SI(001)*, J Applied Physics **91**(3), p.1695-1697 (2002).

[12] B.Z. Liu and J. Nogami, *An STM study of DySi2 nanowires growth on Si(001)*, J Applied Physics **93**(1), p.593-599 (2003).

[13] J. Nogami, *Growth and characterization of atomic and nanometer scale wires on the silicon surface*, Surface Review and Letters **7**(5-6), p.555-560 (2000).

[14] C. Ohbuchi and J. Nogami, *Holmium growth on Si(001): surface reconstructions and nanowire formation*, Phys. Rev. B **66**, p.165323 (2002).

[15] Y. Chen, D.A.A. Ohlberg, G. Medeiros-Ribeiro, Y.A. Chang, and R.S. Williams., *Growth and evolution of epitaxial erbium disilicide nanowires on Si(001)*, Appl. Phys. A **75**, p.353-361 (2002).

[16] J.S. Yang, Q. Cai, X.D. Wang, and R. Koch, *Morphological evolution of erbium disilicide nanowires on Si(001)*, Surf. Interface Anal. **36**, p.104-108 (2004).

[17] M. Kuzmin, P. Laukkanen, R.E. Perala, R.-L. Vaara, and I.J. Vayrynen, *Formation of ytterbium silicide nanowires on Si(001)*, Appl. Surf. Sci. **222**, p.394 (2004).

[18] Z. He, D.J. Smith, and P.A. Bennett, unpublished.

[19] J.L. McChesney, A. Kirakosian, R. Bennewitz, J.N. Crain, J.-L. Lin, and F.J. Himpsel, *Gd disilicide nanowires attached to Si(111) steps*, Nanotechnology **13**, p.545-547 (2002).

[20] Z. He, M. Stevens, D.J. Smith, and P.A. Bennett, *Dysprosium silicide nanowires on Si(110)*, Appl. Phys. Lett. **83**(25), p.5292-5294 (2003).

[21] K.A. Gschneidner and L.R. Eying, *Handbook on the Physics and Chemistry of Rare Earths*. Electronic structure of rare earth metals, ed. S.H. Liu. Vol. **1**. 1978: North-Holland Publishing Company.

[22] A. Chatterjee and A.K. Singh, *Pressure-Induced Electronic Collapse and Structural Changes in Rare-Earth Monochalcogenides*, Phys. Rev. B **6**(6), p.2285-2291 (1972).

[23] A. Stenborg, O. Bjorneholm, A. Nilsson, N. Martensson, J.N. Andersen, and C. Wigren, *Valence changes and core-level shifts of Sm adsorbed on Mo(110)*, Phys. Rev. B **40**(9), p.5916-5923 (1989).

[24] H. Norde, J.d.S. Pires, F. d'Heurle, F. Pesavento, S. Petersson, and P.A. Tove, *The Schottky-barrier height of the contacts between some rare-earth metals (and silicides) and p-type silicon*, Appl. Phys. Lett. **38**(11), p.865 (1981).

[25] K.N. Tu, R.D. Thompson, and B.Y. Tsaur, *Low Schottky barrier of rare-earth silicide on n-Si*, Appl. Phys. Lett. **38**(8), p.626-628 (1981).

[26] R.D. Thompson, B.Y. Tsaur, and K.N. Tu, *Contact reaction between Si and rare earth metals*, Appl. Phys. Lett. **38**(7), p.535-537 (1981).

[27] A. Franciosi, J.H. Weaver, P. Perfetti, A.D. Katnani, and G. Margaritondo, *Samarium valence changes and reactive interdiffusion at the Si(111)-Sm interface*, Solid State Communications **47**(6), p.427 (1983).

[28] G. Rossi, J. Nogami, I. Lindau, L. Braicovich, I. Abbati, U.d. Pennino, and S. Nannarone, *First Spectroscopic Investigation of the Yb / Si Interface at Room Temperature*, Journal of Vacuum Science and Technology A **1**(2), p.781 (1983).

[29] L.D. Woolf, *Transport and magnetic properties of layered rare earth disilicides*, Solid State Communications **47**(7), p.519-523 (1983).

[30] E. Houssay, A. Rouault, O. Thomas, R. Madar, and J.P. Senateur, *Metallurgical Reinvestigation of Rare Earth Silicides*, Appl. Surf. Sci. **38**, p.156-161 (1989).

[31] A. Iandelli and A. Palenzona, in: Handbook on the Physics and Chemistry of Rare Earths (North-Holland Publishing Company, 1978) vol.2 Alloys and intermetallics, ch.13.

[32] G. Rossi, *d and f metal interface formation on silicon*, Surf. Sci. Rep. **7**, p.1 (1987).

[33] F.P. Netzer, *Rare earth overlayers on silicon*, J. Phys. Condens. Matter **7**, p.991-1022 (1995).

[34] S. Auffret, J. Pierre, B. Lambert, J.L. Soubeyroux, and J.A. Chromoczek, *Crystallographic and magnetic-structures of Er_3Si_5*, Physica B **163**(3), p.271-280 (1990).

[35] V.M. Koleshko, V.F. Belitsky, and A.A. Khodin, *Thin-films of rare-earth-metal silicides*, Thin Solid Films **141**(2), p.277-285 (1986).

[36] J.A. Knapp and S.T. Picraux, *Epitaxial growth of rare-earth silicides on (111) Si*, Appl. Phys. Lett. **48**(7), p.466-468 (1986).

[37] A. Iandelli, A. Palenzona, and G.L. Olcese, *Valence Fluctuations of Ytterbium in Silicon-rich compounds*, Journal of Less Common Metals **64**, p.213-220 (1979).

[38] O. Thomas, C.S. Petersson, and F.M. Dheurle, *The reaction of scandium thin-films with silicon - diffusion, nucleation, resistivities*, Appl. Surf. Sci. **53**, p.138 (1991).

[39] R. Baptist, S. Ferrer, G. Grenet, and H.C. Poon, *Surface Crystallography of YSi2-x Films Epitaxially Grown on Si(111): An X-Ray Photoelectron Diffraction Study*, Phys. Rev. Lett **64** p.311-314 (1990).

[40] M.-A.Nicolet and S.S. Lau, *Formation and characterization of transition-metal silicides*, VLSI electronics -Mictostructure Science Vol.6 Eds N.G. Einspruch, G.B. Larrabee (1983), and references therein.

[41] C.C. Hsu, Y.X. Wang, J. Hu, J. Ho, and J.J. Qian, *The effect of thermal treatment on the thin-film reaction of La, Ce, and Nd on silicon surfaces*, J. Vac. Sci. Technol. A **7**(5), p.3016-3022 (1989).

[42] K.A. Gschneidner and L.-R. Eyring, *Handbook on the Physics and Chemistry of Rare Earths; and references therein.* vol.1 Metals (1978) ; vol.2 Alloy and Intermetallics (1979); and references therein: North-Holland Publishing Company.

[43] A. Vantomme, M.F. Wu, S. Hogg, U. Wahl, W. Deweerd, H. Pattun, G. Langouche, S. Jin, and H. Bender, *Stabilization and phase transformation of hexagonal rare-earth silicides on Si(111)*, Nuclear Instruments and Methods B **17**, p.261-266 (1999).

[44] M.L. Huang, J.H. Yang, Y.A. Chang, R. Ragan, Y. Chen, D.A.A. Ohlberg, and R.S. Williams, *Phase stabilities of ternary rare earth metal disilicides*, Appl. Phys. A **78**(1), p.1 (2004).

[45] S. Auffret, J. Pierre, B. Lambert-Andron, R. Madar, E. Houssay, D. Schmitt, and E. Siaud, *Magnetic properties versus crystal structure in heavy rare-earth silicides RSi2-x*, Physica B **173**, p.265-276 (1991).

[46] N. Frangis, G.V. Tendeloo, J.V. Landuyt, G. Kaltsas, A. Travlos, and A.G. Nassiopoulos, *New Erbium Silicide Superstructures: A Study by High Resolution Electron Microscopy*, Phys. Stat. Sol. **158**, p.107-116 (1996).

[47] J.E. Baglin, F.M. d'Heurle, and C.S. Petersson, Appl. Phys. Lett. **36**(7), p.594-596 (1980).

[48] I. Gerocs, G. Molnar, E. Jaroli, E. Zsoldos, G. Peto, J. Gyulai, and E. Bugiel, *Epitaxy of orthorhombic gadolinium disilicide on <100> silicon*, Appl. Phys. Lett. **52**(25), p.2144-2145 (1987).

[49] J.Y. Duboz, P.A. Badoz, F.A. Davitaya, and J.A. Chroboczek, *Electronic transport-properties of epitaxial erbium silicide silicon heterostructures*, Appl. Phys. Lett. **55**(1), p.84-86 (1989).

[50] L. Stauffer, A. Mharchi, C. Pirri, P. Wetzel, D. Bolmont, and G. Gewinner, *Electronic structure and interfacial geometry of epitaxial two-dimensional Er silicide on Si(111)*, Phys. Rev. B **47**(16), p.10555-10562 (1993).

[51] M. Lohmeier, W.J. Huisman, G.t. Horst, P.M. Zagwijn, and E. Vlieg, *Atomic structure and thermal stability of two-dimensional Er silicide on Si(111)*, Phys. Rev. B **54**(3), p.2004-2009 (1996).

[52] C. Wigren, J.N. Andersen, and R. Nyholm, *Sm- and Yb-induced reconstructions of the Si(111) surface*, Phys. Rev. B **48**, p.11014-11019 (1993).

[53] R. Hofmann, W.A. Henle, F.P. Netzer, and M. Neuber, *Electronic-structure of epitaxial Yb silicide*, Phys. Rev. B **46**(7), p.3857-3864 (1992).

[54] C. Wigren, J.N. Andersen, R. Nyholm, U.O. Karlsson, J. Nogami, A.A. Baski, and C.F. Quate, *Adsorption-site determination of ordered Yb on Si(111) Surfaces*, Phys. Rev. B **47**(15), p.9663-9668 (1993).

[55] W.A. Henle, M.G. Ramsey, F.P. Netzer, and L. Horn, *Formation of divalent Eu silicides at the Eu-Si(111) interface*, Surface Science **254**(1-3), p.182-190 (1991).

[56] S. Vandre, T. Kalka, C. Preinesberger, and M. Dahne-Prietch, *Epitaxial growth and electronic structure of lanthanide silicides on n-type Si(111)*, J. Vac. Sci. Technol. B **17**(4), p.1682-1690 (1999).

[57] T.V. Krachino, M.V. Kuz'min, M.V. Loginov, and M.A. Mittsev, *Yb and Sm Adsorption and Silicide Formation on Si(111) Surface*, Phys. Low-Dim. Struct. **9/10**, p.95-106 (1999).

[58] M.V. Kuz'min, N.V. Mikhailov, and M.A. Mittsev, *Formation and properties of a binary adsorbed layer in a two-component adsorption system (Sm+Yb)-Si(111)*, Phys. Sol. Sta. **45**(3), p.579-585 (2003).

[59] T.V. Krachino, M.V. Kuz'min, M.V. Loginov, and M.A. Mittsev, *Growth of an Eu-Si(111) thin film structure: The stage of silicide formation*, Phys. Sol. Sta. **46**(3), p.563-568 (2004).

[60] S. Vandre, T. Kalka, C. Preinesberger, I. Manke, H. Eisele, M. Dahne-Prietsch, R. Meier, E. Weschke, and G. Kaindl, *Growth and electronic structure of Dy silicide on Si(111)*, Appl. Surf. Sci. **123**, p.100-103 (1998).

[61] C.H. Luo, G.H. Shen, and L.J. Chen, *Vacancy ordering structures in epitaxial $RESi_{2-x}$ thin films on (111)Si and (001)Si*, Appl. Surf. Sci. **113/114**, p.457 (1997).

[62] A. Travlos, N. Salamouras, and N. Boukos, *Growth, structure and electrical properties of epitaxial thulium silicide thin films on silicon*, J. Appl. Phys. **81**(3), p.1217-1221 (1997).

[63] J.C. Chen, G.H. Shen, and L.J. Chen, *Interfacial reactions of Gd thin films on (111) and (001)Si*, Appl. Surf. Sci. **142**, p.291-294 (1999).

[64] Y.K. Lee, N. Fujimura, and T. Ito, *Epitaxial-growth of Yttrium silicide YSi_{2-x} on(100) Si*, J. Alloys Comp. **193**(1-2), p.289-291 (1993).

[65] S. Kinnou, J.Y. Veuillen, and T. Tan, *Formation and electronic-properties of erbium silicide on Si(100)*, Surf. Sci. **307**(Part A), p.258-263 (1994).

[66] G. Kaltsas, A. Travlos, N. Salamouras, A.G. Nassiopoulos, P. Revva, and A. Traserse, *Erbium silicide films on (100) silicon, grown in high vacuum. Fabrication and properties*, Thin Solid Films **275**(1-2), p.87-90 (1996).

[67] N. Frangis, J.V. Landuyt, G. Kaltsas, A. Travlos, and A.G. Nassiopoulos, *Growth of erbium-silicide on (100) silicon as characterized by electron microscopy and diffraction*, J. Crystal Growth **172**, p.175-182 (1997).

[68] A. Travlos, N. Salamouras, and N. Boukos, *Epitaxial dysprosium silicide films on silicon: growth, structure and electrical properties*, Thin Solid Films **397**, p.138-142 (2001).

[69] A. Travlos, P. Aloupogiannis, E. Rokofyllou, and C. Papastaikoudis, *Epitaxial lutetium silicide: Growth, characterization and electrical properties*, J Applied Physics **72**(3), p.948-952 (1992).

[70] G. Peto, G.L. Molnar, Z.E. Horvath, E. Zsoldos, N.Q. Khanh, J. Gyulai, and J. Kanski, *Formation of epitaxial $HoSi_2$ layer on Si(100)*, Thin Solid Films **318**, p.168-171 (1998).

[71] M.V. Katkov and J. Nogami, *Yb and Nd growth on Si(001)*, Surf. Sci. **524**(1-3), p.129-136 (2003).

[72] B.Z. Liu and J. Nogami, *An STM study of the Si(001)(2x7)-Gd, Dy surface*, Surf. Sci. **540**(1), p.136-144 (2003).

[73] P.J. Godowski, J. Onsgaard, F. Orskov, and M. Christiansen, *structural aspects of the Sm/Si(100) interface*, J. Mater. Sci. Lett. **9**, p.989 (1990).

[74] J.S. Yang, Q. Cai, X.D. Wang, and R. Koch, *Initial stages of erbium disilicide formation on Si(001)*, Surf. Sci. **526**, p.291-296 (2003).

[75] M. Kuzmin, R.E. Perala, P. Laukkanen, R.-L. Vaara, M.A. Mittsev, and I.J. Vayrynen, *Initial stages of Yb/Si(100) interface growth: 2x3 and 2x6 reconstructions*, Appl. Surf. Sci. **214**(1-4), p.196-207 (2003).

[76] L. Fitting, M.C. Zeman, W.C. Yang, and R.J. Nemanich, *Influence of strain, surface diffusion and Ostwald ripening on the evolution of nanostructures for erbium on Si(001)*, J Appl. Phys. **93**(7), p.4180-4184 (2003).

[77] F.M. Dheurle, M.O. Aboelfotoh, F. Pesavento, and C.S. Petersson, *Schottky barriers of scandium and scandium monosilicide on silicon*, Appl. Surf. Sci. **53**, p.237-239 (1991).

[78] F.U. Hillebrecht, *Interaction of Ce with Si(100)*, Appl. Phys. Lett. **55**(3), p.277-279 (1989).

[79] M.H. Unewisse and J.W.V. Storey, *Electrical and infrared investigation of erbium silicide*, J Appl. Phys. **72**(6), p.2367-2371 (1992).

[80] A. Travlos and N. Salamouras, *Superconductivity of lanthanum silicide thin films*, Vacuum **48**(1), p.13-14 (1997).

[81] S.M. Hogg and A. Vantomme, *Growth and electrical characterization of GeSi1.7 epilayers formed by channeled ion beam systhesis*, J Appl. Phys. **91**(6), p.3664-3668 (2002).

[82] A. Travlos, N. Salamouras, and E. Flouda, *Epitaxial erbium silicide films on (100) silicon: growth, structure and electrical properties*, Appl. Surf. Sci. **120**, p.355-364 (1997).

[83] J. Pierre, S. Auffret, J.A. Chroboczek, and T.T.A. Nguyen, *Magnetotransport in the rare earth silicides RSi2-x*, J. Phys.: Condens. Matter **6**, p.79-92 (1994).

[84] C. Boragno and M.R. Bonansinga, *Electrical and magnetic properties of ErSi2 and GdSi2 alloy thin films*, Solid State Communications **92**(6), p.515-518 (1994).

[85] A. Travlos, P. Aloupogiannis, E. Pokofyllou, and C. Papastaikoudis, *Growth, characterization and electrical properties of gadolinium silicide thin layers*, phil. Mag. B **67**(4), p.485-495 (1993).

[86] G. Guizzetti, E. Mazzega, M. Michelini, and F. Nava, *Electrical and optical characterization of $GdSi_2$ and $ErSi_2$ alloy thin films*, J Applied Physics **67**(7), p.3393-3399 (1989).

[87] F.H. Kaatz, J.V.d. Spiegal, and W.R. Graham, *Anomolous magnetotransport in epitaxial $TbSi_{2-x}$*, J. Vac. Sci. Technol **9**(3), p.426-429 (1991).

[88] S.M. Hogg, A. Vantomme, M.F. Wu, and G. Langouche, *Electrical properties of rare earth silicides produced by channeled ion beam synthesis*, Microelectron Eng. **50**, p.211-215 (2000).

[89] J. Chroboczek, *Transport and magnetic properties of rare earth compounds epitaxially grown on semiconductors*, Acta Physica Polonica A **80**(2), p.179-192 (1991).

[90] E.P. Wohlfarth, Ferromagnetic materials: a handbook on the properties of magnetically ordered substances (North-Holland, Amsterdam, 1980).

[91] J.M. Ziman, Electrons and phonons: the theory of transport phenomena in solids, Oxford, 2001, chapter 9.

[92] A. Franciosi, P. Perfetti, A.D. Katnani, and J.H. Weaver, *Samarium chemisorption on group-IV semiconductors*, Phys. Rev. B **29**(10), p.5611 (1984).

[93] R.G. Long, M.C. Bost, and J.E. Mahan, *Metallic behavior of lanthanum disilicide*, Appl. Phys. Lett. **53**(14), p.1272-1273 (1988).

[94] F. Canepa, S. Cirafici, F. Merlo, and A. Palenzona, *Electrical resistivity in the R_5Si_3 systems (R=La, Ce, Pr, Nd, Sm)*, J. Alloys Comp. **203**, p.L11-L13 (1994).

[95] W.E. Henry, Bulletin of the American Physical Society **7**, p.474 (1962).

[96] X. Zhenjia, *Electrical transport in RE silicides*, Properties of metal silicides: Eds K. Maex, M. Rossum (1995) IMEC. Leuven, Belgium and references therein, (1994).

[97] D. Tsamakis, M. Vlachos, A. Travlos, and N. Salamouras, *Electrical properties of crystalline Er and Dy silicide layers*, Thin Solid Films **418**, p.211-214 (2002).

[98] F. Canepa, S. Cirafici, F. Merlo, and A. Palenzona, *Electrical resistivity measurements on some R5Si3 phases: R=Gd, Tb, Lu and Y*, J. Magn. Magn. Mater. **118**, p.182-186 (1993).

[99] V.N. Eremenko, V.E. Listovnichii, S.P. Luzan, Y.I. Buyanov, and P.S. Martsenyuk, *Phase diagram of the holmium-silicon binary system and physical properties of holmium silicides up to 1050C*, J. Alloys Comp. **219**, p.181-184 (1995).

[100] G. Binnig, H. Rohrer, C. Gerber, and E. Weibel, *Tunneling through a controllable vacuum gap*, Appl. Phys. Lett. **40**(2), p.178-180 (1982).

[101] G. Binnig, H. Rohrer, C. Gerber, and E. Weibel, *Surface Studies by Scanning Tunneling Microscopy*, Phys. Rev. Lett. **49**(1), p.57-60 (1982).

[102] G. Binnig, H. Rohrer, C. Gerber, and E. Weibel, *7x7 reconstruction on Si(111) resolved in real space*, Phys. Rev. Lett. **50**, p.120 (1983).

[103] D.M. Eigler and E.K. Schweizer, *Positioningsingle atoms with a scanning tunneling microscope*, Nature **344**, p.524-526 (1990).

[104] L.J. Whitman, J.A. Stroscio, R.A. Dragoset, and R.J. Celotta, *Manipulation of adsorbed atoms and creation of new structures on room-temperature surfaces with a scanning tunneling microscope*, Science **251**, p.1206-1210 (1991).

[105] H. Uchida, D. Huang, F. Grey, and M. Aono, *Site-Specific Measurement of Adatom Binding Energy Differences by Atom Extraction with the STM*, Phys. Rev. Lett. **70**(13), p.2040-2043 (1993).

[106] T.C. Shen, C. Wang, G.C. Abeln, J.R. Tucker, J.W. Lyding, P. Avouris, and R.E. Walkup, *Atomic scale desorption through electronic and vibrational excitation mechanisms*, Science **268**(1590), (1995).

[107] P. Avouris, *Manipulation of matter at the atomic and molecular levels*, Acc. Chem. Res. **28**, p.95-102 (1995).

[108] S. Hosaka, S. Hosoki, T. Hasegawa, H. Koyanagi, T. Shintani, and M. Miyamoto, *Fabrication of nanostructures using scanning probe microscopes*, J. Vac. Sci. Technol **B13**, p.2813 (1995).

[109] T.A. Jung, R.R. Schlittler, J.K. Gimzewski, H. Tang, and C. Joachim, *Controlled Room-Temperature Positioning of Individual Molecules: Molecular Flexure and Motion*, Science **271**(5246), p.181-184 (1996).

[110] G. Dujardin, A. Mayne, O. Robert, F. Rose, C. Joachim, and H. Tang, *Vercical Manipulation of Individual Atoms by a Direct STM Tip-Surface Contact on Ge(111)*, Phys. Rev. Lett **80**(14), p.3085-3088 (1998).

[111] U.J. Quaade, K. Stokbro, R. Lin, and F. Grey, *Single-atom reversible recording at room temperature*, Nanotechnology **12**, p.265-272 (2001).

[112] Y. Okawa and M. Aono, *Nanoscale control of chain polymerization*, Nature **409**(683), (2001).

[113] R. Bennewitz, J.N. Crain, A. Kirakosian, J.-L. Lin, J.L. McChesney, D.Y. Petrovykh, and F.J. Himpsel, *Atomic scale memory at a silicon surface*, Nanotechnology **13**(499-502), (2002).

[114] S.W. Hla and K.H. Rieder, *Engineering single molecules with a scanning tunneling microscope tip*, Superlarrices and microstructures **31**(1), p.63-72 (2002).

[115] K. Sattler, *Nanolithography using the scanning tunneling microscope*, Jap. J. Appl. Phys. Part1 **42**(7B), p.4825-4829 (2003).

[116] O. Dudko, A.E. Filippov, J. Klafter, and M. Urbakh, *Manipulatioons of individual molecules by scanning probes*, Nano Letters **3**(6), p.795-798 (2003).

[117] S.D. Barrett, *http://www.imagesxm.org.uk/.*

[118] J.A. Kubby and J.J. Boland, *Scanning tunneling microscopy of semiconductor surfaces*, Surface Science Reports **26**, p.61-204 (1996).

[119] J.A. Stroscio and W.J. Kaiser, Scanning Tunneling Microscopy, Academic Press Inc. (1993) ch.1 and ch.4 and references therein.

[120] W. Telieps and E. Bauer, *An analytical reflection and emission UHV surface electron microscope*, Ultramicroscopy **17**, p.57-66 (1985).

[121] E. Bauer, in: Proc. 5th Intern. Congr. on Electron Microscopy (Academic Press, New York, 1962), p.D-11.

[122] R.M. Tromp and M.C. Reuter, *Design of a new photo-emission/low-energy electron microscope for surface studies*, Ultramicroscopy **36**, p.99-106 (1991).

[123] R.M. Tromp, *Low-energy electron microscopy*, IBM J. Res. Develop. **44**(4), p.503-516 (2000).

[124] E. Bauer, *Photoelectron Microscopy*, J. Phys.: Condens. Matter **13**, p.11391-11404 (2001).

[125] E. Bauer, *Methods of surface studies depending on inelastic-scattering of electrons*, Vacuum **22**(11), p.539-552 (1972).

[126] R.M. Tromp and M.C. Reuter, *Imaging with a low-energy electron microscope*, Ultramicroscopy **50**, p.171-178 (1993).

[127] *http://www.ulvac-phi.co.jp/PDF/taguchi01.pdf.*

[128] M. Aono, Y. Hou, C. Oshima, and Y. Ishizawa, *Low-energy ion scattering from the Si(001) surface*, Phys. Rev. B **49**(8), p.567 (1982).

[129] W.S. Yang and F. Jona, *Atomic structure of Si(001) 2x1*, Phys. Rev. B **28**(4), p.2049 (1983).

[130] H. Over, J. Wasserfall, W. Ranke, C. Ambiatello, R. Sawitzki, D. Walf, and W. Moritz, *Surface atomic geometry of Si(001)-(2x1): A low-energy electron-diffraction structure analysis*, Phys. Rev. B **55**(7), p.4731 (1997).

[131] J.A. Appelbaum, G.A. Baraff, and D.R. Hamann, *Si(001) surface reconstruction: spectroscopic selection of a structural model*, Phys. Rev. Lett. **35**, p.729 (1975).

[132] D.J. Chadi, *Si(100) surfaces: Atomic and electronic structures*, J. Vac. Sci. Technol **16**, p.1290-1296 (1979).

[133] A. Redondo and W.A. Goddard, *Electronic correlation and the Si(100) surface: Buckling versus nonbuckling*, J. Vac. Sci. Technol. **21**(2), p.344-350 (1982).

[134] Z. Jing and J.L. Whitten, *Ab initio studies of H chemisorption on Si(100)*, Phys. Rev. B **46**(15), p.9544 (1992).

[135] Y. Jung, Y. Shao, M.S. Gordon, D.J. Doren, and M. Head-Gordon, *Are both symmetric and buckled dimers on Si(100) minima? Density functional and multireference perturbation theory calculations*, J. Chem. Phys. **119**(20), p.10917 (2003).

[136] S. Gasiorowicz, Quantum Physics - second edition: Wiley, p.334 (1996).

[137] J.A. Appelbaum, G.A. Baraff, and D.R. Hamann, *The Si(100) surface. III. Surface reconstruction*, Phys. Rev. B **14**(2), p.588-601 (1976).

[138] O.L. Alerhand, D. Vanderbilt, R.D. Meade, and J.D. Joannopoulos, *Spontaneous formation of stress domains on crystal surfaces*, Appl. Phys. Lett. **61**(17), p.1973-1976 (1988).

[139] *http://www.research.ibm.com/leem/.*

[140] R.M. Tromp, R.J. Hamers, and J.E. Demuth, *Si(001) dimer structure observed with scanning tunneling microscopy*, Phys. Rev. Lett. **55**, p.1303-1306 (1985).

[141] T. Tabata, T. Aruga, and Y. Murata, *Order-disorder transition on Si(001) -C(4X2)TO(2X1)*, Surface Science **179**, p.L63 (1987).

[142] Y. Enta, S. Suzuki, and S. Kono, *Angle-resolved-photoemission study of the electronic structure of the Si(001) c(4x2) surface*, Phys. Rev. Lett **65**, p.2704 (1990).

[143] R.A. Wolkow, *Direct observation of an increase in buckled dimer on Si(001) at low-temperature*, Phys. Rev. Lett **68**, p.2636 (1992).

[144] A. Ramstad, G. Brocks, and P.J. Kelly, *Theoretical study of the Si(001) surface reconstruction*, Phys. Rev. B **51**(20), p.14504-14523 (1995).

[145] G. LeLay, A. Criecenti, C. Ottaviani, P. Perfetti, T. Tanikawa, I. Matsuda, and S. Hasegawa, *Evidence of asymmetric dimers down to 40 K at the clean Si(100) surface*, Phys. Rev. B **66**, p.153317 (2002).

[146] K. Hata, S. Yoshida, and H. Shigekawa, *p(2x2) Phase of Buckled Dimers of Si(100) Observed on n-Type Substrates below 40 K by Scanning Tunneling Microscopy*, Phys. Rev. Lett **89**, p.286104 (2002).

[147] M. Matsumoto, K. Fukutani, and T. Okano, *Low-Energy Electron Diffraction Study of the Phase Transition of Si(001) Surface below 40 K*, Phys. Rev. Lett **90**, p.106103 (2003).

[148] R. Stalder, H. Sirringhaus, N. Onda, and H.V. Kanel, *Observation of misfit dislocations in epitaxial $CoSi_2$/Si(111) layers by scanning tunneling microscopy*, Appl. Phys. Lett. **59**(16), p.1960-1962 (1991).

[149] K. Ojima, M. Yochimura, and K. Ueda, *STM observation of the 2x3 and c(2x6) structures on Ba/Si(001)*, Surf. Sci. **491**(1-2), p.169 (2001).

[150] D.E. Jones, J.P. Pelz, Y. Hong, E. Bauer, and I.S.T. Tsong, *Striped Phase and Temperature Dependent Step Shape Transition on Highly B-Doped Si(001)-(2x1) Surfaces*, Phys. Rev. Lett. **77**(2), p.330 (1996).

[151] J.-F. Nielsen, H.-J. Im, and J.P. Pelz, *Scanning tunneling microscope studies of boron-doped Si(001)*, J. Vac. Sci. Tec. A **17**(4), p.1670 (1999).

[152] D.E. Jones, J.P. Pelz, Y.H. Xie, P.J. Silverman, and G.H. Gilmer, *Enhanced Step Waviness on SiGe(001)-(2x1) Surface under Tensile Strain*, Phys. Rev. Lett. **75**(8), p.1570 (1995).

[153] K.M. Chen, D.E. Jesson, S.J. Pennycook, M. Mostoller, and T. Kaplan, *Step Instabilities: A New Kinetic Route to 3D Growth*, Phys. Rev. Lett. **75**(8), p.1582 (1995).

[154] G. Ye, J. Nogami, and M.A. Crimp (submitted).

[155] O.P. Balkashin, A.G.M. Jansen, O. Laborde, U. Gottlieb, G.L. Sukhodub, P. Wyder, and I.K. Yanson, *High-Frequency Point-Contact Spectroscopy of $TiSi_2$, $TaSi_2$, and VSi2*, J. Low Temp. Phys. **129**(314), p.105-116 (2002).

[156] C.C. Lin, W.S. Chen, K.Y.J. Hsu, H.K. Liou, and K.N. Tu, *Reliability study of sub-micron titanium silicide contacts*, Appl. Surf. Sci. **92**, p.660-664 (1996).

[157] N.M. Ravindra, L. Jin, D. Ivanov, V.R. Mehta, L.M. Dieng, G. Popov, O.H. Gokce, J. Grow, and A.T. Fiory, *Electrical and Compositional Properties of $TaSi_2$ Films*, J. of Elec. Matls. **31**(10), p.1074-1079 (2002).

[158] G. Medeiros-Ribeiro, D.A.A. Ohlberg, D.R. Bowler, R.E. Tanner, G.A.D. Briggs, and R.S. Williams, *Titanium disilicide nanostructures: two phases and their surfaces*, Surf. Sci. **431**, p.116-127 (1999).

[159] K.L. Saenger, J. C. Cabral, L.A. Clevenger, R.A. Roy, and S. Wind, *A kinetic study of the C49 to C54 TiSi2 conversion using electrical resistivity measurements on single narrow lines*, J. Appl. Physics **78**(12), p.7040-7044 (1995).

[160] P. Gallais, J.J. Hantzpergue, and L.C. Remy, *Sputter deposition of thin tantalum layers and low temperature interactions between tantalum and SiO_2 and tantalum and silicon*, Thin Solid Films **165**, p.227-236 (1988).

[161] M.T. Huang, T.L. Martin, V. Malhotra, and J.E. Mahan, *Electronic transport properties of tantalum disilicide thin films*, J. Vac. Sci. Technol **B3**(3), p.836-845 (1985).

[162] H. Oppolzer, F. Neppl, K. Hieber, and V. Huber, *Influence of slight deviations from TaSi2 stoichiometry on the high-temperature stability of tantalum silicide/silicon contacts*, J. Vac. Sci. Technol **B2**(4), p.630-635 (1984).

[163] S.B. Herner and K.S. Jones, *Investigation of mechanisms of vacancy generation in silicon in the presence of a $TaSi_2$ film*, J. Appl. Phys. **82**(2), p.583-588 (1997).

[164] O.V. Hul'ko, R. Boukherroub, and G.P. Lopinski, *Chemical and thermal stability of titanium disilicide contacts on silicon*, J Appl. Phys. **90**(3), p.1655-1659 (2001).

[165] N. Lundqvist, J. Aberg, S. Nygren, C.-A. Bjormander, and S.-L. Zhang, *Effects of substrate bias and temperature during titanium sputter-deposition on the phase formation in $TiSi_2$*, Microelectron Eng. **60**, p.211-220 (2002).

[166] A.W. Dunn, B.N. Cotier, A. Nogaret, P. Moriarty, and P.H. Beton, *Molecular scale alignment strategies: An investigation of Ag adsorption on patterned fullerene layers*, Appl. Phys. Lett. **71**(20), p.2937-2939 (1997).

[167] P.A. Bennett, B. Ashcroft, Z. He, and R.M. Tromp, *Growth dynamics of titanium silicide nanowires observed with low-energy electron microscopy*, J. Vac. Sci. Tec. B **20**(6), p.2500-2504 (2002).

[168] W.-C. Yang, H. Ade, and R.J. Nemanich, *Shape stability of $TiSi_2$ islands on Si(111)*, J. Appl. Physics **95**(3), p.1572-1576 (2004).

[169] E. Abramof, A.F.d. Silva, B.E. Sernelius, J.P.d. Souza, and H. Boudinov, *Metal-nonmetal transition and resistivity of silicon implanted with bismuth*, J. Mater. Res. **12**(3), p.641-645 (1997).

[170] *http://www.tydex.ru/materials/materials2/Si.html.*

[171] P. Gambardella, A. Dallmeyer, K. Maiti, M.C. Malagoli, W. Eberhardt, K. Kern, and C. Carbone, *Ferromagntism in one-dimensional monatomic metal chanis*, Nature **416**(6878), p.301 (2002).

[172] P. Gambardella, *Magnetism in monatomic metal wires*, J. Phys. Condens. Matter **15**, p.S2533-S2546 (2003).

[173] J. Pierre, E. Siaud, and D. Frachon, *Magnetic Properties of Rare Earth Disilicides RSi2*, J. Less-Common Met. **139**, p.321-329 (1988).

[174] K. Sekizawa and K. Yasukochi, *Antiferromagnetism of Disilicides of Heavy Rare Earth Metals*, J. Phys. Soc. Jpn. **21**, p.274 (1966).

[175] C. Kittel, *Introduction to Solid State Physics*. 6 ed. 1986.

[176] S. Labroo, X. Zhang, P. Hill, and N. Ali, *Electrical and magnetic properties of antiferromagnetic rare earth disilicides*, J. Less-Common Met. **149**, p.337 (1989).

[177] H. Yashima, T. Satoh, H. Mori, D. Watanabe, and T. Ohtsuka, *Thermal and magnetic properties and crystal structures of $CeGe_2$ and $CeSi_2$*, Solid State Communications **41**(1), p.1-4 (1982).

[178] J. Pierre, S. Auffret, E. Siaud, R. Madar, E. Houssay, A. Rouault, and J.P. Senateur, *Magnetic properties of rare earth silicide crystals RSi2-x (R = Pr, Nd, Gd)*, J. Magn. Magn. Mater. **89**, p.86-96 (1990).

[179] B.T. Matthias, E. Corenzwit, and W.H. Zachriasen, Phys. Rev. **112**, p.89 (1958).

[180] K.S.V.L. Narasimhan and H. Steinfink, *Magnetic Investigations on AlB2 Type Structures*, J. Solid State Chem. **10**, p.137-141 (1973).

[181] C. Pescher, J. Pierre, A. Ermolieff, and C. Vannuffel, *Magnetic properties of gadolinium silicide thin films produced by different fabrication processes*, Thin Solid Films **278**, p.140-143 (1996).

[182] J. Pierre, B. Lambert-Andron, and J.L. Soubeyroux, *Magnetic-structures of rare earth silicides $NdSi_{2-x}$, $HoSi_{2-x}$, $DySi_{2-x}$*, J. Magn. Magn. Mater. **81**, p.39 (1988).

[183] M.C. Hersam, N.P. Guisinger, and J.W. Lyding, *Atomic-level study of the robustness of the Si(100)-2x1:H surface following exposure ro ambient conditions*, Appl. Phys. Lett. **78**(7), p.886-888 (2001).

[184] T. Sakurai and H.D. Hagstrum, *Interplay of the monohydride phase and a newly discovered dihydride phase in chemisorption of H on Si(100)2x1*, Phys. Rev. B **14**, p.1593-1596 (1976).

[185] Y.J. Chabal and K. Raghavachari, *New Ordered Structure for the H-Saturated Si(100) Surface: The (3x1) Phase*, Phys. Rev. Lett **54**(10), p.1055-1058 (1985).

[186] M. Niwa, H. Iwasaki, and S. Hasegawa, *Hydrogen terminated Si(100) surfaces studied by scanning tunneling microscopy, X-ray photon spectroscopy, and auger-electron spectroscopy*, J. Vac. Sci. Tec. A **8**(1), p.266-269 (1990).

[187] J.J. Boland, *Structure of the H-saturated Si(100) surface*, Phys. Rev. Lett. **65**, p.3325-3328 (1990).

[188] J.J. Boland, *Role of bond-strain in the chemistry of hydrogen on the Si(100) surface*, Surface Science **261**(1-3), p.17-28 (1992).

[189] Y. Okada, H. Shimomura, and M. Kawabe, *Atomic image observation of hydrogen-saturated Si(100) prepared by atomic-hydrogen irradiation*, Jap. J. Appl. Phys. Part2-Letters **31**(8A), p.L1121-L1123 (1992).

[190] K. Kitahara and O. Ueda, *Observation of atomic-structure by scanning-tunneling -microscopy of vicinal Si(100) surface annealed in hydrogen gas*, Jap. J. Appl. Phys. Part2-Letters **33**(11B), p.L1571-L1573 (1994).

[191] M. Yoshimura and K. Ueda, *Evolution of surface structures on Si(001) during hydrogen desorption*, Appl. Surf. Sci. **121**, p.179-182 (1997).

[192] T. Komeda and Y. Kumagai, *Si(001) surface variation with annealing in ambient H_2*, Phys. Rev. B **58**(3), p.1385-1391 (1998).

[193] K. Arima, K. Endo, T. Kataoka, Y. Oshikane, H. Inoue, and Y. Mori, *Scanning tunneling microscopy study of hydrogen-terminated Si(001) surfaces after wet cleaning*, Surface Science **446**(1-2), p.128-136 (2000).

[194] T. Hashizume, H. Kajiyama, Y. Suwa, S. Heike, S. Matsuura, J. Nara, and T. Ohno, *Adsorption of Si atom on H-terminated Si(001)-2x1 surface*, Appl. Surf. Sci. **216**(1-4), p.15-18 (2003).

[195] Y. Suwa, S. Matsuura, M. Fujimori, S. Heike, T. Onogi, H. Kajiyama, T. Hitosugi, K. Kitazawa, T. Uda, and T. Hashizume, *Dopant-pair structures segregated on a hydrogen-terminated Si(100) surface*, Phys. Rev. Lett **90**(15), p.156101 (2003).

[196] T. Hirosugi, T. Hashizume, S. Heike, Y. Wada, S. Watanabe, T. Hasegawa, and K. Kitazawa, *Scanning tunneling spectroscopy of dangling-bond wires fabricated on the Si(100)-2x1-H surface*, Appl. Phys. A **66**, p.S695-S699 (1998).

[197] J.A. Schaefer, *Electronic and structural-properties of hydrogen on semiconductor surfaces*, Physica B **170**(1-4), p.45-68 (1991).

[198] E.J. Buehler and J.J. Boland, *Dimer preparation that mimics the transition state for the adsorption of H-2 on the Si(100)-2x1 surface*, Science **290**(5491), p.506-509 (2000).

[199] K. Bobrov, G. Comtet, G. Dujardin, and L. Hellner, *Electronic structure of partially hydrogenated Si(100)-(2 x 1) surfaces prepared by thermal and nonthermal desorption*, Phys. Rev. Lett **86**(12), p.2633-2636 (2001).

[200] D.X. Chen and J.J. Boland, *Chemisorption-induced disruption of surface electronic structure: Hydrogen adsorption on the Si(100)-2x1 surface*, Phys. Rev. B **65**(16), p.165336 (2002).

[201] J.J. Boland, *Evidence of pairing and its role in the recombinative desorption of hydrogen from the Si(100)-2x1 surface*, Phys. Rev. Lett **67**(12), p.1539 (1991).

[202] J.J. Boland, *Scanning tunneling microscopy study of the adsorption and recombinative desorption of hydrogen from the Si(100)-2x1 surface*, J. Vac. Sci. Tec. A **10**(4), p.2458-2464 (1992).

[203] X.D. Wang, H. Lu, T. Hashizume, H.W. Pickering, and T. Sakurai, *Atomic-hydrogen chemisorption on Si(100)(2x1) studied by FI-STM*, Appl. Surf. Sci. **57**(1-4), p.266-274 (1993).

[204] G.C. Abeln, T.C. Shen, J.R. Tucker, and J.W. Lyding, *Nanoscale STM-patterning and chemical modification of the Si(100) surface*, Microelectron Eng. **27**(1-4), p.23-26 (1995).

[205] P. Avouris, R.E. Walkup, A.R. Rossi, T.C. Shen, G.C. Abeln, J.R. Tucker, and J.W. Lyding, *STM-induced H atom desorption from Si(100): Isotope effects an site selectivity*, Chem. Phys. Lett. **257**(1-2), p.148-154 (1996).

[206] J.W. Lyding, T.C. Shen, G.C. Abeln, C. Wang, and J.R. Tucker, *Nanoscale patterning and selective chemistry of silicon surfaces by ultrahigh-vacuum scanning tunneling microscopy*, Nanotechnology **7**(2), p.128-133 (1996).

[207] J.W. Lyding, T.C. Shen, G.C. Abeln, C. Wang, P.A. Scott, J.R. Tucker, P. Avouris, and R.E. Walkup, *Ultrahigh vacuum scanning tunneling microscope-based nanolithography and selective chamistry on silicon surfaces*, Israel J. Chem. **36**(1), p.3-10 (1996).

[208] D.H. Huang and Y. Yamamoto, *Manipulating atoms one by one with a scanning tunneling microscope*, Surf. Rev. Lett. **3**(3), p.1463-1472 (1996).

[209] T. Hitosugi, T. Hashizume, S. Heike, S. Watanabe, Y. Wada, T. Hasegawa, and K. Kitazawa, *Scanning tunneling spectroscopy of dangling-bond wires fabricated on the Si(100)-2x1-H surface*, Jap. J. Appl. Phys. Part2-Letters **36**(3B), p.L361-L364 (1997).

[210] M. Sakurai, C. Thirstrup, T. Nakaya, and M. Aono, *Local modification of hydrogen-terminated silicon surfaces by clean and hydrogen-covered STM tips*, Surf. Sci. **386**(1-3), p.154-160 (1997).

[211] C. Thirstrup, M. Sakurai, T. Nakayama, and M. Aono, *Atomic scale modifications of hydrogen-terminated silicon 2x1 and 3x1 surfaces by scanning tunneling microscope*, Surf. Sci. **411**, p.203-214 (1998).

[212] C. Syrykh, J.P. Nys, B. Legrand, and D. Stievenard, *Nanoscale desorption of H-passivated Si(100)-2x1 surfaces using an ultrahigh vacuum scanning tunneling microscope*, J Appl. Phys. **85**(7), p.3887-3892 (1999).

[213] Q. Shi, D.H. Huang, and G.S. Zhu, *Vibrational-energy redistribution in single-atom manipulation by scanning tunneling microscope*, Jap. J. Appl. Phys. Part1 **38**(6B), p.3856-3659 (1999).

[214] K. Stokbro, U.J. Quaade, R. Lin, C. Thirstrup, and G. Grey, *Electronic mechanism of STM-induced diffusion of hydrogen on Si(100)*, Faraday Discussions **117**, p.231-240 (2000).

[215] M. Durr, Z.H. Hu, A. Biedermann, U. Hofer, and T.F. Heinz, *Real-space study of the pathway for dissociative adsorption of H-2 on Si(001)*, Phys. Rev. Lett **88**(4), p.046104 (2002).

[216] M.C. Hersam, N.P. Guisinger, J. Lee, K.G. Cheng, and J.W. Lyding, *Variable temperature study of the passivation of dangling bonds at Si(100)-2x1 reconstructed surfaces with H and D*, Appl. Phys. Lett. **80**(2), p.201-203 (2002).

[217] Z.H. Hu, *Quantitative study of adsorbate-adsorbate interactions of hydrogen on the Si(100) surface*, Phys. Rev B **68**(15), p.155418 (2003).

[218] H. Tsurumaki, K. Iwamura, T. Karato, S. Inanaga, and A. Namiki, *Adsorption and desorption of deuterium on partially oxidized Si(100) surfaces*, Phys. Rev. B **67**(15), p.155316 (2003).

[219] L. Soukiassian, A.J. Mayne, M. Carbone, and G. Dujardin, *Atomic-scale desorption of H atoms from the Si(100)-2x1 : H surface: Inelastic electron interactions*, Phys. Rev. B **68**(3), p.035303 (2003).

[220] T. Hashizume, S. Heike, M.I. Lutwyche, S. Watanabe, and Y. Wada, *Atom structures on the Si(100) surface*, Surface Science **386**(1-3), p.161-165 (1997).

[221] T. Hitosugi, T. Hashizume, S. Heike, H. Kajiyama, Y. Wada, S. Watanabe, T. Hasegawa, and K. Kitazawa, *Electronic structures of dangling-bond structures fabricated on hydrogen-terminated Si(100)-2x1 surfaces*, Deffect and Diffusion Forum/Journal **162**, p.43-57 (1998).

[222] T. Hitosugi, S. Heike, T. Onogi, T. Hashizume, S. Watanabe, Z.Q. Li, K. Ohno, Y. Kawazoe, T. Hasegawa, and K. Kitazawa, *Jahn-Teller distortion in dangling-bond linear chains fabricated on a hydrogen-terminated Si(100)-2 x 1 surface*, Phys. Rev. Lett **82**(20), p.4034-4037 (1999).

[223] R.P. Chen and D.S. Lin, *Distribution of dangling bond pairs on partially hydrogen-terminated Si(100) surface observed by scanning tunneling microscopy*, Surf. Sci. **454**, p.196-200 (2000).

[224] H. Jungblut, D.J. Muller, M. Aggour, and H.J. Lewerenz, *Scanning-tunneling-microscopy observation of atomic structures on silicon (100) surface in air*, Electrochimica Acta **38**(10), p.1367-1371 (1993).

[225] N. Kramer, M.R. vandenBerg, and C. Schonenberger, *Scanning tunneling microscope-induced oxidation of hydrogen passivated silicon surfaces*, Thin Solid Films **282**(1-2), p.637-639 (1996).

[226] H. Kijiyama, S. Heike, Y. Wada, and T. Hashizume, *Initial stage oxidation at an unpaired dangling bond site on a Si(100)-2 X 1-H surface*, Thin Solid Films **344**(Sp. Iss. SI), p.550-553 (1999).

[227] Z.H. Mai, Y.F. Lu, W.D. Song, and W.K. Chim, *Nano-modification on hydrogen-passivated Si surfaces by a laser-assisted scanning tunneling microscope operating in air*, Appl. Surf. Sci. **154**, p.360-364 (2000).

[228] D.A. MacLaren, N.J. Curson, P. Atkinson, B. Holst, D.J. Johnson, and W. Allison, *Simple design for the transportation of ex situ prepared hydrogen passivated silicon*, J. Vac. Sci. Tec. A **20**(1), p.285-287 (2002).

[229] S. Maruno, H. Iwasaki, K. Horioka, S.T. Li, and S. Nakamura, *Electronic structures of the monohydride (2x1):H and dihydride (1x1)::2H Si(001) surfaces studied by angle-resolved electron-energy-loss spectroscopy*, Phys. Rev. B **27**(7), p.4110-4116 (1983).

[230] D.T. Jiang, G.W. Anderson, K. Griffiths, T.K. Sham, and P.R. Norton, *Adsorption of atomic hydrogen on Si(199)-2x1 at 400 K*, Phys. Rev. B **48**(7), p.4952-4955 (1993).

[231] J.Y. Veuillen and T.A.N. Tan, *Hydrogen adsorption on $ErSi_{1.7}$(0001)*, Phys. Rev. B **52**(15), p.10796-10799 (1995).

[232] S. Saintenoy, P. Wetzel, C. Pirri, J.C. Peruchetti, D. Bolmont, and G. Gewinner, *Hydrogen adsorption on erbium silicide surface*, Solid State Communications **94**(9), p.719-723 (1995).

[233] S. Saintenoy, P. Wetzel, C. Pirri, D. Bolmont, and G. Gewinner, *Interaction of H with epitaxial Er silicide layers on Si(111) adsorption versus absorption*, Surface Science **349**, p.145-154 (1996).

[234] P. Wetzel, C. Pirri, and G. Gewinner, *Buckling reversal of the Si(111) bilayer termination of 2-dimensional $ErSi_2$ upon H dosing*, Europhysics Letters **38**(5), p.359-364 (1997).

[235] P. Wetzel, T. Angot, C. Pirri, and G. Gewinner, *Origin of the semimetal-to-semiconductor transition observed in two-dimensional Er silicide upon H exposure: evidence ot two chemisorption sites*, Surf. Sci. **383**, p.340-349 (1997).

[236] P. Louis, T. Angot, D. Bolmont, and G. Gewinner, *Pairing mechanism in interaction of atomic hydrogen with epitaxial erbium silicide*, Surf. Sci. **422**, p.65-76 (1999).

[237] M.-H. Tuilier, C. Pirri, D. Berling, D. Bolmont, G. Gewinner, and P. Wetzel, *Structure of clean and H-saturated epitaxial two-dimensional Er silicide on Si(111) studied by SEXAFS*, Surf. Sci. **555**(1-3), p.94-100 (2004).

[238] *http://www.icknowledge.com/glossary/s.html.*

[239] *http://www.ece.gatech.edu/research/labs/vc/theory/sheetRes.html.*

[240] L. Maissel and R. Glang, *Handbook of Thin Film Technology*. 1983: McGraw-Hill.

[241] J. Hornstra and L.J.v.d. Pauw, J. Electron. Control **7**, p.169 (1959).

[242] W.L.V. Price, *Extension of van der Pauw's theorem for measuring specific resistivity in disks of arbitrary shape to anisotropic media*, J. Phys. D: Appl. Phys. **5**(6), p.1127 (1972).

[243] W.L.V. Price, *Electric potential and current distribution in a rectangular sample of anisotropic material with application to the measurement of the principal resistivities by an extension of van der Pauw's method*, Solid State Electronics **16**, p.753-762 (1973).